

# Investigations of graphene-MOF composites and porous pillared graphene frameworks

A thesis submitted in partial fulfilment  
for the degree of

**Master of Science**

as part of the

**Integrated Ph. D. programme  
(Materials Science)**

by

**Ram Kumar**



Chemistry and Physics of Materials Unit  
Jawaharlal Nehru Centre for Advanced Scientific Research  
(*A Deemed University*)  
Bangalore, India.

**April 2013**



*Dedicated to my teachers, friends and family*



## DECLARATION

I hereby declare that the matter embodied in this M.S. thesis entitled “*Investigations of graphene-MOF composites and porous pillared graphene frameworks*” is the result of investigations carried out by me under the supervision of Prof. C. N. R. Rao, FRS at the Chemistry and Physics of Materials Unit, Jawaharlal Nehru Centre for Advanced Scientific Research, Bangalore, India and that it has not been submitted elsewhere for the award of any degree or diploma.

In keeping with the general practice in reporting scientific observations, due acknowledgement has been made whenever the work described is based on the findings of other investigators.

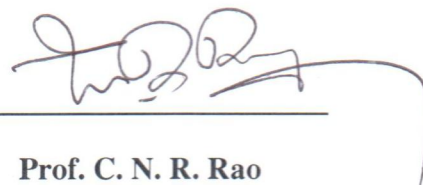
---

**Ram Kumar**



## CERTIFICATE

I hereby certify that the matter embodied in this M.S. thesis entitled “*Investigations of graphene-MOF composites and porous pillared graphene frameworks*” has been carried out by Mr. Ram Kumar at the Chemistry and Physics of Materials Unit, Jawaharlal Nehru Centre for Advanced Scientific Research, Bangalore, India under my supervision and it has not been submitted elsewhere for the award of any degree or diploma.



---

**Prof. C. N. R. Rao**  
**(Research Supervisor)**





## **Acknowledgements**

*I am extremely thankful to Prof. C. N. R. Rao, FRS and I take this opportunity to express my immense gratitude to him. He not only introduced me to the field of Material Science but also has helped me with his invaluable guidance and fascinating constant encouragement. He is a person of immense enthusiasm and wisdom. It is a rich and fulfilling experience to work under his guidance. He has taught me the various facts of science, the way of understanding the problem and how to maintain levelheaded approach when problems do not work.*

*I would like to express my sincere thanks to Dr. T.K. Maji for his constant guidance and fruitful discussions.*

*I thank Dr. A. Thirumurugan for collaborative work and various important discussions.*

*I would like to express my sincere thanks to Dr. A. Govindaraj who has helped me a great deal in carrying out various experiments. His friendly attitude towards me has made him a very approachable person for any kind of problem.*

*I would like to thank, specially Ms. Urmimala Maitra, Mr. K. Jayaramulu and Mr. M.V. Suresh for working with me in different research problems.*

*I would like to thank Dr. B.S. Naidu and Urmimala Maitra for helping me in PL measurement and various useful suggestions. I would like to thank Mr. Ritesh Haldhar and Mr. Arpan Hazra for help in gas adsorption measurements and analysis.*

*I would like to thank specially Dr. Krishnendu Biswas and Mr. Nitesh Kumar for suggestions and helping me in various possible ways during experiments.*

*I would like to thank all my present and past lab mates, Rana Saha, Dr. K. Vasu, Mosses, Sunita, Pramoda, Monali, Uttam, Dr. Prasad, Dr. Chhitiah, Sreedhara, Dr. H.S.S.R.*

*Matte, Bolla, Lngahmpallii, Sreekanth, Madhu, Ajmala, Dr. Barun Das, Dr. Anupama Ghosh, Dr. L.S. Panchkarla, Dr. Neenu, Dr. K.S. Subhramaniam, and Gopal, for helping in various occasions.*

*Also my heartfelt thanks to my all Int. Ph.D. batch mates of 2010, Sisir, Rajsekhar, Ankush, Anirban, Chandan De, Chandan Kumar and Arkomita and all the seniors for helping me in all ways possible.*

*I would like to thank the past and present Int. Ph.D. conveners, Prof. S. Balasubramanian and Dr. T. K. Maji.*

*I am thankful to the present and past chairman of our department, Prof. S. Balasubramanian and Prof. G. U. Kulkarni for providing and maintaining various facilities to all the students.*

*I am grateful to the administration of JNCASR.*

*I would like to express my gratitude to the various faculty members of the Chemistry and Physics of Materials Unit for the courses they offered and the wonderful classes.*

*My sincere thanks to the technical staffs of JNCASR for their help with the various characterization techniques.*

*I express my deep gratitude to Prof. S.K. Dash, Regional Institute of Education (NCERT), Bhubaneswar, Orissa for his guidance and encouragements towards research.*

*I would like to express my sincere thanks to my friends Pankaj Kumar Sharma, Rahul Pandey, Byasadev Pradhan and Rakesh (NCERT) for their help on various occasions.*

*My deepest thanks to Mrs. Indumati Rao and Mr. Sanjay Rao for their love, affection and hospitality extended to all of us during the course of my association with them.*

*I thank all my friends from, specially Sudip, Saumik, Anindita, Rajdeep, Devendra, Vasu, Dhanya, Vijay, Ramana, Anand, Arjun, Dr. Paramesh, Wasim and Pallavi.*

*Above all, I would like to thank my family for all the love, affection and support they gave. They stood by me whenever I felt depressed and led me to find out the correct way.*



## PREFACE

This thesis presents the results of investigations of graphene-metal organic framework (MOF) hybrid composites and porous pillared graphene frameworks. Graphene is a wonder material with novel electronic properties and also exhibits remarkably high surface area and gas adsorption capacity. MOFs have received widespread attention due to high surface area, optical property and catalytic applications. Composites of graphene with MOFs due to synergistic effects show many interesting optical and gas adsorption property.

Chapter 1 gives a brief overview of graphene and metal organic frameworks.

In chapter 2, the effect of graphene content on the optical property of lanthanide based MOFs has been studied. Graphene quenches the lanthanide emission.

In chapter 3 graphene oxide ZIF-8 hybrid nanocomposites are discussed. The morphology, surface area and CO<sub>2</sub> uptake were affected by graphene in the nanocomposite. Increase in CO<sub>2</sub> uptake is observed for hybrid nanocomposites due to synergistic effect of nano MOF and graphene. ZIF-8 nanoparticles on the graphene oxide basal plane are used as sacrificial agents for the synthesis of GO-ZnS composites.

Chapter 4 presents the effect of graphene in modulating the adsorption property of a flexible Cd-based MOF.

In chapter 5 a Pd (0) catalyzed coupling reaction has been employed for the synthesis porous 3D pillared graphene porous solid. These materials exhibit high thermal stability and high CO<sub>2</sub> uptake.



# Contents

|                               |      |
|-------------------------------|------|
| <i>Declaration</i> .....      | III  |
| <i>Certificate</i> .....      | V    |
| <i>Acknowledgements</i> ..... | VII  |
| <i>Preface</i> .....          | XI   |
| <i>Contents</i> .....         | XIII |

## Chapter 1.

|   |    |
|---|----|
| <i>Brief Overview of graphene and MOFs</i> .....        | 1  |
| 1.1.1 Introduction.....                                 | 1  |
| 1.1.2 Structural and electronic properties.....         | 2  |
| 1.1.3 Synthesis of single- and few- layer graphene..... | 3  |
| <i>Mechanical exfoliation and sonication</i> .....      | 3  |
| <i>Arc Discharge</i> .....                              | 4  |
| <i>Reduction of graphite oxide</i> .....                | 5  |
| <i>Chemical vapour deposition</i> .....                 | 6  |
| 1.1.4 Characterization.....                             | 7  |
| 1.1.5 Properties and applications.....                  | 10 |
| <i>Mechanical properties</i> .....                      | 10 |
| <i>Clean energy application</i> .....                   | 11 |
| <i>Chemical storage of hydrogen</i> .....               | 11 |
| <i>Gas adsorption</i> .....                             | 12 |
| <i>Supercapacitor</i> .....                             | 13 |
| <i>Fluorescence quenching</i> .....                     | 14 |
| 1.1.6 Chemistry of graphene.....                        | 15 |
| 1.2.1 Porous solids.....                                | 17 |
| 1.2.2 Metal-Organic frameworks (MOFs).....              | 18 |

|  |    |
|--|----|
| 1.2.3 Classification of MOFs.....          | 21 |
| 1.2.4 Zeolitic imidazolate frameworks..... | 24 |
| 1.2.5 Luminescent MOFs.....                | 25 |
| 1.2.6 Gas storage/Separation.....          | 28 |
| 1.2.7 Catalysis.....                       | 29 |
| 1.2.8 Graphene MOF hybrid composites.....  | 30 |

**Chapter 2.**

|  |           |
|--|-----------|
| <b>Quenching of lanthanide emission in composites of graphene with a Bi-based MOF.....</b> | <b>34</b> |
| Summary.....   | 34        |
| 2.1 Introduction.....  | 35        |
| 2.2 Materials and experiments.....   | 36        |
| 2.3 Results and Discussion.....  | 41        |
| 2.4 Conclusions.....   | 55        |
| References.....  | 55        |

**Chapter 3.**

|  |           |
|--|-----------|
| <b>Hybrid nanocomposites of ZIF-8 with graphene oxide exhibiting tunable morphology, significant CO<sub>2</sub> uptake and other novel properties.....</b> | <b>57</b> |
| Summary.....   | 57        |
| 3.1 Introduction.....  | 58        |
| 3.2 Materials and experiments.....   | 60        |
| 3.3 Results and discussion.....  | 62        |
| 3.3 Conclusions.....   | 73        |
| References.....  | 74        |



**Chapter 4.**

***Flexible Porous crystal composites of a Cd-based MOF and graphene.....76***

*Summary.....76*

*3.1 Introduction.....77*

*3.2 Materials and experiments.....78*

*3.3 Results and discussion.....80*

*3.3 Conclusions.....91*

*References.....92*

**Chapter 5.**

***Robust porous graphene frameworks pillared by organic linkers, with tunable surface area and gas storage.....94***

*Summary.....94*

*3.1 Introduction.....95*

*3.2 Materials and experiments.....97*

*3.3 Results and discussion.....101*

*3.3 Conclusions.....116*

*References.....117*

## *Brief overview of graphene and MOFs*

---

### **1.1.1 Introduction:**

Carbon is one of the most important elements in the periodic table and the source of life.<sup>[1]</sup> Besides its important role in organic chemistry, it forms many allotropes, two being known from ancient times (diamond and graphite) and some discovered recently (fullerenes and nanotubes).<sup>[2-4]</sup> The new two-dimensional form of carbon, graphene, consisting of atomically thin  $sp^2$  bonded carbon atoms has attracted widespread attention from the scientific community.<sup>[5-7]</sup> Graphene with interesting electronic, optical, high mechanical strength and chemical properties have wide range of applications.<sup>[7-9]</sup> It is used in energy storage devices, sensors, gas storage, electronics, optical, optoelectronic devices and polymer composites.<sup>[7, 8, 10, 11]</sup> Graphene normally refer to a single-layer of  $sp^2$  bonded carbon atoms, the properties of bi- and few- layer graphene synthesized using different chemical and physical methods have been investigated in detail.<sup>[12, 13]</sup> Graphene initially was obtained by micromechanical cleavage of graphite.<sup>[5]</sup> This method allows to get high quality graphene, but is not suitable for large scale synthesis. There has been significant progress in large scale synthesis of graphene using by chemical and physical routes.

## 1.1.2 Structural and electronic properties:

Graphene is the mother of all graphitic carbons including carbon nanotubes, and fullerenes.<sup>[6]</sup> Fig. 1.1.1 shows how 2-D graphene sheet can be wrapped, rolled or stacked to generate fullerene, nanotube and graphite.<sup>[6]</sup>

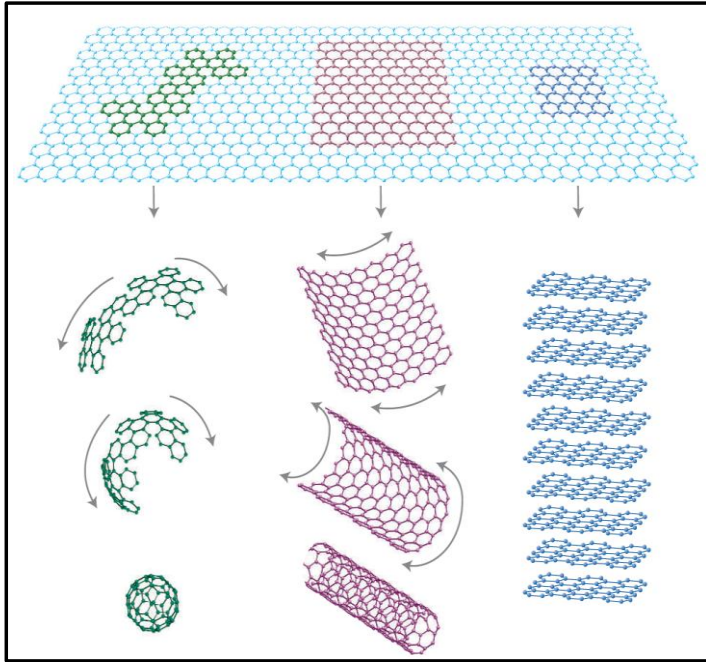


**Figure 1.1** Graphene: mother of all graphitic forms. It can be wrapped up into 0D buckyballs, rolled into 1D nanotubes or stacked into 3D graphite. [Adapted with permission from Ref. 6]

According to Mermin-Wagner theorem, there should be no long range order in two dimensions.<sup>[14, 15]</sup> Thus, dislocations will appear in two-dimensional crystals at any finite temperature, as a result two-dimensional crystals should be rippled. Indeed, ripples are observed in 2-D graphene sheets and play an important role in its electronic properties.<sup>[15]</sup> The electronic structure of graphene rapidly evolves with the number of layers and approaches the three dimensional electronic structure of graphite for more than 10 layers.<sup>[16-18]</sup> Monolayer and bilayer graphene have simple electronic structure and both are zero-gap semiconductors or zero-overlap

semimetals with electrons and holes as charge carriers. With increasing number of layers the electronic structure become complicated as several charge carriers appears, and the valence and conduction band start overlapping. Thus, electronic structure allows single-, double-, and few-(3 to <10) layer graphene to be distinguished as three different types of two-dimensional crystals.

### **1.1.3 Synthesis of single- and few- layer graphenes**

Several physical and chemical methods have been developed in recent years for the synthesis of graphene. Some of the important methods for synthesis are exfoliation, arc discharge, reduction of graphene oxide and sonication.

#### **Mechanical Exfoliation and sonication:**

Stacking of individual graphene sheets in graphite is due to weak van der Waals interaction between individual graphene sheets. Partially filled  $p_z$  orbital forms extended  $\pi$  bonding in graphene sheets. The delocalized  $\pi$  electron cloud of individual graphene sheets interacts with each other by  $\pi$ - $\pi$  interaction in graphite. Due to the weak bonding in perpendicular direction in comparison to very strong in-plane covalent bond, it has been attempted to synthesize graphene sheets through exfoliation of graphite. Graphene sheets with different number of layers have been obtained by micromechanical cleavage of HOPG using scotch tape.<sup>[5]</sup>

Using the concept involved in the dispersion and exfoliation of carbon nanotube in different organic solvents, solution phase exfoliation of graphite in different organic solvents have been performed to yield graphene sheets. Enthalpy of mixing of nanotubes per volume of solvent is given by

$$\Delta H_{mix}/V \approx 4(\sqrt{E_{s,NT}} - \sqrt{E_{s,sol}})^2 \varphi/D \quad (1)$$

In equation 1  $\varphi$  denotes the dispersed nanotube volume fraction,  $D$  is the dispersed nanotube (or bundle) diameter, and  $E_{s,NT}$  and  $E_{s,sol}$  are the surface energies of nanotube and solvent, respectively. The equation suggests that those solvents with surface energy close to that of the nanotube are very efficient in exfoliation and dispersion of SWNT.<sup>[19]</sup> Using this principle solution phase exfoliation of graphite in N-methylpyrrolidone yields single layer graphene. The energy required to exfoliate graphite is balanced by the solvent graphene interaction.<sup>[19]</sup>

### **Arc Discharge:**

Large scale synthesis of few layer graphene using simple procedure of arc discharge was reported by Rao *et al.*<sup>[12]</sup> This procedure of arc discharge yields 100 nm-300 nm graphene sheets (HG) with 2-3 layers. The use of small concentration of H<sub>2</sub> during arc discharge process terminates the dangling carbon bonds present on edges and prevents the formation of closed structure. The experimental conditions favorable for obtaining graphene in the inner wall of arc chamber are high DC current (above 100 A), high voltage (above 50 V) and H<sub>2</sub> (200 torr)/He (500 torr) gas mixture. The procedure has been further utilized for the synthesis of boron and nitrogen doped graphene in the presence of boron and nitrogen precursors.

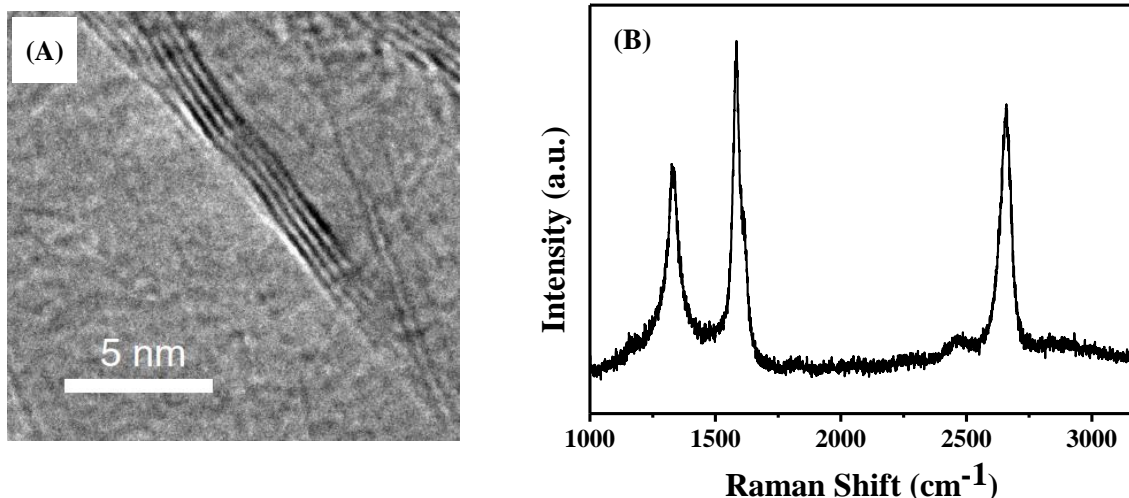


**Figure 1.2:** (A) TEM image of few layer graphene synthesized using arc discharge method (HG). (B) Raman spectrum of graphene synthesized using arc discharge method. [Fig.(A), Adapted with permission from Ref.12]

## Reduction of graphite oxide:

Graphite oxide synthesized by B.C. Bordie in the year of 1859, is an important precursor for large scale synthesis of graphene and various chemically modified forms of graphene.<sup>[20]</sup> Graphite oxide basal plane contains large concentration of epoxy, hydroxyl and carboxylic acid functional groups.<sup>[21]</sup> Oxygen containing functional groups makes graphite oxide highly hydrophilic and can be easily dispersed in water. Single layer graphene oxide dispersed in water can be easily reduced using various reducing agents such as  $N_2H_4$  and  $NaBH_4$ .<sup>[22, 23]</sup> Several other reducing agents such as hydroxylamine, phenyl hydrazine, glucose, ascorbic acid, hydroquinone etc. have been used.<sup>[24-28]</sup> Reduction method utilizing  $N_2H_4$  and  $NaBH_4$  are most widely used. Graphene synthesized using reduction of graphene oxide contains small concentration of unreduced oxygen containing functional groups or inserted N atom in aromatic rings in case of

hydrazine hydrate reduced samples. Acid treatment and thermal annealing have been further developed to increase the C/O ratio.<sup>[23, 29]</sup>

### **Chemical Vapor Deposition:**

CVD is the most promising inexpensive and readily accessible approach for the deposition of reasonably high quality graphene on transition metal substrates such as Ni, Pd, Ru, Ir, and Cu.<sup>[7, 30-35]</sup> The process is based on the saturation of carbon concentration on transition metal upon exposure to hydrocarbon gas at higher temperature. During cooling the solubility of carbon in the transition metal decreases and a thin film of carbon precipitates from the surface. Different hydrocarbons such as methane, ethylene, acetylene and benzene have been used for CVD growth of graphene. Radio frequency plasma enhanced chemical vapour deposition (PECVD) was used to synthesize graphene on variety of substrates such as Si, W, Mo, Zr, Ti, Hf, Nb, Ta, Cr, SiO<sub>2</sub>, Al<sub>2</sub>O<sub>3</sub> etc.<sup>[36-38]</sup> The PECVD have advantage of reduced energy consumption and prevents the formation of amorphous carbon or other types of unwanted products. Optimization of gas flow, hydrocarbon concentration and reaction temperature are important parameters for the growth of high quality graphene sheets. Fig.1.1.3 shows the TEM image and Raman spectrum of graphene prepared on Ni substrate by thermal decomposition of methane.

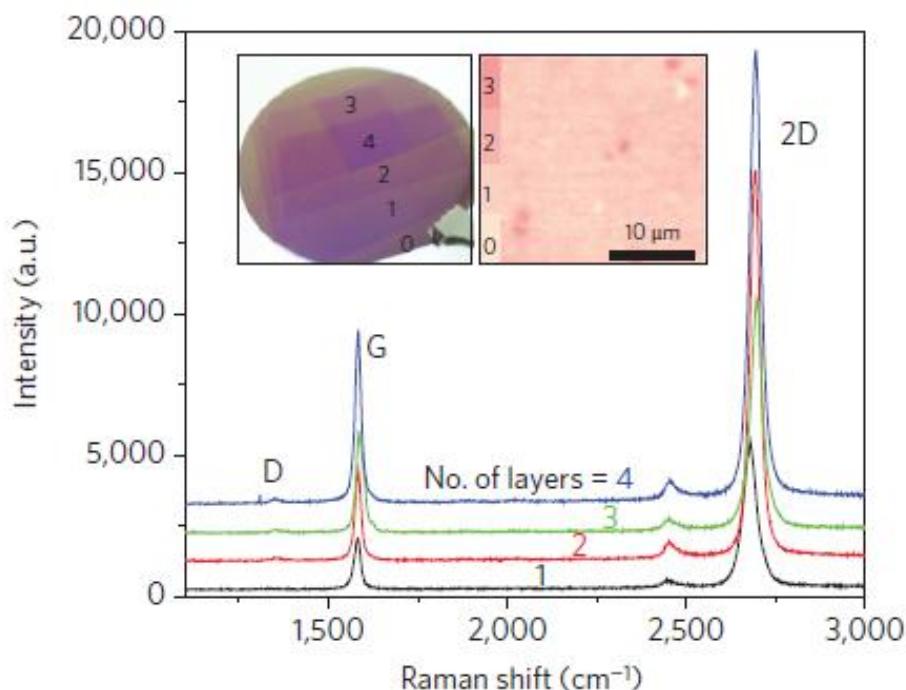


**Figure 1.3:** Raman spectra of graphene films with different number of layers. Inset shows transferred graphene layers on SiO<sub>2</sub>/Si substrate. [Adapted with permission from Ref. 35]

### **1.1.4 Characterization:**

Graphene has been characterized using different microscopy and spectroscopic technique. Transmission electron microscopy (TEM) and scanning electron microscopy (SEM) are used to obtain morphology. Atomic force microscopy (AFM) is used to obtain number of layers. Optical contrast of graphene is the most simple and reliable method for identifying different number of layers on different substrates. The contrast is due to interference of the reflected light beam at the air-to-graphene, graphene-to-dielectric (in the case of thin dielectric films) and dielectric-to-substrate interfaces. Fig.1.1.4A shows the single-, bi-, and multiple-layer (< 10 layers) graphene on Si substrate with a 285 nm SiO<sub>2</sub> film, differentiated by using contrast spectra, generated from the reflected light of a white light source.<sup>[39]</sup> One of the interesting properties of graphene is



fluorescence quenching of luminescent dye molecules and have been utilized to observe graphene on different substrates (Figure 1.1.4B) by using fluorescence quenching microscopy.<sup>[40]</sup> TEM images of single and bilayer graphene are shown in Fig. 1.1.4C, by keen observation of edges number of layers in few layer graphene can be obtained using TEM.<sup>[41]</sup> Atomic force microscope gives information about number of layers of graphene. Height profile analysis of AFM images gives the clear idea about the number of layers present in graphene. Fig. 1.1.4D shows the AFM images of exfoliated graphene oxide sheets with high profile showing mostly single layer.<sup>[22]</sup>

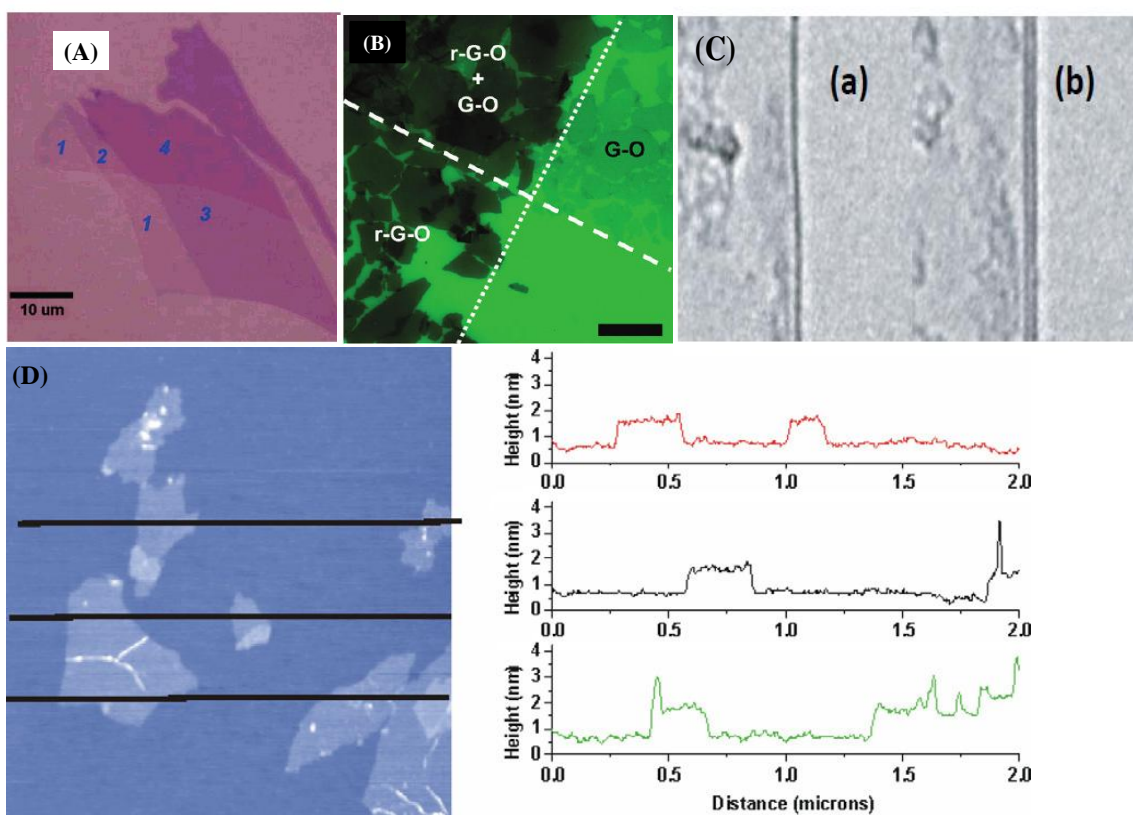


**Figure 1.4:** (A) Optical image of graphene with one, two, three and four layers.[ Adapted with permission from Ref. 39]. (B) Visualization of GO and RGO by fluorescence quenching microscopy.[ Adapted with permission from Ref. 40]. (C) TEM images of graphene. [Adapted with permission from Ref. 41] (d) AFM image of graphene oxide sheets along with height profile in different locations. [Adapted with permission from Ref. 22]

Raman spectroscopy is a relatively easy non-destructive and quick measurement to probe the inelastic scattering of light from sample surface. It is very helpful in characterizing nanocarbons.<sup>[42]</sup> Raman spectrum of graphene shows three characteristic bands, D band around  $1300\text{ cm}^{-1}$ , G band around  $1580\text{ cm}^{-1}$ , and the 2 D band around  $2700\text{ cm}^{-1}$ . In addition to these three bands sometimes D' band near  $1620\text{ cm}^{-1}$  is observed. The D and D' bands are defect induced Raman features. The G-band is due to in-plane vibrations of the  $\text{sp}^2$  carbon atoms. The integrated intensity ratio  $I_D/I_G$  for D band and G band is widely used for characterizing the defect quantity. The 2 D band related to the double resonance Raman scattering process is symmetry allowed.<sup>[43]</sup>

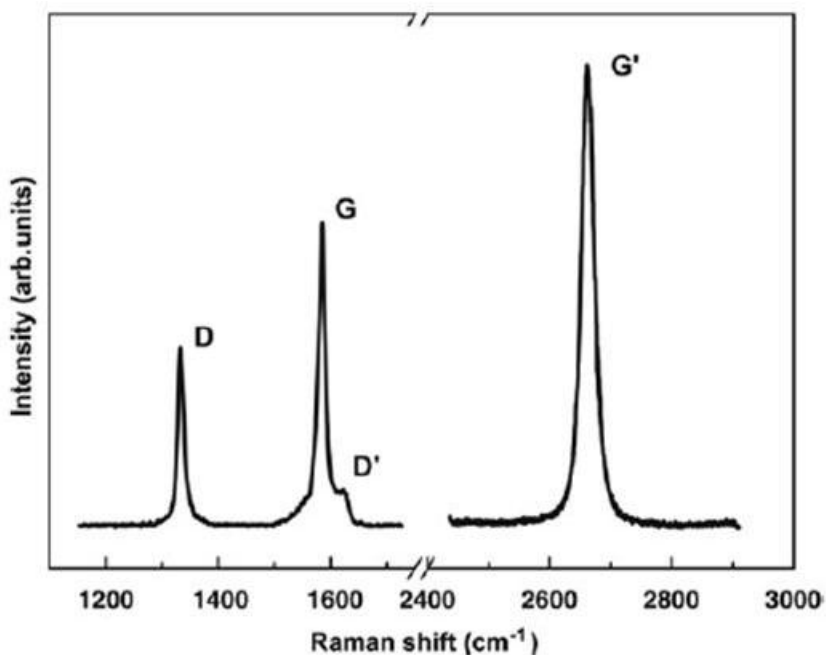


**Figure 1.5:** Raman spectrum of graphene showing characteristic D band, G band, D' band and 2 D band. [Adapted with permission from Ref. 43]

### **1.1.5 Properties and applications:**

As explained in earlier sections 2-D sheets of graphene exhibits many interesting properties which make it applicable in large range of applications. Some of the remarkable property of graphene and its corresponding applications are briefly explained in this section.

#### **Mechanical properties:**

Graphene shows very high mechanical strength. Lee *et al.* measured the elastic property and intrinsic breaking strength of free standing monolayer graphene membranes by nanoindentation.<sup>[9]</sup> Graphene showed an elastic modulus of  $\sim 1$  TPa, a strength of  $\sim 130$  GPa and a breaking strength of  $42\text{Nm}^{-1}$ . Very high mechanical strength of graphene has been utilized in designing high performance graphene reinforced polymer matrix composites. A significant increase of 35% and 45% respectively in the elastic modulus and hardness was obtained on the addition of just 0.6 wt.% of graphene to PVA matrix.<sup>[44]</sup> Detailed investigation of synergistic effect and mechanical properties of binary combinations of nanodiamond (ND), few-layer graphene (FG) and single-walled carbon nanotubes (SWNT) in PVA matrices have been carried out. The mechanical properties of resulting composites, evaluated by nanoindentation technique showed remarkable synergy with improvement by as much as 400% in stiffness and hardness compared to those obtained with single nanocarbon reinforcements. Extraordinary synergy was observed in ND + FG composites (PVA-0.4FG-0.2ND) with 4 and 1.5-fold increase in elastic modulus and hardness respectively. Variation in the percent crystallinity (%) of the PMCs with

the two nanocarbon is 2%, which shows that increase in crystallinity is not the cause of observed synergy.<sup>[45]</sup>

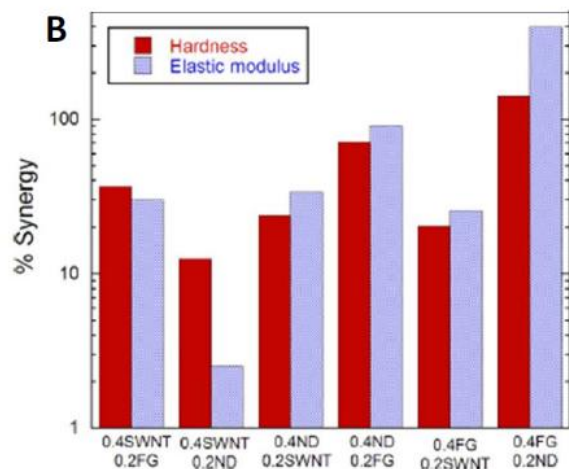


**Figure 1.6:** Percentage synergy in hardness and elastic modulus for different binary nanocarbon composites. [Ref. 45]

## Clean energy applications:

### (A) Chemical storage of Hydrogen

The amount of chemical energy which can be stored per mass of hydrogen ( $142 \text{ MJkg}^{-1}$ ) is at least three times larger than that of other chemical fuels (equivalent value for liquid hydrocarbons are around  $47 \text{ MJkg}^{-1}$ ).<sup>[46]</sup> Only combustion product of hydrogen is water has lot of advantage over hydrocarbons which produces greenhouse  $\text{CO}_2$  as combustion product. One of the major obstacles for the mobile applications of hydrogen is efficient storage. Lot of research in MOFs and other hydrogen storage materials have been performed but storage capacity is low at room temperature. In this regard chemical storage of graphene in few layer graphene is very promising. By using Birch reduction up to 5 wt.% of hydrogen can be stored under ambient condition without the need of high pressure. The stored hydrogen can be released within few minutes on laser irradiation.<sup>[47]</sup>

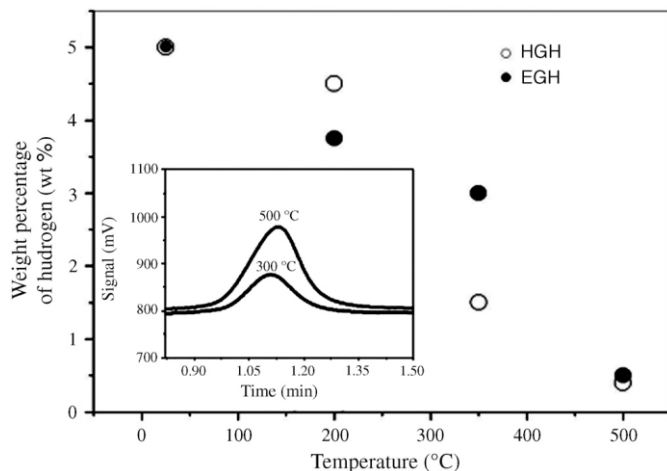


**Figure 1.7:** Change in weight percentage of hydrogen in two different few layer graphene samples (EGH, HGH). Inset shows the evolution of hydrogen recorded by gas chromatograph. [Ref. 47]

## (B) Gas adsorption

Theoretically predicted surface area of single layer graphene is  $2600 \text{ m}^2/\text{g}$ .<sup>[48]</sup> This theoretically predicted high surface area of graphene is hardly achieved due to strong  $\pi$ - $\pi$  interaction between graphene sheets. Due to this strong  $\pi$ - $\pi$  interaction graphene sheets are agglomerated and show much less surface area than theoretically predicted value. Few layer graphene samples prepared by different method have surface area in the range of  $270$ - $1550 \text{ m}^2/\text{g}$ . The  $\text{H}_2$  adsorption measurement on few layer graphene samples prepared by exfoliation of graphite oxide (EG) and conversion of nanodiamond exhibited uptake up to  $1.7 \text{ wt.}\%$  at  $77\text{K}$ . High pressure measurement showed an uptake of  $3 \text{ wt.}\%$   $\text{H}_2$  at  $100 \text{ atm}$  and  $298 \text{ K}$ . The prepared samples showed highest  $\text{CO}_2$  uptake of  $35 \text{ wt.}\%$  at  $1 \text{ atm}$  and  $195 \text{ K}$ . The  $\text{H}_2$  uptake was observed to increase with increasing surface area (Fig.1.1.8A).<sup>[49]</sup>

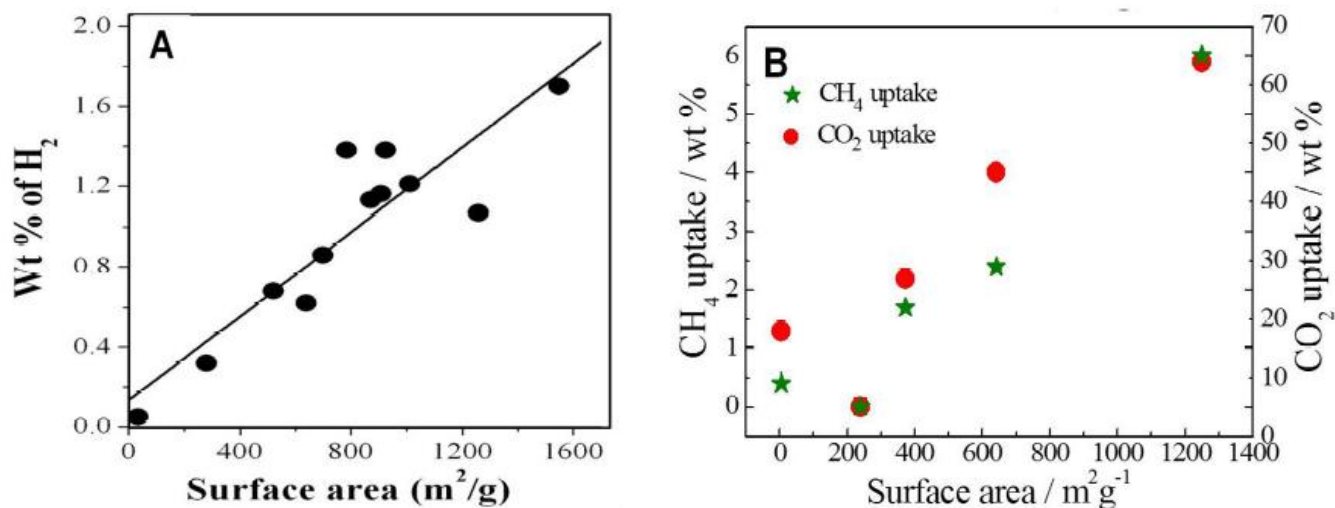


**Figure 1.8:** (A) Increase in H<sub>2</sub> uptake with increasing surface area at 1 atm and 77 K for various graphene samples. (B) Increase in CO<sub>2</sub> uptake (at 195K and 1 atm) and methane uptake (at 298 K and 5 MPa) with increasing surface area. [Adapted with permission from Ref. 49]

## Supercapacitors

Few layer graphene prepared by thermal exfoliation of graphene and conversion of nanodiamond has been studied as an electrode material for supercapacitors. The few layer graphene showed high specific capacitance up to 117 F/g in aqueous electrolyte and an operating voltage of 1 V. In ionic liquid [(N-butyl-N-methylpyrrolidinium bis (trifluoromethanesulfonyl)imide); (PYR14TFSI)] specific capacitance and energy density of 75 F/g and 31 Wh kg<sup>-1</sup> respectively was obtained at an operating voltage of 3 V. Figure 1.1.9 shows the Voltametric characteristic and specific capacitance as a function of scan rate.<sup>[7]</sup>

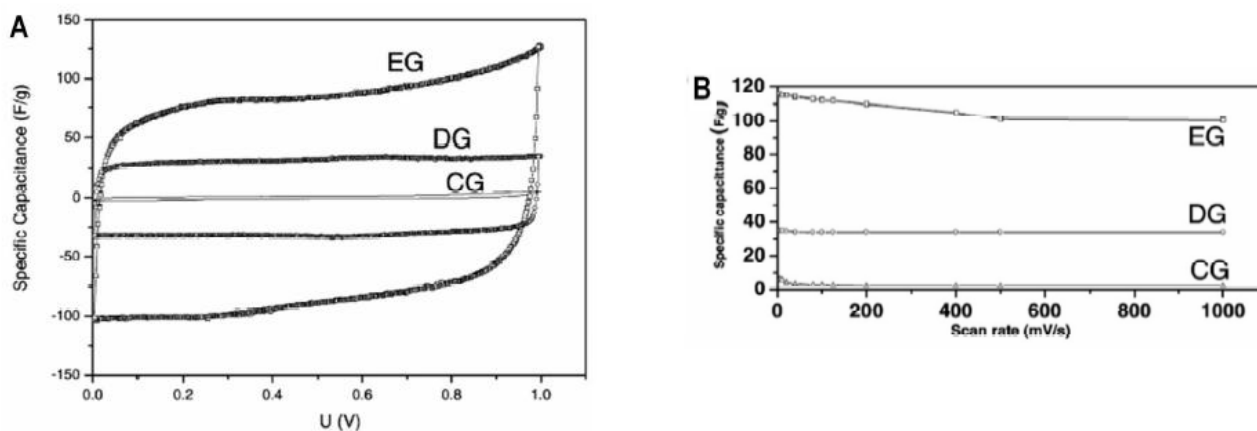


**Figure 1.9:** (A) Voltametric characteristics of a capacitor built from different graphene samples in aqueous electrolyte (1M H<sub>2</sub>SO<sub>4</sub>) (B) Specific capacitance as a function of scan rate for different graphene samples. [Adapted with permission from Ref. 7]

## Fluorescence Quenching:

Graphene is an efficient fluorescence quencher.<sup>[40, 50]</sup> Fluorescence quenching of aromatic dye molecules and semiconductor nanoparticle graphene composites have been studied. Fig.1.1.10 shows the PL emission spectrum of OPV ester with increasing concentration of graphene. Large quenching of fluorescence emission supported by decrease in lifetime was observed. Graphene acts as an electron acceptor and both charge transfer and energy transfer mechanism have been given to explain the observed fluorescence quenching. This property of fluorescence quenching has been utilized in characterizing graphene and as bio sensors. Electron transfer from semiconductor nanoparticle to graphene sheets has been used for photocatalytic applications of graphene.<sup>[50]</sup>

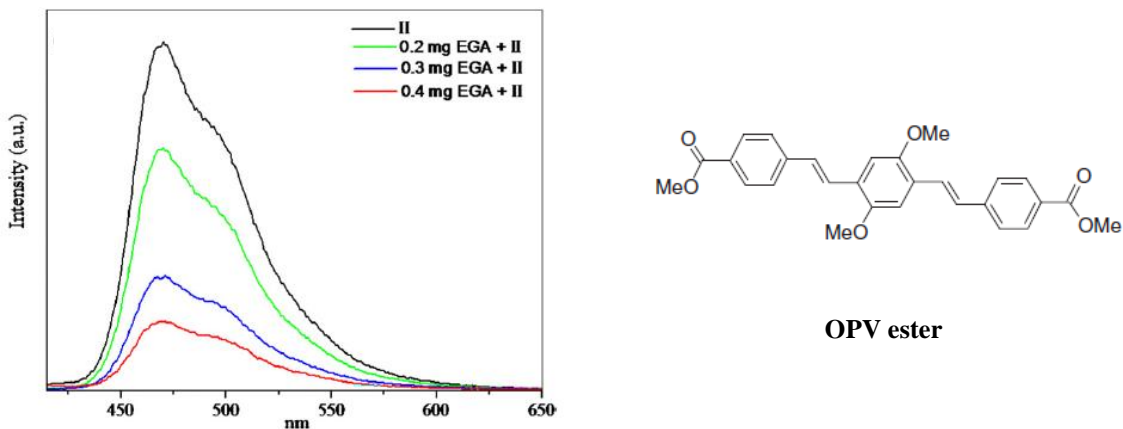


**Figure 1.10A:** Quenching of OPV ester fluorescence with increasing concentration of graphene. [Adapted with permission from Ref. 50]

### **1.1.6 Chemistry of graphene:**

Covalent and non-covalent chemistry of graphene has been explored recently to some extent.<sup>[51-53]</sup> Graphene with its  $\pi$  electron cloud gives the opportunity of interaction with various aromatic systems. This  $\pi$ - $\pi$  interaction of graphene has been utilized for dispersing graphene sheets in various solvents. Coronene tetracarboxylic acid salt was used for dispersing graphene sheets. In this regard non-covalent interactions have an advantage over covalent bond formation which perturbs the electronic structure of graphene. Carboxylic acid functionalization of graphene has been performed by treating with  $\text{HNO}_3$  and  $\text{H}_2\text{SO}_4$  mixture.<sup>[7]</sup> Obtained functionalized graphene sheets can be easily dispersed in various solvents. After treatment with  $\text{SOCl}_2$  various molecules can be attached to graphene basal plane by amide bond formation. Functionalization of graphene basal plane using different diazonium salts for various applications have been performed. Palladium catalysed C-C and C-N coupling reactions are well



explored in synthetic organic chemistry for the synthesis of various drugs and biomolecules. Such coupling reactions have not been developed for covalent modification of nanocarbons. Since Pd catalyzed coupling reactions are highly efficient and simple, in chapter 5 Sonogashira coupling reaction has been used for the synthesis of highly porous 3D graphene structures. Various modifications of graphene basal plane according to required applications are possible using these coupling reactions. Presently Pd(0) catalyzed Buchwald-Hartwig C-N coupling reaction and Suzuki coupling (C-C) reactions in graphene and carbon nanotube are under investigation.

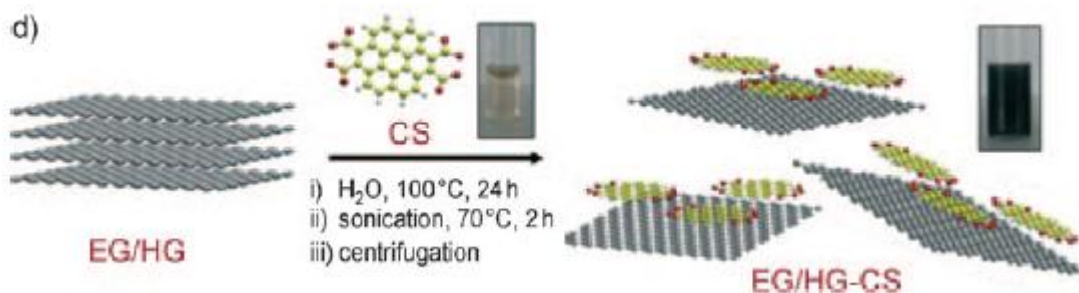


**Figure 1.10B:** Schematic representation of the exfoliation of few-layer graphene with CS to yield monolayer graphene-CS composites. [Adapted with permission from Ref. 53]

## **1.2.1 Porous Solids:**

Solids containing voids or empty space in their structure which can be used for trapping adsorbates are called porous solids. Porous solids can be highly crystalline zeolites and metal organic frameworks or amorphous activated carbon. Depending on the size of pore present these porous solids are classified as microporous ( $2\text{ nm} <$ ), mesoporous ( $2\text{ nm}-50\text{ nm}$ ) and macroporous ( $> 50\text{ nm}$ ).<sup>[54]</sup> Sometimes a distribution of pore size is observed. The voids in these porous solids are generally occupied by guest or template molecules and can be easily removed by heating or evacuation. Till 1990s zeolites and activated carbon were most explored porous solids. In 1990s mesoporous silica based porous solids (MCM-41 and SBA-15) were developed.<sup>[55, 56]</sup> Followed by the initial work of Robson *et al.* in 1990 there has been significant development in high surface area MOFs since 1995.<sup>[57, 58]</sup> Along with conventional porous materials nanocarbons such as carbon nanotubes and carbon fibers were also studied for gas storage applications.<sup>[59]</sup> Recently graphene based carbon materials have been studied for gas storage and catalyst support.<sup>[47, 49, 60]</sup> Some of the new materials with high surface area and remarkable  $\text{CO}_2$  and  $\text{CH}_4$  adsorption capability that have been developed recently are graphene like Borocarbonitrides,  $\text{B}_x\text{C}_y\text{N}_z$  by Rao *et al.*<sup>[61]</sup> Other important developments in last one decade are covalent organic frameworks (COFs) and conjugated microporous polymers. Owing to the well-known industrial requirement for porous solids in storage/separation, catalysis, ion exchange, sensors etc.<sup>[62]</sup> Lots of development in the area of porous solids is expected depending on required applications.  $\text{CO}_2$  sequestration is other area where porous solids can have significant advantage over amine based solvents.<sup>[63]</sup> Graphene based porous solids are highly promising for  $\text{CO}_2$  sequestration applications. In Chapter 5 a new route for the synthesis of pillared 3D porous structure of graphene with significantly high  $\text{CO}_2$  uptake is explored.

## 1.2.2 Metal-Organic Frameworks (MOFs):

Metal-organic frameworks (MOFs) or porous coordination polymers (PCPs) are an important class of hybrid materials that exist as infinite crystalline lattices consisting of inorganic vertices (Figure 1.2.2) and organic struts (Figure 1.2.3), connected by coordination bonds of moderate strength.<sup>[54]</sup> MOFs have attracted widespread attention because of the potential of exploiting both inorganic and organic components within the same framework structure.<sup>[64]</sup> Inorganic elements in framework structure provide the potential of similar properties to traditional zeolites, mechanical and thermal stability, regular structure along with many other interesting material properties such as optical and magnetic. Organic ligands offer tunable properties based on shape, size and functionality. By changing the length of ligand, binding site of ligands and introducing different functional group in linker lot of important property, flexibility and pore size can be tuned. Large numbers of organic ligands are commercially available or can be designed according to pore size and functionality requirements.

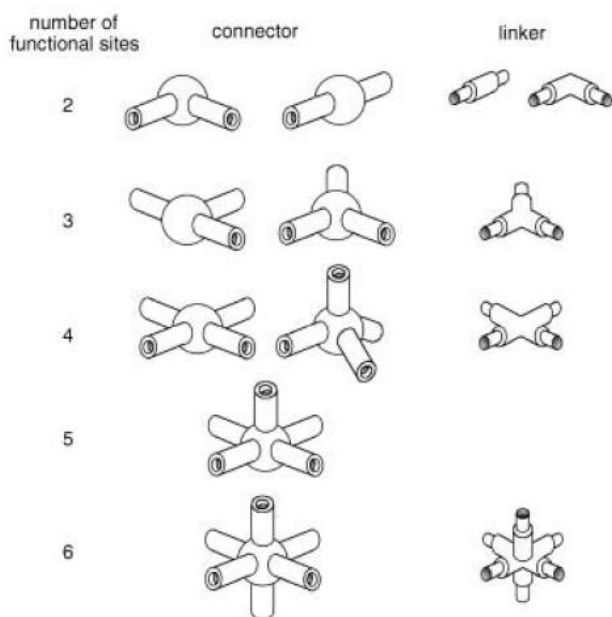
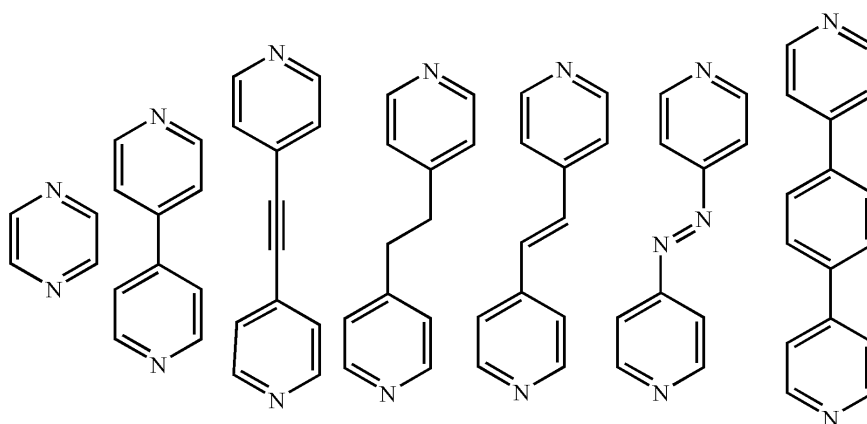


**Figure 1.11:** Components of metal organic frameworks (MOFs)/Coordination polymer. [Adapted with permission from Ref. 54]

## (a) Inorganic ligands:

Halides (F, Cl, Br, and I), Cyanometallate ( $[M(CN)_x]^{n-}$ ),  $CN^-$ ,  $SCN^-$

## (b) Neutral organic ligands



## (c) Anionic organic ligands

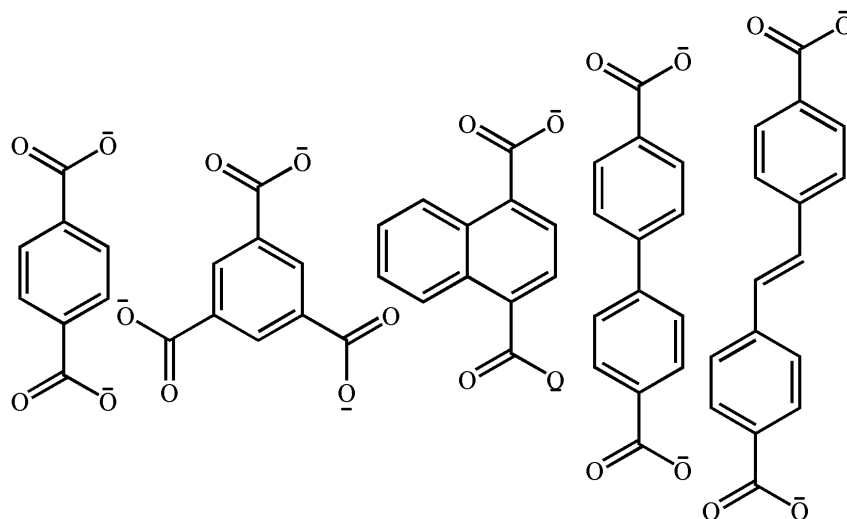


**Figure 1.12:** Commonly used Ligands for the synthesis of metal organic frameworks (MOFs)/Coordination polymers.

Maximum MOFs are microporous although few mesoporous frameworks have also been reported. The design of MOFs with ordered array of the basic building units has been extensively studied for the development of new solid state functional materials. Large number of dense as well as porous structure based on carboxylate functional group of ligand has been synthesized with many interesting property.<sup>[65]</sup> Generally framework structures based on metal carboxylates are rigid and have been used to design high surface area materials for gas storage applications.<sup>[66]</sup> Other interesting classes of MOFs are flexible which responds reversibly to external stimuli. In addition to coordinate bond other weak interactions such as hydrogen bonding,  $\pi$ - $\pi$  interactions and van der Waals interactions are generally utilized for designing flexible MOFs. Crystalline structures are generally rigid and flexibility of framework structures is an important property of MOFs.<sup>[67]</sup> The topology of MOFs are intimately related to the coordination environment of metal ion and the geometry of the organic ligand, which together form overall framework structure and dictate the property. Hybrid organic inorganic analogue of zeolites using imidazole ligands and Zn (II) metal ion with very good chemical and thermal stability are other important class of MOFs.<sup>[58]</sup>

Typically MOFs are synthesized under solvothermal condition by taking appropriate concentration of metal ion, organic ligand and suitable solvent. Reaction temperature, choice of solvent, reaction time and pH plays an important role in designing the framework structure. Other important parameters controlling the formation of framework structure are kinetic and thermodynamic control. Slow diffusion technique has also been used to grow MOF crystals under ambient condition. In this technique metal ion and ligand are dissolved in two different solvent and slow diffusion forms the MOF crystals at liquid- liquid interface. Recently, other

techniques such as sonochemical, microwave and mechanochemical synthesis etc. have been developed for the synthesis of MOFs.

Highly porous structure with very well defined and tailorable pores and specific functionality makes MOFs one of the promising materials for gas storage/separation, catalysis and sensing applications.<sup>[21]</sup> In addition to gas storage applications lanthanide/lanthanide doped frameworks and lanthanide and transition metal based heterometallic frameworks shows very interesting optical and magnetic properties.<sup>[66, 68]</sup> Using proper choice of metal ion and ligand multifunctional material with luminescence, magnetism and porosity can be designed. These materials will have promising optical, optoelectronic, sensing and biomedical applications. Recently many nano-MOF and hybrid composites have also been synthesized.<sup>[69]</sup> A brief account of some of the promising applications of these hybrid organic inorganic framework materials are given in separate section.

### **1.2.3 Classification of MOFs:**

Table 1 shows the complete range of possibilities in terms of M–ligand–M connectivity and extended inorganic dimensionalities. In table 1,  $m$  represents the dimensionality of ligand bridging ( $O^m$ ) and  $n$  represents the dimensionality of inorganic connectivity ( $I^n$ ). Overall the structure is represented by the notation  $I^nO^m$  and the sum of exponents gives the overall dimensionality of the structure. Interestingly the entire family of organometallic chemistry and much of classical coordination chemistry is represented within a single box ( $I^0O^0$ ) in table 1 (i.e. both the ligand connectivity M–L–M ( $m$ ) and inorganic connectivity ( $n$ ) = 0). The remaining three boxes in the first column represent the coordination polymers with extended ligand connectivity in different dimension and overall dimensionality 1–3. The three boxes in the

second column represent hybrid compounds with extended inorganic connectivity in one dimension ( $I^1$ ) with an overall dimensionality between 1 and 3. The two boxes in the third column represent hybrid compounds with extended inorganic connectivity in two dimensions with the overall dimensionality of structure between 2 and 3. The first box in the fourth column represents a rare class of hybrid compound ( $I^3O^0$ ) with the extended inorganic connectivity in all the three dimensions ( $I^3$ ) and overall dimensionality of 3. Hybrid compounds with zero inorganic connectivity and ligand connectivity M-L-M in different dimensions are coordination polymers, which can be represented as  ${}_xI^0O^m$  where  $x$  represents the nuclearity of the metal site. For coordination polymers with isolated metal sites,  $x = 1$  and for cluster metal sites,  $x > 1$ .<sup>[66]</sup>

Dimensionality of inorganic connectivity,  $I^n$  ( $n = 0-3$ )

|   | 0   | 1  | 2  | 3                              |
|---|---|--|--|--------------------------------|
| 0 | Molecular complexes<br>$I^0O^0$           | Hybrid inorg chains<br>$I^1O^0$                | Hybrid inorg. layers<br>$I^2O^0$               | 3-D Inorg. hybrids<br>$I^3O^0$ |
| 1 | Chain coordination polymers<br>$I^0O^1$   | Mixed inorg.-organic layers<br>$I^1O^1$        | Mixed inorg.-organic 3-D framework<br>$I^2O^1$ | —                              |
| 2 | Layered coordination polymers<br>$I^0O^2$ | Mixed inorg.-organic 3-D framework<br>$I^1O^2$ | —  | —                              |
| 3 | 3-D coordination polymers<br>$I^0O^3$     | —  | —  | —                              |

Table 1.1: Classification of hybrid inorganic-organic framework solids.

In addition to the given broader classification of hybrid materials of which coordination polymers or MOFs are one of the subset, MOFs have also been classified according to flexibility and dynamic behavior of structure. Kitagawa *et al* have classified MOFs/PCPs into three categories, viz. first, second and third generations (Figure 1.2.4) based on their structural response upon guest removal.<sup>[67]</sup> The first generation framework structure collapses irreversibly after the removal of guest molecules. The second generation MOFs/PCPs has stable and robust structure which maintains original framework structure upon guest removal. Large surface area highly porous MOFs such as ZIFs and MOF-5 can be classified in this category. The third generation MOFs/PCPs has flexible structure which responds reversibly to external stimuli, such as solvent or guest molecules. These classes of hybrid solids show selective adsorption property and interesting adsorption property. Chapter 3 of thesis deals with the application of graphene in modulating the adsorption property of flexible MOFs.

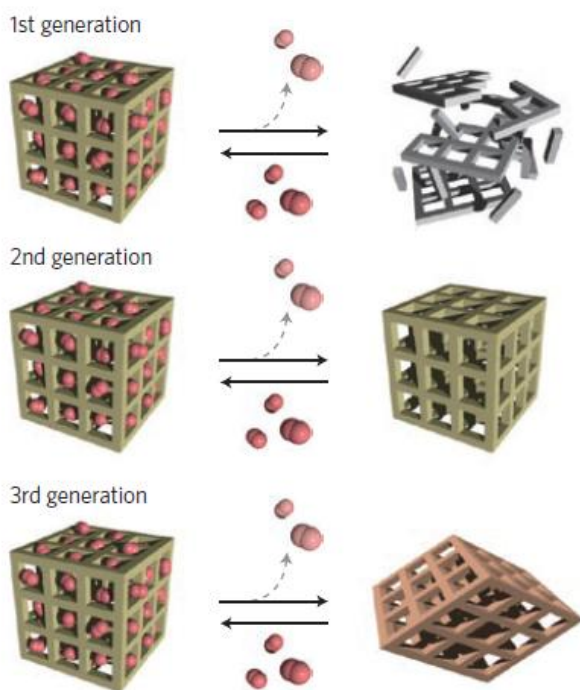
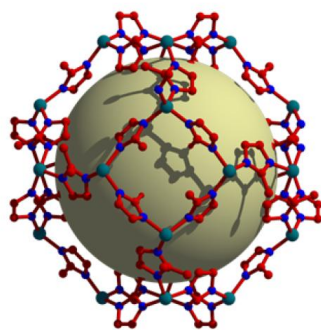


**Figure 1.13:** Classification of metal organic frameworks (MOFs). [Adapted with permission from Ref. 67]



### **1.2.4 Zeolitic imidazolate frameworks :**

Zeolitic imidazolate frameworks are an important class of MOFs with structure analogous to zeolites. These framework structures are designed by carefully selecting metal ion and imidazole based linkers. These imidazole based ligands make M-Im-M angle close to  $145^\circ$ , which is coincident with the Si-O-Si angle commonly found in many zeolite structures. ZIFs have been shown to have high thermal and chemical stability and surface area.<sup>[58]</sup> ZIFs have advantage in comparison to conventional zeolites, many ZIF structure have been reported to have remarkably high surface area in comparison to inorganic zeolites. In addition to higher surface area different functional group can be attached to imidazole linkers for specific applications. ZIF-8 is one of the widely studied zeolitic imidazolate framework with a sodalite zeolite structure, containing large cavities ( $\sim 11.7 \text{ \AA}$  of diameter) interconnected by narrow windows ( $\sim 3.40 \text{ \AA}$ ). ZIF-8 nanoparticles can be easily synthesized using simple mixing of 2-methylimidazole and Zn (II) ion solution in water or methanol. High surface area with good thermal and chemical stability has made it promising in catalysis, gas storage, polymer membranes for gas separation etc. Hybrid nanocomposites of ZIF-8 with metal, semiconductor and transition metal oxide nanoparticles with interesting optical and magnetic property have been studied.<sup>[70]</sup>



ZIF-8

Figure 1.14: Figure showing the pore of ZIF-8

## 1.2.5 Luminescent MOFs

Luminescence in MOFs arises from direct organic ligand excitation of highly conjugated ligands, charge transfer process such as metal to ligand charge transfer (MLCT) and ligand to metal charge transfer (LMCT) and metal centered emission in case of lanthanide ions due charge transfer process. The 4f orbital in lanthanide ions ( $\text{Ln}^{3+}$ ) are shielded by filled  $5s^2$  and  $5p^6$  orbitals.<sup>[71]</sup> Due to the shielding of 4f orbital lanthanide ions are less sensitive to the chemical environment around the metal ion and have well-defined energy levels. Owing to the well-defined energy levels each lanthanide ion exhibits narrow and characteristic 4f-4f transitions. Figure 1.2.5 shows the electronic energy levels of lanthanide ions. Due to the forbidden f-f transitions lanthanide ions suffer from weak light absorption, which makes the direct excitation of metal ions very inefficient. However in case of MOFs this is not a problem due to energy transfer from photo excited organic ligand to lanthanide centers. Figure 1.2.6 shows the process of energy transfer from ligand to lanthanide ions. The main energy transfer process involves ligand centered absorption followed by intersystem crossing  $S_1 \rightarrow T_1$ ,  $T_1 \rightarrow \text{Ln}^{3+}$  transfer, and metal- centered emission. Other possible energy transfer process involves direct energy transfer from excited singlet state  $S_1$  of ligand to the energy levels of lanthanide ion. This mechanism of direct energy transfer is known for  $\text{Eu}^{3+}$  and  $\text{Tb}^{3+}$ . If the process of energy transfer is not very efficient, both remaining ligand fluorescence and the lanthanide centered emission are observed. Efficient energy transfer is achieved by proper choice of ligands. The lowest triplet state of the organic linker should have to be located at an energy level nearly equal to or above the resonance level of the lanthanide ions.<sup>[72]</sup>



Due to very sharp and well defined emission spectrum of lanthanide based MOFs it has promising applications in optical, optoelectronic and biomedical applications and as sensors. Several heterometallic lanthanide frameworks have also been designed. Recently bismuth based frameworks which have not been studied in detail have been shown as a very efficient host for lanthanide ions with very efficient energy transfer and high quantum yield.<sup>[73]</sup> The possibility of having optical, magnetic and porosity property in same hybrid material is interesting. Chapter 1 of thesis deals with lanthanide doped bismuth based framework graphene composites and effect of graphene on fluorescence property.

In addition to lanthanide ion based luminescent MOFs several other luminescent MOFs due to flourishing highly conjugated ligands or fluorescent guest have been studied. The Charge transfer luminescence in  $d^{10}$  metal ions has been explored. Ligand based luminescence are generally stronger in MOFs in comparison to solution due to rigid arrangement of linkers around the metal ions. In addition to the enhancement in lifetime and quantum yield of ligand based luminescence in framework structure, shift in absorption maxima is generally observed due to enhanced molecular interactions. Loss of fine structure and broadening of emission spectrum is observed.<sup>[74]</sup>

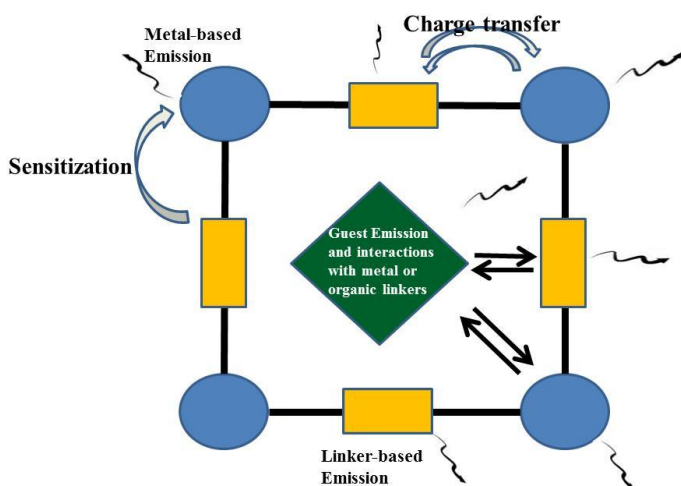


**Figure 1.17:** Various possibilities of luminescence in MOFs

### **1.2.6 Gas storage/ Separation:**

One of the most important properties of MOFs which have been studied in very detail for clean energy applications is very high surface area with well-defined pore structure.<sup>[75]</sup> Some of the remarkably high surface area MOFs reported in literature are MOF-177 ( $5640 \text{ m}^2\text{g}^{-1}$ ), MIL-101 ( $5900 \text{ m}^2\text{g}^{-1}$ ), UMCM-2 ( $6000 \text{ m}^2\text{g}^{-1}$ ) and MOF-210 ( $6240 \text{ m}^2\text{g}^{-1}$ ).<sup>[76-79]</sup> The exceptionally high surface area along with well-defined nanospace inside their framework structure allows them to efficiently trap various gas molecules. With the merits of high crystallinity, porosity and controllable structural characteristics, MOFs have been studied for  $\text{H}_2$ ,  $\text{CH}_4$  storage and  $\text{CO}_2$  sequestration. Although hydrogen storage in MOFs have been studied in great detail methane storage in MOFs have not been explored in much detail. Compared to petroleum oil, methane can provide much more energy because of its higher hydrogen-to-carbon ratio. Other application where MOFs will have promising application is  $\text{CO}_2$  sequestration. MOFs provide significant advantage over amine based solvents presently used for  $\text{CO}_2$  sequestration in thermal power plants. Amine based solvents suffer from solvent degradation, toxicity, corrosive nature, and high energy demand for the solvent regeneration.<sup>[63]</sup>

Adsorptive separation is an important industrial process. Industrial separation process uses porous solid materials such as zeolites, silica gel, and activated carbon as adsorbents. The basic principle for separation is different affinity between different adsorbates and the surface of adsorbents. The adsorption capacity and selectivity of an adsorbent are the requisite for adsorptive gas separation. The adsorption capacity depends on the equilibrium pressure and temperature, the nature of the adsorbate, and the nature of the micropores in the adsorbent. The selectivity is significantly more complicated, as it seems to be integrative and process related

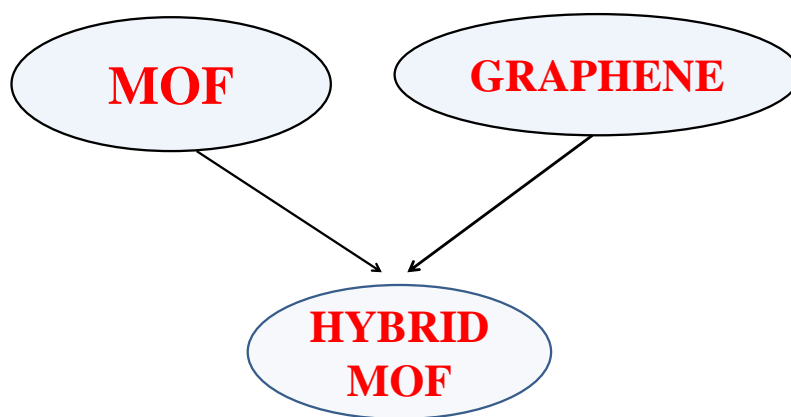
issue in practical separation, though it is still related to the operational temperature and pressure and the nature of adsorbate- adsorbent interaction.<sup>[54, 75]</sup> Many MOFs and MOF polymer membrane composites have been studied for gas separation applications. ZIF-8 polymer membranes have been studied for gas separation with interesting results.<sup>[80]</sup>

### **1.2.7 Catalysis:**

One of the interesting applications of MOFs is in catalysis. The metal or metal clusters, used as connecting nodes can be used to catalyze organic reactions. Shape and selectivity are important parameter in industrial catalytic process and nonporous MOFs with tunable pore size and functionality attached to ligands have been utilized.<sup>[66, 68]</sup> The catalyst must have uniform pores with molecular dimensions, in order to provide shape/sizes selective behavior. Uniform porosity in case of MOFs is an outcome of highly ordered structure. Due to the very open architecture, self-diffusion coefficients of molecules in the pore system are only slightly lower than in the bulk solvent. The mass transport in the pore system is not hindered. The ordered structure offers the opportunity to spatially separate active centers. Due to their very high surface areas, MOF- based catalysts contain a very high density of fully exposed active site per unit volume. This feature results in enhanced activity, and hence a more effective catalytic system. In addition to the non-coordinated catalytically active metal site catalytically active centers can also be generated from the functional group attached to the ligand. Interestingly, unlike traditional immobilized catalyst, the active catalytic sites generated are predictable and tunable due to the well-known chemical property of linker.<sup>[54]</sup>

### **1.2.8 Graphene MOF hybrid composites**

Graphene can be chemically modified with various functional groups such as benzoic acid and graphene oxide. Oxygen containing functional groups provide coordination center for metal ions and can be utilized for the synthesis of graphene MOF hybrid composites. Oxygen functionality present on graphene basal plane will modulate the growth mechanism of MOF crystals; also graphene may act as nucleation center for the growth of MOF crystals. Large area functionalized graphene sheets can be used to grow MOF nanocrystals with many interesting property due to the synergistic effect of MOF and graphene. Further such hybrid composites may have different adsorption property in comparison to parent MOF. MOFs are known to be insulators but such composites are conducting due to high conductivity of graphene. Interesting optical properties of graphene have been studied, MOFs are also known for certain interesting optical properties. Study of optical properties of such hybrid composites will be interesting. Chapters 2, 3 and 4 explore some of the interesting properties-graphene MOF hybrid composites.



**References:**

- [1] L. Pauling, *Cornell University Press, Ithaca, NY, 1960* 1960.
- [2] R. F. Curl, *Reviews of Modern Physics* 1997, 69, 691-702.
- [3] R. E. Smalley, *Reviews of Modern Physics* 1997, 69, 723-730.
- [4] S. Iijima, *Nature* 1991, 354, 56-58.
- [5] K. S. Novoselov, A. K. Geim, S. V. Morozov, D. Jiang, Y. Zhang, S. V. Dubonos, I. V. Grigorieva, A. A. Firsov, *Science* 2004, 306, 666-669.
- [6] A. K. Geim, K. S. Novoselov, *Nat Mater* 2007, 6, 183-191.
- [7] C. N. R. Rao, A. K. Sood, K. S. Subrahmanyam, A. Govindaraj, *Angewandte Chemie International Edition* 2009, 48, 7752-7777.
- [8] X. Wan, Y. Huang, Y. Chen, *Accounts of Chemical Research* 2012, 45, 598-607.
- [9] C. Lee, X. Wei, J. W. Kysar, J. Hone, *Science* 2008, 321, 385-388.
- [10] H. Chang, H. Wu, *Advanced Functional Materials* 2012, n/a-n/a.
- [11] I. V. Lightcap, P. V. Kamat, *Accounts of Chemical Research* 2012.
- [12] K. S. Subrahmanyam, L. S. Panchakarla, A. Govindaraj, C. N. R. Rao, *The Journal of Physical Chemistry C* 2009, 113, 4257-4259.
- [13] S. Park, J. An, J. R. Potts, A. Velamakanni, S. Murali, R. S. Ruoff, *Carbon* 2011, 49, 3019-3023.
- [14] N. D. Mermin, *Physical Review* 1968, 176, 250-254.
- [15] J. C. Meyer, A. K. Geim, M. I. Katsnelson, K. S. Novoselov, T. J. Booth, S. Roth, *Nature* 2007, 446, 60-63.
- [16] B. Partoens, F. M. Peeters, *Physical Review B* 2006, 74, 075404.
- [17] S. V. Morozov, K. S. Novoselov, F. Schedin, D. Jiang, A. A. Firsov, A. K. Geim, *Physical Review B* 2005, 72, 201401.
- [18] Y. Zhang, J. P. Small, M. E. S. Amori, P. Kim, *Physical Review Letters* 2005, 94, 176803.
- [19] J. N. Coleman, *Accounts of Chemical Research* 2012, 46, 14-22.
- [20] B. C. Brodie, *Philosophical Transactions of the Royal Society of London* 1859, 149, 249-259.
- [21] H. He, T. Riedl, A. Lerf, J. Klinowski, *The Journal of Physical Chemistry* 1996, 100, 19954-19958.
- [22] S. Stankovich, D. A. Dikin, R. D. Piner, K. A. Kohlhaas, A. Kleinhammes, Y. Jia, Y. Wu, S. T. Nguyen, R. S. Ruoff, *Carbon* 2007, 45, 1558-1565.
- [23] H.-J. Shin, K. K. Kim, A. Benayad, S.-M. Yoon, H. K. Park, I.-S. Jung, M. H. Jin, H.-K. Jeong, J. M. Kim, J.-Y. Choi, Y. H. Lee, *Advanced Functional Materials* 2009, 19, 1987-1992.
- [24] V. H. Pham, T. V. Cuong, T.-D. Nguyen-Phan, H. D. Pham, E. J. Kim, S. H. Hur, E. W. Shin, S. Kim, J. S. Chung, *Chemical Communications* 2010, 46, 4375-4377.
- [25] X. Zhou, J. Zhang, H. Wu, H. Yang, J. Zhang, S. Guo, *The Journal of Physical Chemistry C* 2011, 115, 11957-11961.
- [26] C. Zhu, S. Guo, Y. Fang, S. Dong, *ACS Nano* 2010, 4, 2429-2437.
- [27] J. Zhang, H. Yang, G. Shen, P. Cheng, J. Zhang, S. Guo, *Chemical Communications* 2010, 46, 1112-1114.
- [28] G. Wang, J. Yang, J. Park, X. Gou, B. Wang, H. Liu, J. Yao, *The Journal of Physical Chemistry C* 2008, 112, 8192-8195.
- [29] S. Park, Y. Hu, J. O. Hwang, E.-S. Lee, L. B. Casabianca, W. Cai, J. R. Potts, H.-W. Ha, S. Chen, J. Oh, S. O. Kim, Y.-H. Kim, Y. Ishii, R. S. Ruoff, *Nat Commun* 2012, 3, 638.
- [30] K. S. Kim, Y. Zhao, H. Jang, S. Y. Lee, J. M. Kim, K. S. Kim, J.-H. Ahn, P. Kim, J.-Y. Choi, B. H. Hong, *Nature* 2009, 457, 706-710.
- [31] S.-Y. Kwon, C. V. Ciobanu, V. Petrova, V. B. Shenoy, J. Bareño, V. Gambin, I. Petrov, S. Kodambaka, *Nano Letters* 2009, 9, 3985-3990.
- [32] P. W. Sutter, J.-I. Flege, E. A. Sutter, *Nat Mater* 2008, 7, 406-411.
- [33] J. Coraux, A. T. N'Diaye, C. Busse, T. Michely, *Nano Letters* 2008, 8, 565-570.



- [34] C. N. R. Rao, K. S. Subrahmanyam, H. S. S. R. Matte, B. Abdulhakeem, A. Govindaraj, B. Das, P. Kumar, A. Ghosh, D. J. Late, *Science and Technology of Advanced Materials* 2010, *11*, 054502.
- [35] S. Bae, H. Kim, Y. Lee, X. Xu, J.-S. Park, Y. Zheng, J. Balakrishnan, T. Lei, H. Ri Kim, Y. I. Song, Y.-J. Kim, K. S. Kim, B. Ozyilmaz, J.-H. Ahn, B. H. Hong, S. Iijima, *Nat Nano* 2010, *5*, 574-578.
- [36] J. J. Wang, M. Y. Zhu, R. A. Outlaw, X. Zhao, D. M. Manos, B. C. Holloway, V. P. Mammana, *Appl. Phys. Lett.* 2004, *85*, 1265-1267.
- [37] J. Wang, M. Zhu, R. A. Outlaw, X. Zhao, D. M. Manos, B. C. Holloway, *Carbon* 2004, *42*, 2867-2872.
- [38] M. Zhu, J. Wang, B. C. Holloway, R. A. Outlaw, X. Zhao, K. Hou, V. Shutthanandan, D. M. Manos, *Carbon* 2007, *45*, 2229-2234.
- [39] Z. H. Ni, H. M. Wang, J. Kasim, H. M. Fan, T. Yu, Y. H. Wu, Y. P. Feng, Z. X. Shen, *Nano Letters* 2007, *7*, 2758-2763.
- [40] J. Kim, L. J. Cote, F. Kim, J. Huang, *Journal of the American Chemical Society* 2010, *132*, 260-267.
- [41] L. S. Panchakarla, K. S. Subrahmanyam, S. K. Saha, A. Govindaraj, H. R. Krishnamurthy, U. V. Waghmare, C. N. R. Rao, *Advanced Materials* 2009, *21*, 4726-4730.
- [42] M. A. Pimenta, G. Dresselhaus, M. S. Dresselhaus, L. G. Cancado, A. Jorio, R. Saito, *Physical Chemistry Chemical Physics* 2007, *9*, 1276-1290.
- [43] L. M. Malard, M. A. Pimenta, G. Dresselhaus, M. S. Dresselhaus, *Physics Reports* 2009, *473*, 51-87.
- [44] B. Das, K. E. Prasad, U. Ramamurty, C. N. R. Rao, *Nanotechnology* 2009, *20*, 125705.
- [45] K. E. Prasad, B. Das, U. Maitra, U. Ramamurty, C. N. R. Rao, *Proceedings of the National Academy of Sciences* 2009, *106*, 13186-13189.
- [46] L. Schlapbach, A. Züttel, *Nature* 2001, *414*, 353-358.
- [47] K. S. Subrahmanyam, P. Kumar, U. Maitra, A. Govindaraj, K. P. S. S. Hembram, U. V. Waghmare, C. N. R. Rao, *Proceedings of the National Academy of Sciences* 2011.
- [48] A. Peigney, C. Laurent, E. Flahaut, R. R. Bacsa, A. Rousset, *Carbon* 2001, *39*, 507-514.
- [49] A. Ghosh, K. S. Subrahmanyam, K. S. Krishna, S. Datta, A. Govindaraj, S. K. Pati, C. N. R. Rao, *The Journal of Physical Chemistry C* 2008, *112*, 15704-15707.
- [50] H. S. S. Ramakrishna Matte, K. S. Subrahmanyam, K. Venkata Rao, S. J. George, C. N. R. Rao, *Chemical Physics Letters* 2011, *506*, 260-264.
- [51] J. R. Lomeda, C. D. Doyle, D. V. Kosynkin, W.-F. Hwang, J. M. Tour, *Journal of the American Chemical Society* 2008, *130*, 16201-16206.
- [52] R. Voggu, B. Das, C. S. Rout, C. N. R. Rao, *Journal of Physics: Condensed Matter* 2008, *20*, 472204.
- [53] A. Ghosh, K. V. Rao, S. J. George, C. N. R. Rao, *Chemistry – A European Journal* 2010, *16*, 2700-2704.
- [54] S. Kitagawa, R. Kitaura, S.-i. Noro, *Angewandte Chemie International Edition* 2004, *43*, 2334-2375.
- [55] C. T. Kresge, M. E. Leonowicz, W. J. Roth, J. C. Vartuli, J. S. Beck, *Nature* 1992, *359*, 710-712.
- [56] M. Kruk, M. Jaroniec, C. H. Ko, R. Ryoo, *Chemistry of Materials* 2000, *12*, 1961-1968.
- [57] B. F. Hoskins, R. Robson, *Journal of the American Chemical Society* 1990, *112*, 1546-1554.
- [58] K. S. Park, Z. Ni, A. P. Côté, J. Y. Choi, R. Huang, F. J. Uribe-Romo, H. K. Chae, M. O’Keeffe, O. M. Yaghi, *Proceedings of the National Academy of Sciences* 2006, *103*, 10186-10191.
- [59] G. Gundiah, A. Govindaraj, N. Rajalakshmi, K. S. Dhathathreyan, C. N. R. Rao, *Journal of Materials Chemistry* 2003, *13*, 209-213.
- [60] S. Moussa, A. R. Siamaki, B. F. Gupton, M. S. El-Shall, *ACS Catalysis* 2011, *2*, 145-154.
- [61] N. Kumar, K. S. Subrahmanyam, P. Chaturbedy, K. Raidongia, A. Govindaraj, K. P. S. S. Hembram, A. K. Mishra, U. V. Waghmare, C. N. R. Rao, *ChemSusChem* 2011, *4*, 1662-1670.

- [62] A. Thomas, *Angewandte Chemie International Edition* 2010, 49, 8328-8344.
- [63] P. Markewitz, W. Kuckshinrichs, W. Leitner, J. Linssen, P. Zapp, R. Bongartz, A. Schreiber, T. E. Muller, *Energy & Environmental Science* 2012, 5, 7281-7305.
- [64] M. Eddaoudi, D. B. Moler, H. Li, B. Chen, T. M. Reineke, M. O'Keeffe, O. M. Yaghi, *Accounts of Chemical Research* 2001, 34, 319-330.
- [65] C. N. R. Rao, S. Natarajan, R. Vaidhyanathan, *Angewandte Chemie International Edition* 2004, 43, 1466-1496.
- [66] A. K. Cheetham, C. N. R. Rao, R. K. Feller, *Chemical Communications* 2006, 0, 4780-4795.
- [67] S. Horike, S. Shimomura, S. Kitagawa, *Nat Chem* 2009, 1, 695-704.
- [68] C. N. R. Rao, A. K. Cheetham, A. Thirumurugan, *Journal of Physics: Condensed Matter* 2008, 20, 083202.
- [69] W. J. Rieter, K. M. L. Taylor, H. An, W. Lin, W. Lin, *Journal of the American Chemical Society* 2006, 128, 9024-9025.
- [70] G. Lu, S. Li, Z. Guo, O. K. Farha, B. G. Hauser, X. Qi, Y. Wang, X. Wang, S. Han, X. Liu, J. S. DuChene, H. Zhang, Q. Zhang, X. Chen, J. Ma, S. C. J. Loo, W. D. Wei, Y. Yang, J. T. Hupp, F. Huo, *Nat Chem* 2012, 4, 310-316.
- [71] Y. Cui, Y. Yue, G. Qian, B. Chen, *Chemical Reviews* 2011, 112, 1126-1162.
- [72] F. S. Richardson, *Chemical Reviews* 1982, 82, 541-552.
- [73] A. Thirumurugan, A. K. Cheetham, *European Journal of Inorganic Chemistry* 2010, 2010, 3823-3828.
- [74] M. D. Allendorf, C. A. Bauer, R. K. Bhakta, R. J. T. Houk, *Chemical Society Reviews* 2009, 38, 1330-1352.
- [75] G. Férey, *Chemical Society Reviews* 2008, 37, 191-214.
- [76] H. K. Chae, D. Y. Siberio-Perez, J. Kim, Y. Go, M. Eddaoudi, A. J. Matzger, M. O'Keeffe, O. M. Yaghi, *Nature* 2004, 427, 523-527.
- [77] G. Férey, C. Mellot-Draznieks, C. Serre, F. Millange, J. Dutour, S. Surblé, I. Margiolaki, *Science* 2005, 309, 2040-2042.
- [78] K. Koh, A. G. Wong-Foy, A. J. Matzger, *Journal of the American Chemical Society* 2009, 131, 4184-4185.
- [79] H. Furukawa, N. Ko, Y. B. Go, N. Aratani, S. B. Choi, E. Choi, A. Ö. Yazaydin, R. Q. Snurr, M. O'Keeffe, J. Kim, O. M. Yaghi, *Science* 2010, 329, 424-428.
- [80] Q. Song, S. K. Nataraj, M. V. Roussanova, J. C. Tan, D. J. Hughes, W. Li, P. Bourgoïn, M. A. Alam, A. K. Cheetham, S. A. Al-Muhtaseb, E. Sivaniah, *Energy & Environmental Science* 2012, 5, 8359-8369.

---

# *Quenching of lanthanide emission in composite of graphene with a Bi- based MOF*

---

## *Summary*

Effect of graphene on the optical properties of lanthanide-based graphene-MOF hybrid composites has been investigated. Graphene is found to be a very efficient quencher of lanthanide emission. For this purpose, hybrid composites of a bismuth based MOF [Bi(1,4-bdc)<sub>2</sub>].(dma) [where 1,4-bdc = Benzene-1,4-dicarboxylate anion, dma = dimethyl ammonium cation] doped with lanthanide ions were prepared with different proportions of benzoic acid functionalized graphene (BFG). A large decrease in luminescence intensity is observed even with a very small concentration (2wt.%) of benzoic acid functionalized graphene (BFG). The quantum yield decreased from 50.23% to 1.37% in case of Tb doped samples. Similar effect was observed in Eu doped and Eu/Tb codoped samples. On subsequent addition of higher concentration of functionalized graphene, a small decrease in luminescence intensity and hence fluorescence quenching was observed. The observed fluorescence quenching was further supported by lifetime measurements. The observed quenching of lanthanide emission is attributed to excited state energy/charge transfer from bdc ligand to graphene which perturbs the energy

transfer from ligand to lanthanide metal ion. Even very small concentration of graphene is sufficient to quench lanthanide emission very effectively.

## **2.1 Introduction:**

Graphene due to its interesting electronic, optical, mechanical, chemical and other properties has received great attention.<sup>[1-3]</sup> Fluorescence quenching is one of the important properties of graphene and has been utilized in sensing biomolecules and visualization of graphene sheets on various substrates.<sup>[4-6]</sup> Interaction of graphene and various chemically modified forms of graphene with semiconductor nanoparticles and dye molecules has been studied to understand the mechanism of fluorescence quenching.<sup>[7, 8]</sup> Lanthanide based metal organic frameworks (MOFs) have been studied for their optical, magnetic and catalytic property.<sup>[9-13]</sup> Bi<sup>3+</sup> based frameworks have been recently investigated as hosts for lanthanide ions with interesting optical properties.<sup>[14, 15]</sup> Lanthanide based phosphors and metal organic frameworks have promising optoelectronic applications. Since graphene and various modified forms of graphene have been utilized for various optical and optoelectronic applications,<sup>[16, 17]</sup> we have prepared lanthanide based hybrid graphene composites with metal organic framework. Interaction of graphene with lanthanide based frameworks and its effect on quenching lanthanide emission is largely unexplored. We have carried out detailed investigations of optical properties of such graphene bismuth based MOF hybrid composites. For our present investigations, the bismuth based framework [Bi(1,4-bdc)<sub>2</sub>](dma) (**BDC**) [1,4-bdc = Benzene-1,4-dicarboxylate anion, dma = dimethyl ammonium cation] with lanthanide ion

doping was utilized.<sup>[15]</sup> This lanthanide doped framework shows strong luminescence corresponding to rare earth emission due to very efficient ligand to rare earth ion energy transfer. In order to make uniform composites and provide coordination center to the metal ions graphene basal plane was functionalized with benzoic acid (BFG).<sup>[18]</sup> We discuss properties of the BFG-Ln doped BDC composites in this chapter.

## **2.2 Materials and experiments:**

Graphite powder used for synthesizing RGO was obtained from Alfa Aesar. Terephthalic acid,  $\text{Eu}(\text{NO}_3)_3 \cdot 5\text{H}_2\text{O}$  and  $\text{Tb}(\text{NO}_3)_3 \cdot 5\text{H}_2\text{O}$  were obtained from Sigma Aldrich.  $\text{Bi}(\text{NO}_3)_3 \cdot 5\text{H}_2\text{O}$  was obtained from SRL Chemicals. DMF,  $\text{KMnO}_4$ ,  $\text{NaNO}_3$  and other chemicals were obtained from Merck chemicals. All the chemicals were of high purity and used without further purification.

### **Synthesis of Graphite Oxide:**

Graphite oxide was prepared using a modified Hummers and Offeman method. In an ice bath 75 ml conc.  $\text{H}_2\text{SO}_4$ , 1.5 g graphite powder and 1.5 g  $\text{NaNO}_3$  were added and stirred for 10 min to make uniform mixture. To this mixture, 10 g  $\text{KMnO}_4$  was slowly added. The reactants were allowed to mix properly then transferred to an oil bath maintained at 40 °C and stirred for 45 min. Oxidation of graphite powder occurred and dark brown coloured viscous product formed. 75 ml distilled water was slowly added followed with stirring for another 15 min at 70 °C. Brown color suspension formed. The

temperature was then raised to 80 °C followed by the addition of 15 ml H<sub>2</sub>O<sub>2</sub> in 150 ml warm water (~70 °C). Colour of suspension changed from dark brown to yellow. Obtained product was centrifuged then washed repeatedly with distilled water to remove excess acid. The product was again dispersed in water and dialyzed for 24 hours to remove any residual acid. GO suspension was then centrifuged to remove excess water. Obtained solid product was transferred to petri dish and kept in vacuum at room temperature for drying.

### **Reduction of Graphite Oxide:**

Obtained graphite oxide was dispersed in water and reduced using NaBH<sub>4</sub> according to procedure reported in literature.<sup>[33]</sup> In a round bottom flask 400 mg of GO was dispersed in 320 ml water by sonication. The pH was adjusted to 10 by adding 5% Na<sub>2</sub>CO<sub>3</sub> solution. Then, the dispersion was stirred at 90 °C for 9 hours. The pH was again checked using a pH meter and adjusted to 10. Then, 3.2g NaBH<sub>4</sub> (0.085 mol) in 80 ml H<sub>2</sub>O was added to dispersion under constant stirring, with temperature maintained at 80 °C. The dispersion was stirred for next 3 hours. The color of dispersion changed from dark brown to black accompanied by outgassing. The final product was filtered and washed several times with water and ethanol and dried under vacuum.

### **Benzoic Acid functionalization of Graphene (BFG):**

Functionalization of graphene was performed by making diazonium salt of *para*-aminobenzoic acid. In 80 ml water 960mg *para*-aminobenzoic acid and 280mg NaOH (7mmol) were added. In the solution 526 mg NaNO<sub>2</sub> and 6ml 20%HCl (6.4M, 19.2

mmol) were added with temperature maintained at 0 °C and stirred for 45min. The color of solution changed to pale yellow due to the formation of diazonium salt. RGO (300mg) was dispersed in water by sonication in 1 wt.% sodium dodecylbenzenesulfonate (SDBS) solution. RGO dispersion was added to diazonium salt solution and stirred at 0°C for 4 hours. Then, ice bath was removed and stirred for another 4 hours at room. The resulting dispersion was filtered and washed with ethanol water mixture, ethanol and acetone to remove the surfactant. TEM images of RGO and characterization of RGO and BFG are given in Figure 2.1.

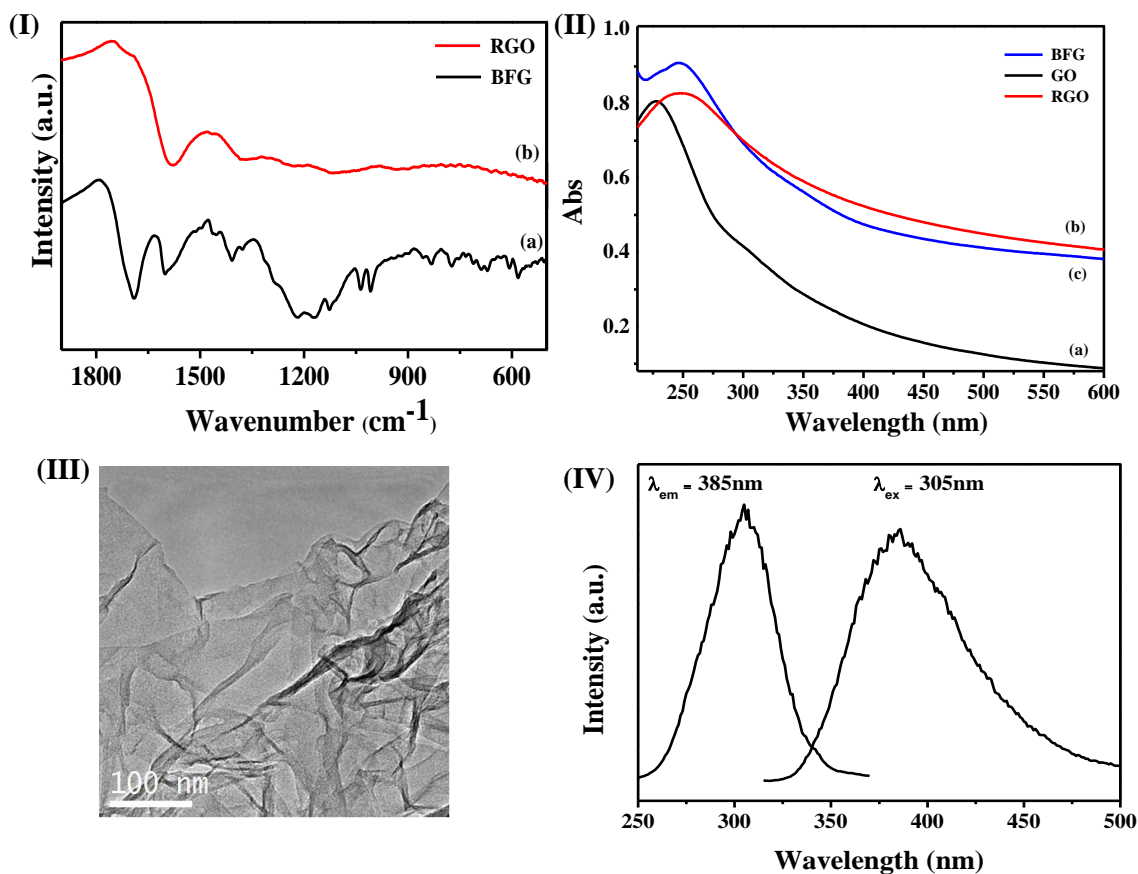


**Figure 2.1** (I) Infrared spectra of (a) RGO (red) and (b) BFG (Black). (II) UV- Visible absorbance spectra of (a) GO (black) (b) RGO (red) and (c) BFG (blue). (III) TEM image of RGO. (IV) PL excitation and emission spectra of BFG.

In reduced graphene oxide (RGO) Strong peak at  $1577\text{ cm}^{-1}$  due to C=C bond vibration and a very weak shoulder near  $1700\text{ cm}^{-1}$  due to remaining carboxylic acid was observed (Figure 2.1(I)). Very low intensity of carboxylic acid peak is due to efficient reduction of graphene oxide. In benzoic acid functionalized graphene (BFG) strong peak at  $1691\text{ cm}^{-1}$  due to COOH functional group is present. Peak at  $1600\text{ cm}^{-1}$  in BFG is due to C=C stretching vibration. UV-Visible absorption spectra of GO, RGO and BFG were collected by dispersing in water. GO showed absorption maxima at 227 due to  $\pi\rightarrow\pi^*$  transition (Figure 2.1(II)). In RGO  $\pi\rightarrow\pi^*$  transition absorption maxima peak was red shifted to 250 nm due to partial recovery of conjugation after reduction. Red shift in  $\pi\rightarrow\pi^*$  was also observed in BFG with the absorption maximum at 247nm. . TEM image of reduced graphene oxide (RGO) used for the benzoic acid functionalization of graphene are given in figure 2.1(III). RGO synthesized using sodium borohydride as reducing agent were agglomerated due to strong  $\pi$ - $\pi$  interaction between graphene sheets. PL excitation and emission spectrum of BFG is given in figure 2.1(IV).

### **BDC ([Bi(1,4-bdc<sub>2</sub>)].dma) and BDCG graphene composite:**

Benzoic acid functionalized graphene was dispersed in 5 ml DMF by sonication for 45 mins. Benzoic acid functional group present of graphene helped in dispersing graphene sheets in DMF. A stable colloidal dispersion of BFG was obtained. To the colloidal dispersion of BFG, Bi(NO<sub>3</sub>)<sub>3</sub>.5H<sub>2</sub>O (0.3 mmol), 1,4H<sub>2</sub>bdc (1.5 mmol, Benzene-1,4-dicarboxylic acid), Him (1.2 mmol, Imidazole), dmf (N,N-Dimethylformamide) were added and stirred for 30 min to form a homogeneous mixture. The homogeneous



mixture was sealed in a 23 ml stainless steel reactor with a PTFE liner and heated at 100 °C for 72 hours, then cooled to room temperature. 10 mol%  $\text{Eu}^{3+}$ ,  $\text{Tb}^{3+}$ , and 5 mol% each  $\text{Eu}^{3+}/\text{Tb}^{3+}$  doped BDC/BFG composites were obtained by replacing stoichiometric amounts of Eu/Bi and Tb/Bi nitrates. BDC1 and rare earth doped BDC1 were obtained by the same procedure without adding functionalized graphene. The product was filtered, washed with dmf and acetone and dried at room temperature.

## Physical Measurements

Powder X-ray diffraction (PXRD) pattern of all samples were recorded with a Bruker D8 X-ray diffractometer with  $\text{Cu K}\alpha$  radiation. Raman spectra were recorded using Jobin Yvon LabRam HR spectrometer with 632.8 nm HeNe laser in backscattering geometry. Infrared spectra were recorded on a Bruker IFS 66v/S using KBr pellets. Thermogravimetric analysis (TGA) was carried out on Mettler Toledo TGA850 instrument with a heating rate of 10 °C/min in air. FESEM images were obtained from Nova Nano SEM 600, FEI Company. Transmission electron microscope images of samples were obtained with a JEOL JEM 3010 microscope operating at an accelerating voltage of 300 kV. Photoluminescence measurements of solid samples were carried out using Flurolog-3 spectrophotometer from Horiba Jobin Yvon. PL measurements of solid samples were done by taking approximately equal amount of sample and placing between quartz plates. Illumination area of sample was kept constant during measurement. Lifetime measurements were carried out on Edinburgh PL spectrometer using pulsed Xenon lamp.

## 2.3 Results and Discussion:

BDC and BDC graphene composites BDCG with different concentration of graphene and Eu/Tb doping was synthesized using solvothermal route. The samples were prepared with three different benzoic acid functionalized graphene (BFG) concentration 3 mg (BDC3G), 6 mg (BDC6G) and 9 mg (BDC9G) which corresponds to approximately 2 wt.%, 4 wt.% and 6 wt.% of BFG respectively based on 86% observed yield. BDC host framework and corresponding composites were doped with 10 mol % Eu, 10 mol % Tb and 5 mol % Eu/ 5 mol % Tb respectively. Obtained BDC and BDCG were characterized with PXRD (Figure 2.2) to check phase purity and were consistent with simulated pattern.

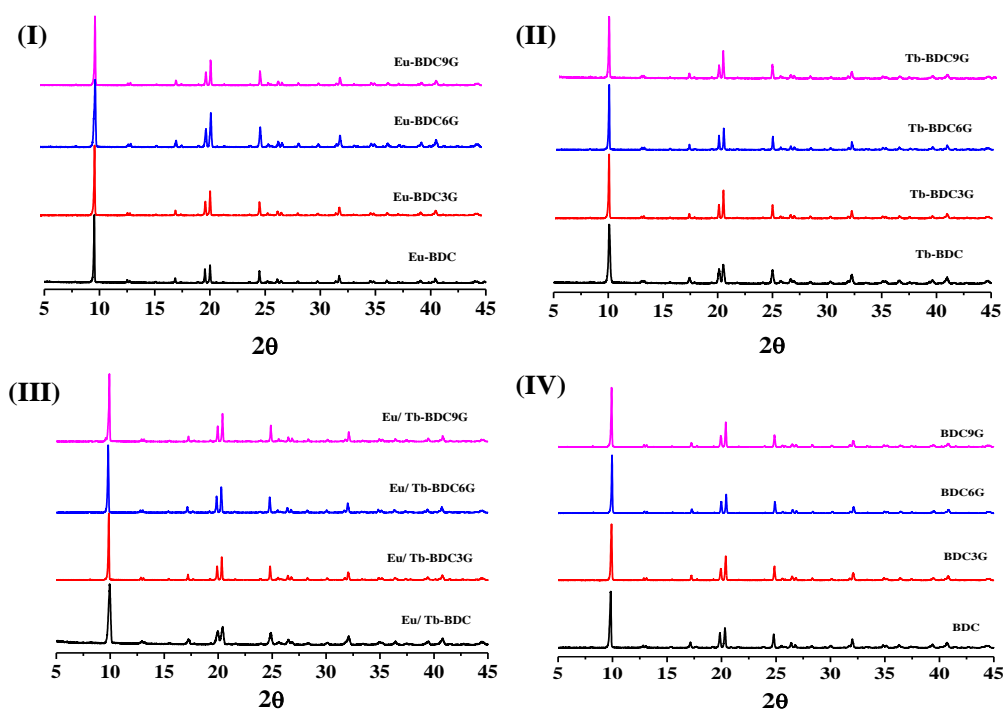


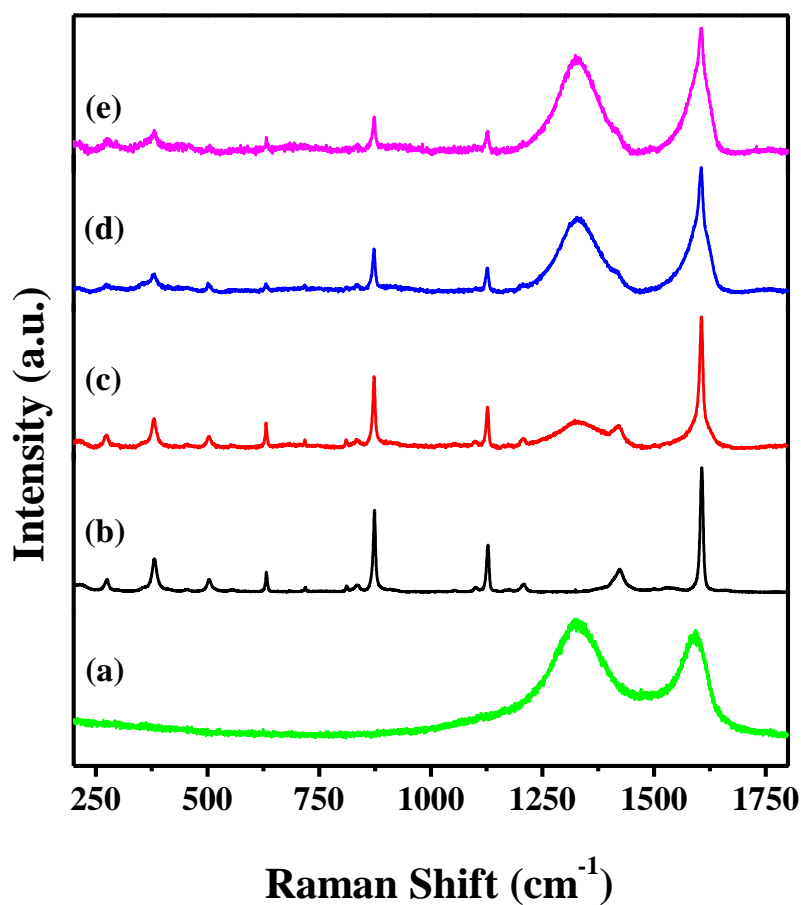
**Figure 2.2** PXRD pattern of lanthanide doped BDC and BDCG. **(I)** Eu doped BDC and BDCG. **(II)** Tb doped BDC and BDCG. **(III)** Eu/Tb doped BDC and BDCG. **(IV)** undoped BDC. 3G, 6G and 9G correspond to 3 mg, 6 mg and 9 mg of functionalized graphene respectively. BDC 3 mg, 6 mg, and 9 mg, BFG composites are represented in black, red, blue and magenta respectively.

No change was observed in PXRD pattern between BDC and BDCG. BDC crystallizes in rhombohedral  $R\bar{3}c$  space group with two crystallographically different  $\text{Bi}^{3+}$  cation. Two different  $\text{Bi}^{3+}$  sites B1 and B2 corresponds to twelve and nine coordination with a stereochemically inactive lone pair of electrons. The dma cation occupy space between the bdc anion by hydrogen bonding interaction with the oxygen atom of carboxylate group. Overall the framework forms a dense structure without any void space.

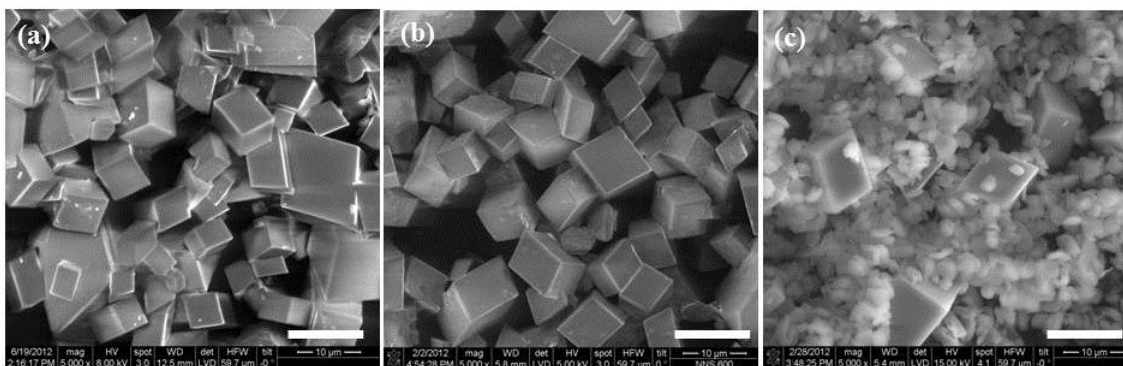
Raman spectroscopy gives an important insight on the homogeneity and quality of nanocarbon composites.<sup>[19]</sup> Figure 2.3 shows the Raman spectra of BFG, BDC and BDCG. Raman spectra were collected in backscattering geometry using 632.8 nm He Ne laser by focusing on individual cube shaped crystals. BFG shows characteristic D and G band at  $1330\text{ cm}^{-1}$  and  $1593\text{ cm}^{-1}$  respectively. Peaks at  $631\text{ cm}^{-1}$ ,  $836\text{ cm}^{-1}$  and  $874\text{ cm}^{-1}$  in BDC and BDCG can be assigned to out of plan deformation modes of the C-H bond in benzene ring of 1,4-bdc ligand. Peaks at  $1425\text{ cm}^{-1}$  and  $1607\text{ cm}^{-1}$  are due to the stretching modes of carboxylate groups and symmetric benzene ring stretching vibration.<sup>[20]</sup> In addition to the Raman modes corresponding to BDC, characteristic D and G bands of graphene at  $1330\text{ cm}^{-1}$  and  $1593\text{ cm}^{-1}$  were observed in BDCG. G band at  $1593\text{ cm}^{-1}$  merged with  $1607\text{ cm}^{-1}$  peak. Intensity of D and G bands increased from BDC3G to BDC6G and BDC9G which is consistent with increasing graphene concentration.

FESEM images of BDC and BDCG (Figure 2.4) showed cube shaped morphology for both BDC and BDCG. No significant change in morphology was observed for graphene composites in comparison to pure MOF. The BDC and BDCG crystals were very uniform with cubic morphology and average size variation between  $5\text{ }\mu\text{m}$  to  $10\text{ }\mu\text{m}$ . An

important role of pH was observed in morphology of BDC crystals. In acidic environment BDC1 crystallized in thin approximately 1 $\mu\text{m}$  plate shaped crystals with small concentration of cubic morphology crystals. In the presence of functionalized graphene even in acidic environment always cube shaped crystals formed which may be due to functionalized graphene sheets acting as nucleation center for the growth of MOF crystals

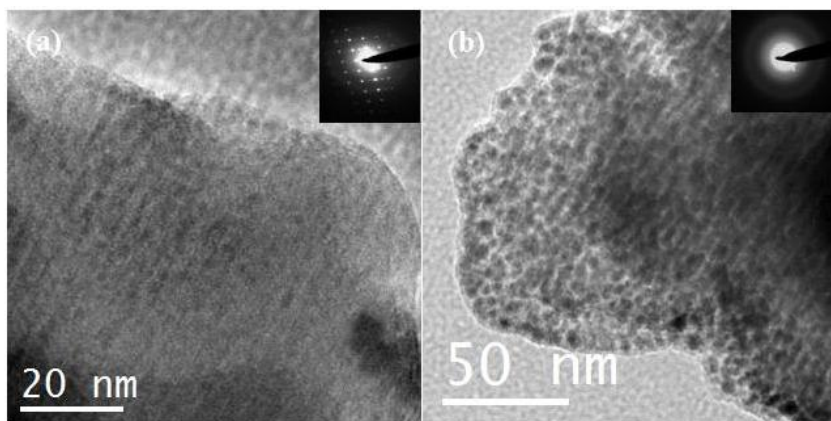


**Figure 2.3** Raman spectra of (a) Benzoic acid functionalized graphene (BFG) (b) Eu doped BDC (c) Eu-BDC3G (d) Eu-BDC6G and (e) Eu-BDC9G. Eu-BDC corresponds to Eu doped BDC. 3G, 6G, and 9G correspond to 3 mg, 6 mg and 9 mg of functionalized graphene respectively.



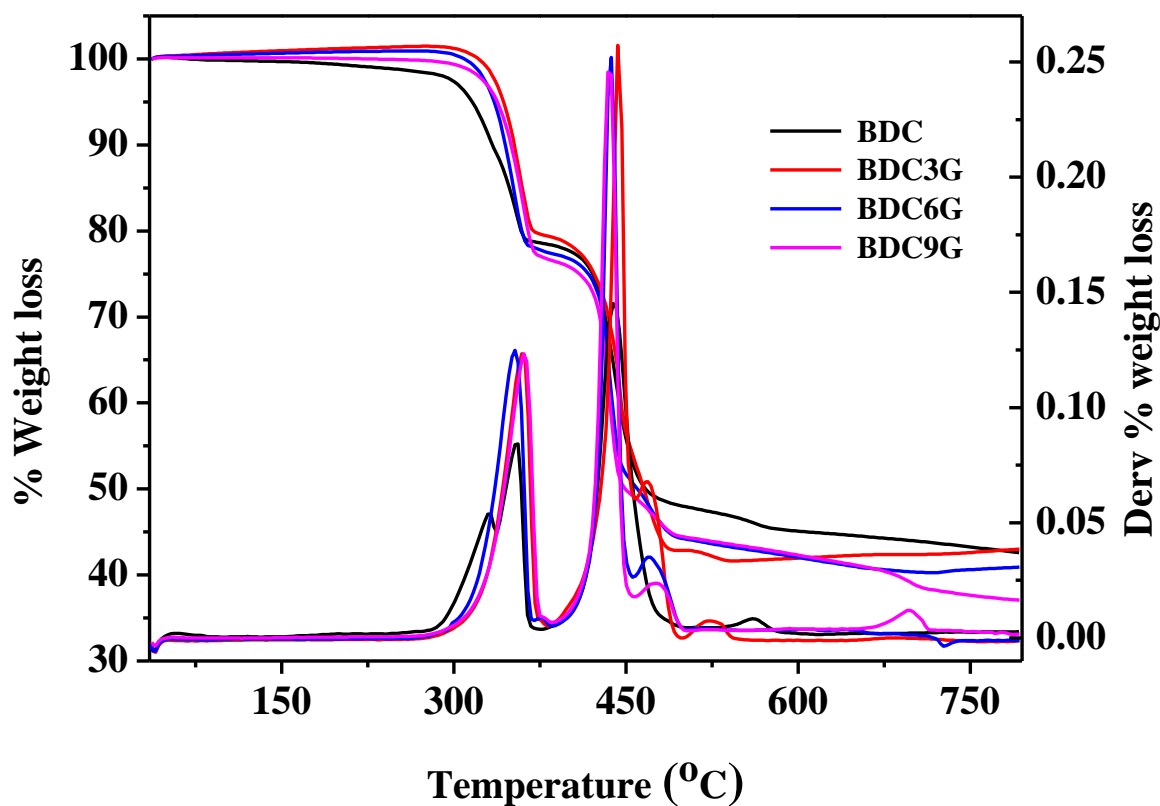
**Figure 2.4** FESEM images of (a) Eu-BDC (b) Eu-BDC9G (c) Eu-BDC in acidic condition. Scale bar corresponds to 10 µm.

TEM image of composites are given in figure 2.5. BDCG composites were highly crystalline and electron diffraction pattern was observed. When the crystals were grinded and sonicated for 45 min uniform cubic structure collapsed and approximately 10 nm MOF particles strongly agglomerated and supported by graphene sheets was observed.

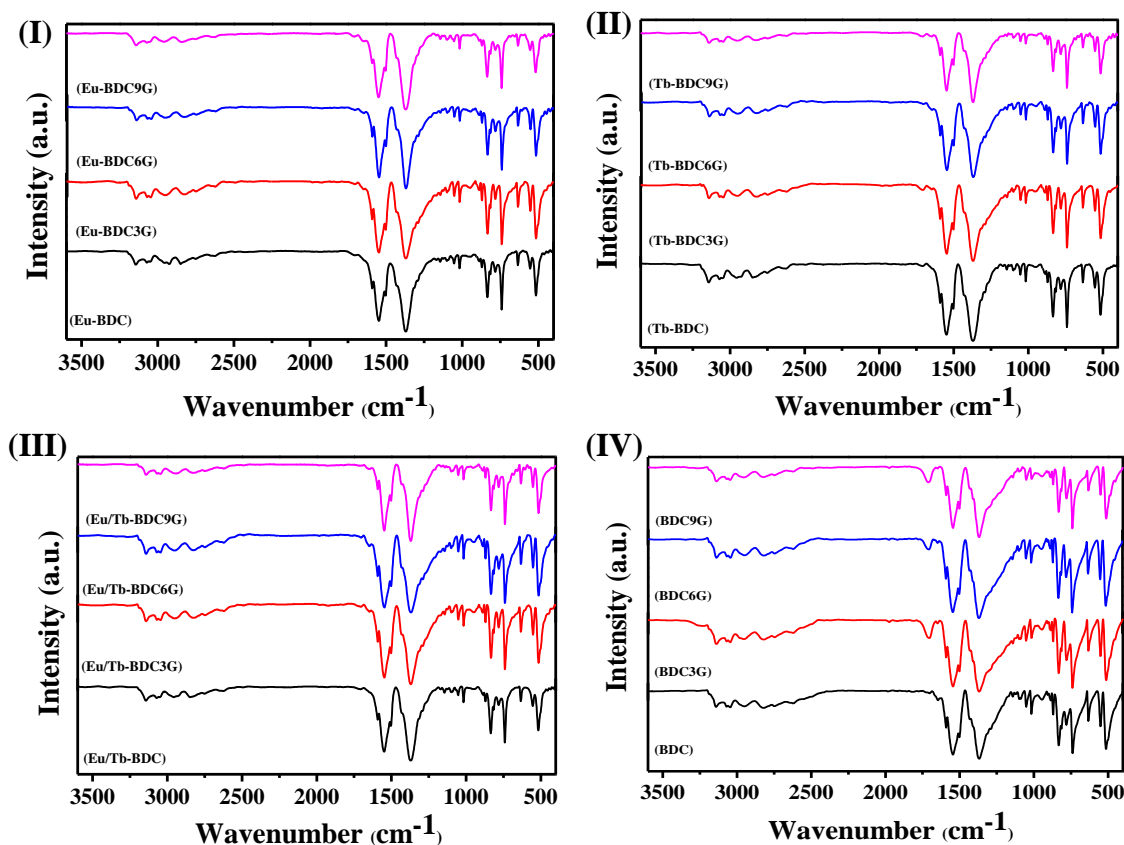


**Figure 2.5** TEM images of (a) Eu-BDC9G and (b) Eu-BDC9G after grinding and 45 min sonication.

Thermogravimetric analysis (Figure 2.6) of BDC and different concentration graphene composites BDCG showed two step weight loss. First weight loss near 300 °C is due to the loss of dmf molecules and second weight loss at 400 °C is due to the decomposition of framework structure. TGA showed similar thermal stability for BDCG and BDC. Thermal stability of graphene MOF composites (BDCG) shows that composites are homogeneous with high thermal stability. Infrared spectrums of all the compounds are given in figure 2.7.



**Figure 2.6** TG analysis of BDC and BDCG. TGA was carried out at a heating rate of 10 °C in air.



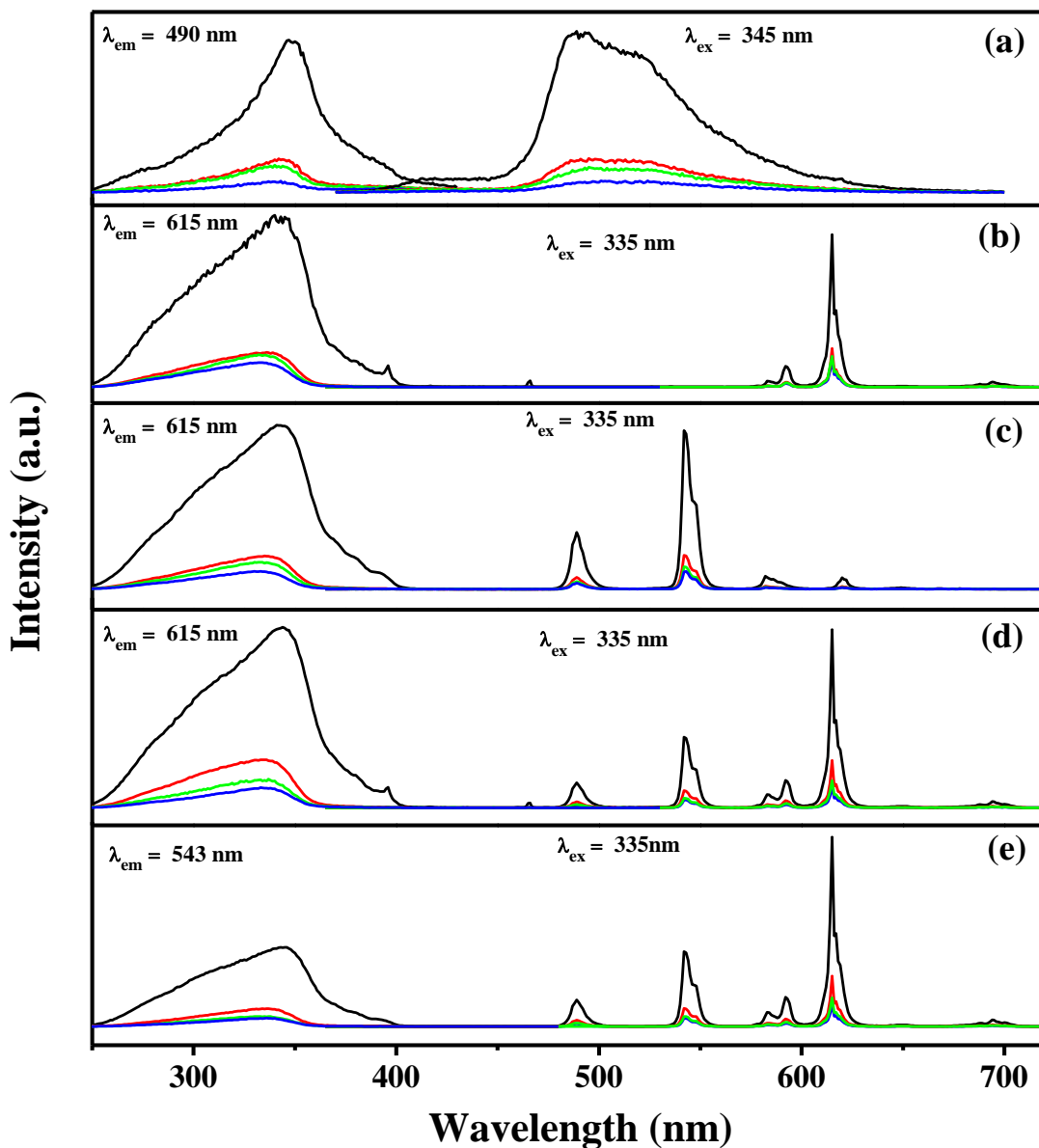
**Figure 2.7** Infrared spectra of lanthanide doped BDC and BDCG. **(I)** Eu doped BDC and BDCG. **(II)** Tb doped BDC and BDCG. **(III)** Eu/Tb doped BDC and BDCG. **(IV)** undoped BDC. 3G, 6G and 9G correspond to 3 mg, 6mg and 9mg of functionalized graphene respectively. BDC 3 mg, 6mg, and 9mg, BFG composites are represented in black, red, blue and magenta respectively

Figure 2.8 shows the photoluminescence spectrum of BDC, BDCG and rare earth doped BDCG. Very efficient fluorescence quenching of lanthanide emission was observed. BDC showed broad emission with maximum at approximately 490 nm on excitation at 345 nm. This broad emission spectrum is due to intraligand luminescence or charge-transfer transitions. On addition of first 3 mg of BFG large decrease in emission intensity was observed followed by small decrease in intensity on subsequent addition of 6 mg and 9 mg functionalized graphene. Eu doped BDC showed very strong characteristic

peak at 615 nm corresponding to  ${}^5D_0 \rightarrow {}^7F_2$  transition at 335 nm excitation wavelength. Low intensity peaks at 583 nm, 592 nm and 695 nm can be attributed to  ${}^5D_0 \rightarrow {}^7F_J$  ( $J = 0, 1, 4$ ) transitions. Low intensity peak at 583 nm due to  ${}^5D_0 \rightarrow {}^7F_0$  suggests that  $\text{Eu}^{3+}$  occupy a low symmetry site without an inversion center.<sup>[21]</sup> Asymmetric ratio of  ${}^5D_0 \rightarrow {}^7F_2 / {}^5D_0 \rightarrow {}^7F_1$  transition was 6.2, which indicates that  $\text{Eu}^{3+}$  ion occupy highly asymmetric site.<sup>[22, 23]</sup> With the addition of first 3 mg functionalized graphene strong quenching of  $\text{Eu}^{3+}$  emission was observed followed by small decrease in emission intensity on subsequent addition of 6 mg and 9 mg functionalized graphene. Tb doped BDC showed sharp emission peaks at 489 nm, 543 nm, 582 nm and 620 nm due to  ${}^5D_4 \rightarrow {}^7F_J$  ( $J = 6, 5, 4, 3$ ) transitions at 335 nm excitation wavelength. Peak at 543 nm due to  ${}^5D_4 \rightarrow {}^7F_5$  is the most intense peak. Similar to Eu doped BDC very strong quenching of Tb emission was observed on the addition of first 3 mg functionalized graphene followed by slight decrease in emission intensity for samples containing 6 mg and 9mg functionalized graphene. Eu and Tb Codoped samples showed emission peaks corresponding to  $\text{Tb}^{3+}$  at 489 nm and 543 nm due to  ${}^5D_4 \rightarrow {}^7F_J$  ( $J = 6, 5$ ) transitions. Peaks at 583 nm, 592 nm, 615 nm and 695 nm are due to  ${}^5D_0 \rightarrow {}^7F_J$  ( $J = 0, 1, 2, 4$ ) transitions of  $\text{Eu}^{3+}$  at 335 nm excitation. In addition to the observed peaks very weak intensity peak at 649 nm due to  ${}^5D_0 \rightarrow {}^7F_3$  transition is also present in Eu doped and Eu/Tb codoped samples but is not observable due to very high intensity of 615 nm electric-dipole transition. Observed lanthanide emission quenching in Eu/Tb codoped samples due to excited state interactions with graphene were similar to Eu and Tb doped samples. The emission band of the intraligand luminescence was not observed in the emission spectra of all the rare earth doped compounds suggesting very efficient energy transfer



from ligand to rare earth ions. Lanthanide ion emission was strong and red, green and orange emission can be observed with naked eye for Eu, Tb and Eu/Tb doped BDC respectively.



**Figure 2.8** PL excitation and emission spectra of (a) BDC (black), BDC3G (red), BDC6G (green) and BDC9G (blue) (b) Eu-BDC (black), Eu-BDC3G (red), Eu-BDC6G (green) and Eu-BDC9G (blue) (c) Tb-BDC (black), Tb-BDC3G (red) and Tb-BDC6G (green) and Tb-BDC9G (blue) (d,e) Eu/Tb-BDC (black), Eu/Tb-BDC3G (red), Eu/Tb-BDC6G (green) and Eu/Tb-BDC9G (blue) with excitation spectra monitored at 615 nm and 543 nm corresponding to  $\text{Eu}^{3+}$  and  $\text{Tb}^{3+}$  respectively.

Figure 2.9 shows the image of lanthanide doped BDC and BDC3G samples corresponding to 3 mg of functionalized graphene under UV light. Quenching of rare earth emission can be easily observed. Very strong luminescence of lanthanide doped BDC shows that bismuth based framework is very efficient host for lanthanide ions in designing high quantum efficiency phosphors.

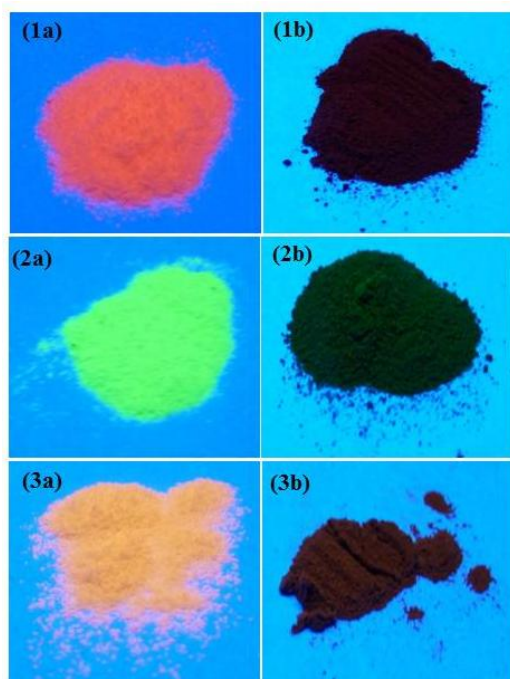


**Figure 2.9** Figure (1a, b) Eu-BDC and Eu-BDC3G (2a, b) Tb-BDC and Tb-BDC3G (3a, b) Eu/Tb-BDC and Eu/Tb-BDC3G on UV light excitation. 3G corresponds to 3mg of benzoic acid functionalized graphene.

Consistent with observed quenching of rare earth emission fluorescence decay measurement showed decrease in lifetime in rare earth doped graphene MOF composites. Figure 2.10 shows the lifetime trend of rare earth doped BDC and BDCG samples. The  $^5D_0$  decay time of Eu doped samples were monitored using the strongest  $^7F_2$  component at 615 nm using excitation wavelength of 335 nm. The lifetime Eu-BDCG decreases with increasing BFG concentration which is consistent with observed quenching of Eu emission. The  $^5D_4$  decay time of Tb doped samples were monitored using  $^7F_5$  component

at 543 nm. Both  $^5D_0$  and  $^5D_4$  decay time corresponding to  $\text{Eu}^{3+}$  and  $\text{Tb}^{3+}$  were monitored for Eu/Tb codoped samples. The  $^5D_0$  and  $^5D_4$  decay time corresponding to  $\text{Eu}^{3+}$  and  $\text{Tb}^{3+}$  codoping were monitored using  $^7F_2$  and  $^7F_5$  transitions respectively. Similar to Eu doped samples lifetime decreased in Tb doped and Eu/Tb codoped BDCG with increasing BFG concentration. The decrease in lifetime is consistent with observed quenching in Eu and Tb emission. Lifetime value of lanthanide doped BDC and BDCG are given in table 1.

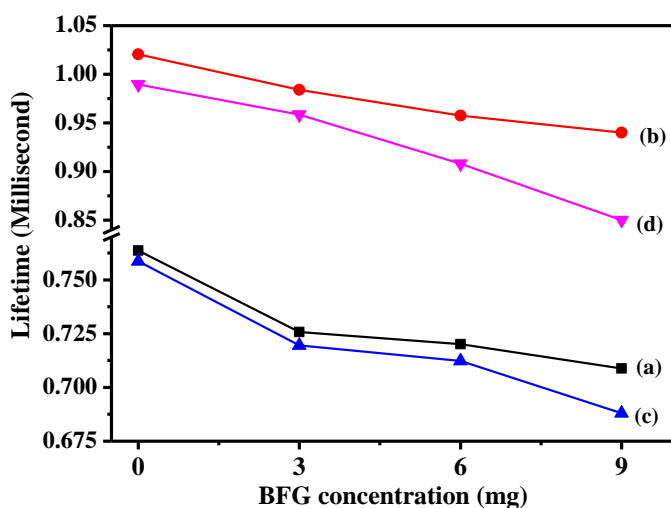


**Figure 2.10** Lifetime value with increasing functionalized graphene concentration (a) Eu doped (black) (b) Tb doped (red) (c, d) Eu/Tb codoped samples corresponding to Eu (615 nm, blue) and Tb (543 nm, magenta) emission respectively.

| BFG Concentration (mg) | Eu doped ( $\lambda_{em}=615\text{ nm}$ ) Lifetime (ms) | Tb doped ( $\lambda_{em}=543\text{ nm}$ ) Lifetime (ms) | Eu/Tb doped ( $\lambda_{em}=615\text{ nm}$ ) Lifetime (ms) | Eu/Tb doped ( $\lambda_{em}=543\text{ nm}$ ) Lifetime (ms) |
|------------------------|---|---|--|--|
| 0                      | 0.76373   | 1.02058   | 0.75874  | 0.98942  |
| 3                      | 0.72575   | 0.98408   | 0.71958  | 0.95849  |
| 6                      | 0.72011   | 0.9574  | 0.71235  | 0.90799  |
| 9                      | 0.70884   | 0.93987   | 0.68801  | 0.85004  |

**Table 1** Lifetime value of lanthanide doped BDC and BDC graphene composites with increasing graphene concentration.

Composites of semiconductor nanoparticle with graphene oxide and carbon nanotube show quenching of semiconductor nanoparticle emission.<sup>[7, 24, 25]</sup> Similar behavior of graphene as a very efficient quencher for aromatic molecule fluorescence has been observed.<sup>[8, 26]</sup> Graphene and its various functionalized forms acts as an electron acceptor and provide an additional non radiative decay pathway.<sup>[7, 8]</sup> Although charge transfer has been explained as one of the mechanism, fluorescence quenching of dye molecules have been observed at 4 nm distance which cannot be explained by charge transfer mechanism.<sup>[27]</sup> Both energy transfer and charge transfer plays a role in fluorescence quenching property of graphene.<sup>[7, 8, 27, 28]</sup> High intensity of lanthanide (Eu, Tb) emission in BDC is due to very efficient energy transfer from bdc anion to lanthanide ions on UV excitation. Energy transfer from photo excited bdc anion to graphene may be responsible for observed quenching of rare earth emission. Charge transfer from photo excited bdc anion to graphene cannot be ruled out due to the close proximity of bdc anion and graphene in the MOF crystal. Excited state charge transfer interaction between graphene and aromatic molecules has been observed in earlier study. The observed quenching of rare earth emission can be explained by energy transfer and/or charge transfer from photo excited bdc anion to graphene. Such excited state interactions perturb the photo excited energy transfer from bdc anion to lanthanide ion. Scheme 1 shows the schematic mechanism of energy/charge transfer responsible for quenching of lanthanide emission.

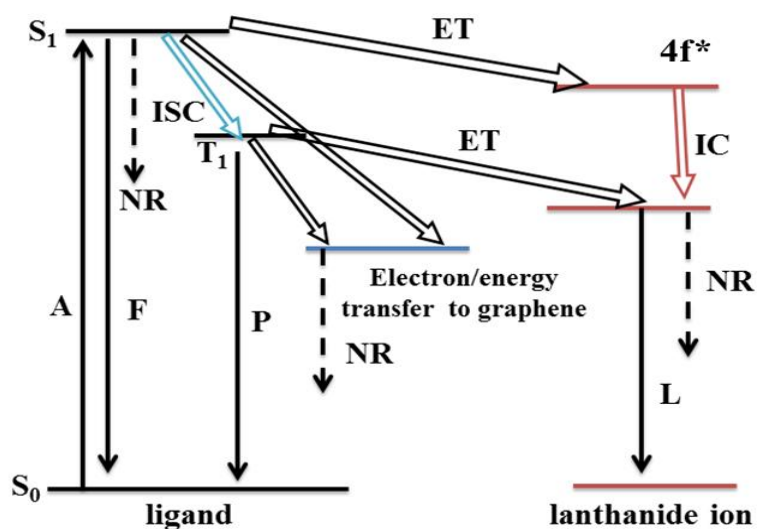
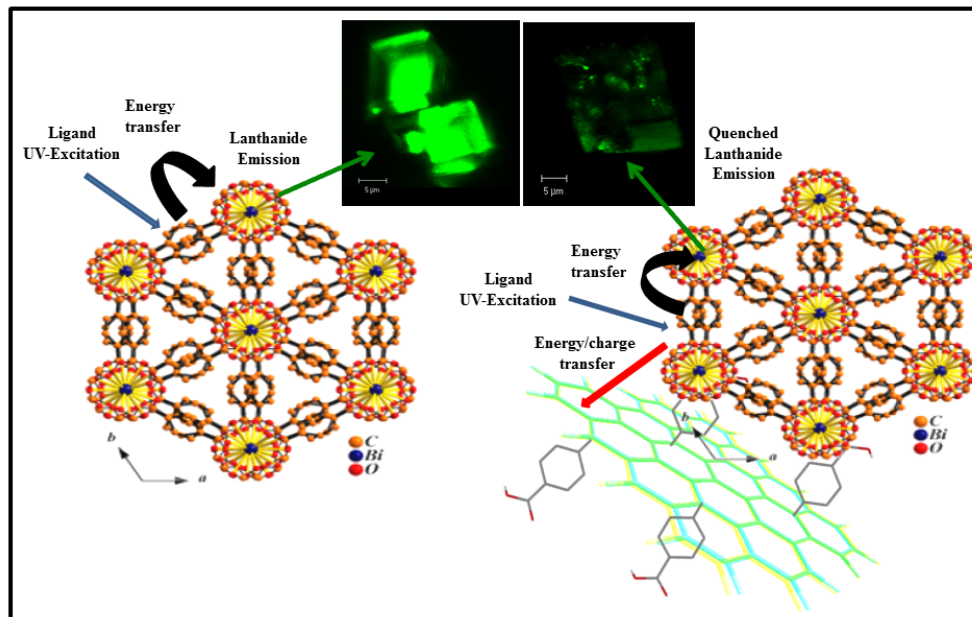


**Figure 2.11** Energy level diagram of lanthanide doped BDC- graphene composite. Graphene provides an additional non-radiative decay pathway via electron/energy transfer. ET = energy transfer, ISC = Inter system crossing, IC = internal conversion, F = fluorescence, P = phosphorescence, L = lanthanide emission, NR = non-radiative decay.



**Scheme 1:** Schematic representation of mechanism for quenching of lanthanide emission in BDC graphene composites. Inset shows confocal images of Tb-BDC and Tb-BDC3G crystals on UV light excitation.

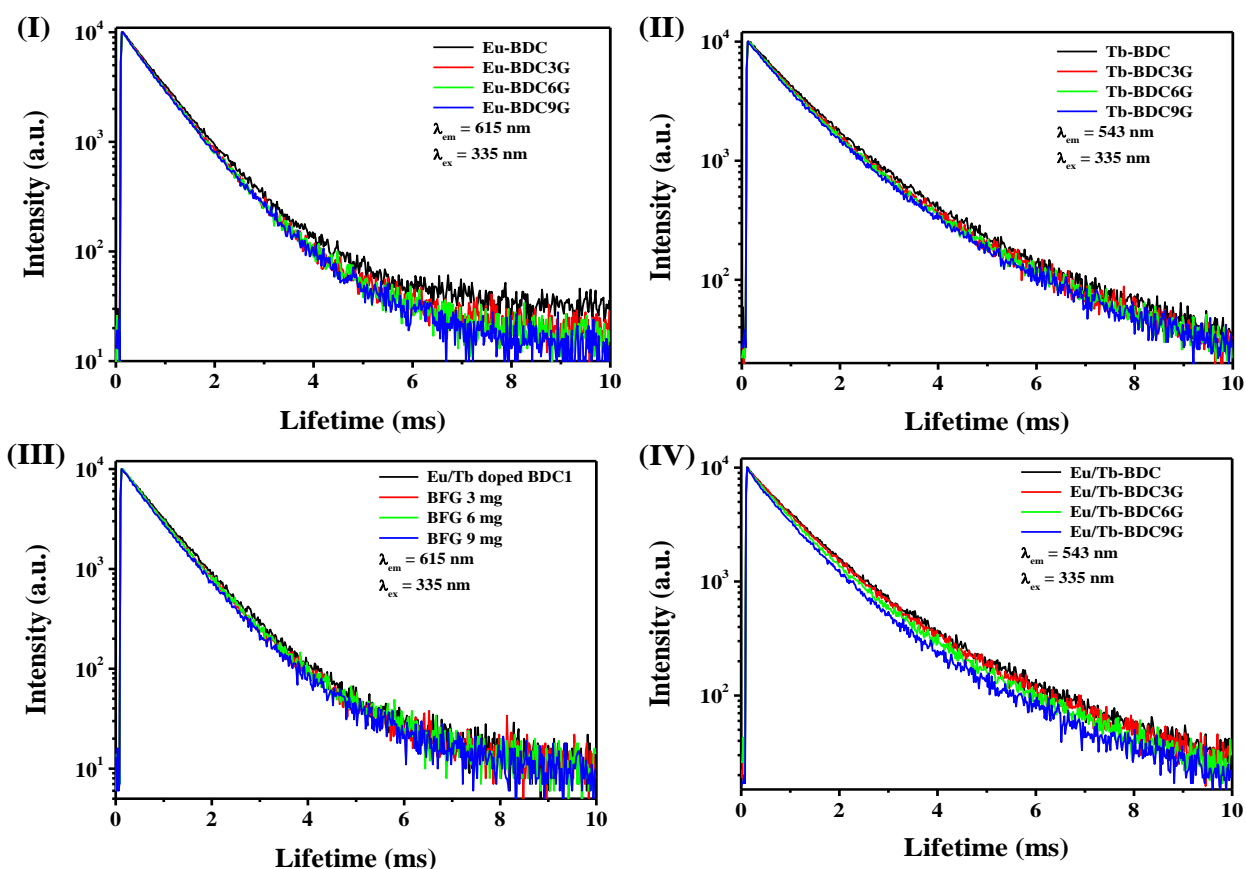


**Figure 2.12** Decay curve of lanthanide doped BDC and BDCG. (I) Eu doped BDC and BDCG (II) Tb doped BDC and BDCG (III, IV) Eu/Tb doped BDC monitored at 615 nm Eu emission and 543 nm Tb emission respectively. Excitation wavelength is 335 nm in all samples. Black, red, green and blue corresponds to BDC, BDC3G, BDC6G and BDC9G composites respectively.

Figure 2.12 shows the quantum yield of lanthanide (Eu, Tb) doped BDC and BDCG. Lanthanide doped BDC has very high quantum yield of 50.23 %, 33.64% and 40.94 % for Tb-BDC, Eu-BDC and Eu/Tb-BDC respectively. On addition of first 3mg of BFG large decrease in quantum yield was observed. The quantum yield value decreased to 1.37 %, 1.1 %, and 1.37 % for Tb-BDC3G, Eu-BDC3G and Eu/Tb-BDC3G respectively. On further addition of 6mg and 9mg BFG slight decrease in quantum yield was observed for lanthanide doped BDCG. Quantum yield value of lanthanide doped

BDC and BDCG are given in table 2. Quantum yield data further confirms very high efficiency of graphene in quenching rare earth emission.

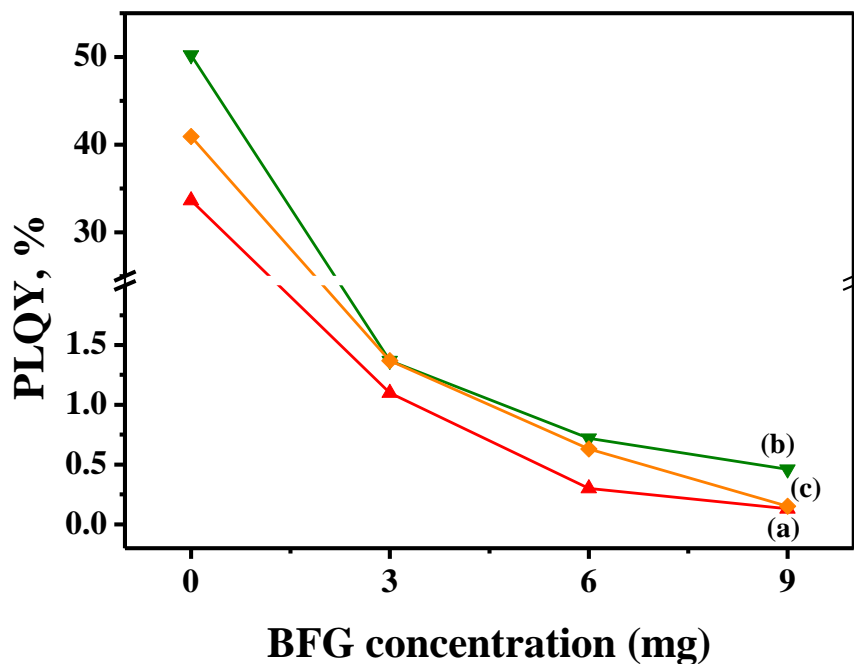


**Figure 2.13** Quantum yield with increasing functionalized graphene concentration (a) Eu doped BDC (b) Tb doped BDC and (c) Eu/Tb codoped BDC samples.

| BFG Concentration (mg) | Eu doped | Tb doped | Eu/Tb doped |
|------------------------|----------|----------|-------------|
| 0                      | 33.64    | 50.23    | 40.94       |
| 3                      | 1.1      | 1.37     | 1.37        |
| 6                      | 0.3      | 0.72     | 0.63        |
| 9                      | 0.13     | 0.46     | 0.15        |

**Table 2** Quantum yield of lanthanide doped BDC and BDC graphene composites with increasing graphene concentration. Large decrease in quantum yield was observed with first 3mg of functionalized graphene.

## **2.4 Conclusions:**

Homogeneous graphene-MOF composites of  $[\text{Bi}(1,4\text{-bdc})_2]\cdot(\text{dma})$  (**BDC**) doped with Eu and Tb with varying proportions of benzoic acid functionalized graphene (BDCG) were synthesized using a solvothermal route. Very strong quenching of lanthanide emission was observed even for very small concentration of the functionalized graphene. Lifetime measurements of lanthanide doped BDC and BDCG showed decrease in lifetime with increasing concentration of functionalized graphene consistent with the observed quenching of lanthanide emission. Lanthanide doped BDC exhibit high quantum yields due to efficient energy transfer from the photo-excited bdc anion to the lanthanide ion. Even a small concentration of functionalized graphene decreased the quantum yield of lanthanide doped BDCG drastically. Photoluminescence, lifetime and quantum yield measurements establish that graphene is highly efficient in quenching lanthanide emission. Utilization of  $\text{Bi}^{3+}$  based frameworks in designing high quantum efficiency phosphors needs to be explored in detail. The present results on quenching of lanthanide emission will have applications in designing hybrid graphene and lanthanide based composites for various optical and optoelectronic applications.

## **References:**

- [1] C. N. R. Rao, A. K. Sood, K. S. Subrahmanyam, A. Govindaraj, *Angewandte Chemie International Edition* 2009, 48, 7752-7777.
- [2] K. E. Prasad, B. Das, U. Maitra, U. Ramamurty, C. N. R. Rao, *Proceedings of the National Academy of Sciences* 2009, 106, 13186-13189.
- [3] G. Eda, M. Chhowalla, *Advanced Materials* 2010, 22, 2392-2415.



- [4] C.-H. Lu, H.-H. Yang, C.-L. Zhu, X. Chen, G.-N. Chen, *Angewandte Chemie International Edition* 2009, *48*, 4785-4787.
- [5] E. Treossi, M. Melucci, A. Liscio, M. Gazzano, P. Samori, V. Palermo, *Journal of the American Chemical Society* 2009, *131*, 15576-15577.
- [6] J. Kim, L. J. Cote, F. Kim, J. Huang, *Journal of the American Chemical Society* 2009, *132*, 260-267.
- [7] G. Williams, P. V. Kamat, *Langmuir* 2009, *25*, 13869-13873.
- [8] H. S. S. Ramakrishna Matte, K. S. Subrahmanyam, K. Venkata Rao, S. J. George, C. N. R. Rao, *Chemical Physics Letters* 2011, *506*, 260-264.
- [9] Y. Cui, Y. Yue, G. Qian, B. Chen, *Chemical Reviews* 2011, *112*, 1126-1162.
- [10] B. V. Harbuzaru, A. Corma, F. Rey, P. Atienzar, J. L. Jordá, H. García, D. Ananias, L. D. Carlos, J. Rocha, *Angewandte Chemie International Edition* 2008, *47*, 1080-1083.
- [11] A. K. Cheetham, C. N. R. Rao, *Science* 2007, *318*, 58-59.
- [12] J. W. Han, C. L. Hill, *Journal of the American Chemical Society* 2007, *129*, 15094-15095.
- [13] A. Thirumurugan, S. K. Pati, M. A. Green, S. Natarajan, *Journal of Materials Chemistry* 2003, *13*, 2937-2941.
- [14] A. Thirumurugan, J.-C. Tan, A. K. Cheetham, *Crystal Growth & Design* 2009, *10*, 1736-1741.
- [15] A. Thirumurugan, A. K. Cheetham, *European Journal of Inorganic Chemistry* 2010, *2010*, 3823-3828.
- [16] H. Chang, H. Wu, *Advanced Functional Materials* 2012, n/a-n/a.
- [17] X. Wan, Y. Huang, Y. Chen, *Accounts of Chemical Research* 2012, *45*, 598-607.
- [18] M. Jahan, Q. Bao, J.-X. Yang, K. P. Loh, *Journal of the American Chemical Society* 2010, *132*, 14487-14495.
- [19] M. S. Dresselhaus, A. Jorio, R. Saito, *Annual Review of Condensed Matter Physics* 2010, *1*, 89-108.
- [20] S. Bordiga, C. Lamberti, G. Ricchiardi, L. Regli, F. Bonino, A. Damin, K. P. Lillerud, M. Bjorgen, A. Zecchina, *Chemical Communications* 2004, *0*, 2300-2301.
- [21] F. S. Richardson, *Chemical Reviews* 1982, *82*, 541-552.
- [22] A. F. Kirby, F. S. Richardson, *The Journal of Physical Chemistry* 1983, *87*, 2544-2556.
- [23] M. G. van der Horst, G. A. van Albada, R.-M. Ion, I. Mutikainen, U. Turpeinen, S. Tanase, J. Reedijk, *European Journal of Inorganic Chemistry* 2008, *2008*, 2170-2176.
- [24] V. Biju, T. Itoh, Y. Baba, M. Ishikawa, *The Journal of Physical Chemistry B* 2006, *110*, 26068-26074.
- [25] J. Cao, J. Z. Sun, J. Hong, H. Y. Li, H. Z. Chen, M. Wang, *Advanced Materials* 2004, *16*, 84-87.
- [26] A. Ghosh, K. V. Rao, S. J. George, C. N. R. Rao, *Chemistry – A European Journal* 2010, *16*, 2700-2704.
- [27] A. Kasry, A. A. Ardakani, G. S. Tulevski, B. Menges, M. Copel, L. Vyklicky, *The Journal of Physical Chemistry C* 2012, *116*, 2858-2862.
- [28] Z. Chen, S. Berciaud, C. Nuckolls, T. F. Heinz, L. E. Brus, *ACS Nano* 2010, *4*, 2964-2968.

***Hybrid nanocomposites of ZIF-8 with graphene oxide exhibiting tunable morphology, significant CO<sub>2</sub> uptake and other novel properties***

---

***Summary***\*

Hybrid nanocomposites of graphene oxide (GO) with ZIF-8 were synthesized and effect of graphene oxide on the morphology and gas adsorption property was studied. Graphene oxide provides as the coordination center for Zn(II) metal ions and controls the nucleation and growth of ZIF-8 nanocrystals. With increase in GO wt.% due to the presence of epoxide, hydroxyl and carboxylic acid functional groups on basal plane the particle size of ZIF-8 decreases from 80-100 nm to 5-10 nm. The morphology of crystals changes from hexagonal to spherical. The surface area of the hybrid nanocomposites depends on the graphene content. The nanocomposites show high CO<sub>2</sub> uptake up to 72 wt.% at 195 K and 1 atm. The remarkably high CO<sub>2</sub> uptake of these nanocomposites can be attributed to synergistic effect due to graphene oxide.

---

\*A paper based on this study has been accepted for publication in *Chem. Commun.*

### **3.1 Introduction:**

Metal-organic frameworks (MOFs) or porous coordination polymers (PCPs) have attracted great attention in recent years because of their possible use in gas storage, catalysis, and optoelectronic devices.<sup>[1-5]</sup> The modifiable pore surface of MOFs propels them to forefront of clean energy and drug delivery research.<sup>[6, 7]</sup> Scaling down these materials to nanoscale keeping the same periodic structure of the bulk state can give rise to novel applications in bio imaging, bio-sensing and other areas.<sup>[8-10]</sup> Furthermore nanoscale MOFs enables solution-based processibility and increased gas uptake.<sup>[11, 12]</sup> Methodologies such as solvent induced precipitation, solvo(hydro)thermal or microwave treatment, coordination modulation techniques and reverse micro emulsion have been employed for the synthesis of nanoscale MOFs.<sup>[8-12]</sup> In the last few years, graphene oxide (GO) has become a material of vital importance because of its unique properties.<sup>[13, 14]</sup> GO has a functionalized basal plane with anchoring groups like hydroxyl, epoxy or carboxyl which are useful for forming graphene-based soft materials and hybrid composites.<sup>[15, 16]</sup> Hybrid composites based on MOFs and graphene afford integration of the unique properties of these two fascinating materials, thus allowing one to design materials possessing properties not possessed by either component.<sup>[17-19]</sup> Bando *et al.* have recently reported GO–MOF composites for the adsorption of ammonia and nitric oxide<sup>[20]</sup> while Loh *et al.* have described conducting nanowires comprising MOF-5 and benzoic acid functionalized graphene where MOF-5 is intercalated between graphene sheets.<sup>[21]</sup> Growth of MOF nanocrystals of different morphologies on graphene sheets has not been explored adequately.

GO can be considered to be a potential platform and as a structure-directing agent for the growth and stabilization of MOF nanoparticles, where coordination modulation occurs through the different functional groups on the surface.<sup>[15]</sup> In this context, making use of zeolitic imidazolate frameworks (ZIFs), a new class of zeolite-like MOFs, possessing a high degree of microporosity and exceptional thermal and chemical stabilities to prepare composites with GO appeared attractive. The prototypical ZIF-8 ( $\text{Zn}(\text{MeIM})_2$ , MeIM = 2-methylimidazolate) with a sodalite zeolite structure, containing large cavities ( $\sim 11.7$  Å of diameter) interconnected by narrow windows ( $\sim 3.40$  Å) was used for the purpose (scheme 1a).<sup>[22-25]</sup> It may be noted that ZIF-8 has been exploited for developing thin films, membranes for catalysis and separation of gases.<sup>[26, 27]</sup> A simple route for the preparation of hybrid nanocomposites of graphene oxide and ZIF-8, where the growth of the ZIF-8 nanocrystals as well as their sizes and morphologies are tuned by the different concentration of GO was developed. The obtained GO@ZIF-8 (ZG) hybrid nanocomposites show tunable surface areas and pore volumes depending on the proportion of GO. Interestingly the hybrid nanocomposites exhibit characteristics by nature of both GO and ZIF-8. The composites exhibit remarkable  $\text{CO}_2$  uptake characteristics with increasing GO concentration. Furthermore, we demonstrate the generation of ZnS nanoparticles on the GO sheets by using external sulphur source, where GO acts as a template and ZIF-8 as the sacrificial Zn source.

### **3.2 Materials and experiments:**

**Materials:** All the reagents and solvents were commercially available and used as supplied without further purification.  $\text{Zn}(\text{NO}_3)_2 \cdot 6\text{H}_2\text{O}$ , 2-methylimidazole were obtained from Aldrich Chemical Co.

#### **Synthesis of Graphite Oxide:**

Detailed synthesis procedure for graphite oxide using modified Hummers method is given in Chapter 2.

#### **Room temperature synthesis of nanoscale ZIF-8 crystals:**

Nanoscale ZIF-8 with hexagonal morphology was prepared according to the literature procedure reported by Wiebcke *et al.*<sup>1</sup> In a typical synthesis methanolic solution (25 ml)  $\text{Zn}(\text{NO}_3)_2 \cdot 6\text{H}_2\text{O}$  (16 mmol, 366 mg) was slowly added into a methanolic solution (25 ml) of 2-methylimidazole (8 mmol, 811 mg) with constant stirring. Stirring was stopped after combining the component solutions and a *gel*-like solid was recovered by centrifugation and washed with methanol for three times and then dried under vacuum. Yield: 60%. Anal. Calcd. for  $\text{C}_8\text{H}_{10}\text{N}_4\text{Zn}$ : C, 42.18; H, 4.3; N, 24.6; Found: C, 41.54; H, 4.86; N, 24.39 %.

#### **Preparation of GO@ZIF-8 hybrid nanocomposites:**

First bare X mg of GO was dispersed in methanol and sonicated for 5 hours. For the synthesis of GO@ZIF-8 composites, different wt.% of GO solution added during preparation of ZIF-8 nano crystals in the stirring condition. The resultant solution was centrifuged and washed several times with water-methanol mixture and dried at 60 °C.

The resulting solid composites obtained by variation of GO content were denoted by ZG-X, X indicated wt.% (X = 1, 2, 4, 10 and 20 wt.%) of GO in comparison to Zn(II) metal. The obtained samples were designated as ZG (**ZG-0**, **ZG-1**, **ZG-2**, **ZG-4**, **ZG-10** and **ZG-20**) based on the different amount of GO loading.

### **Characterization:**

The as synthesized ZIF-8, GO@ZIF-8 composites and Go@ZnS were characterized through different techniques. Powder X-ray diffraction (PXRD) pattern were recorded on a Bruker D8 Discover instrument using Cu-K $\alpha$  radiation. The morphology and porous nature of ZG-Xs' were characterized with Transmission electron microscopy (TEM) (JEOL JEM-3010 with an accelerating voltage at 300 KV). The Raman spectra of the samples were recorded in backscattering arrangement, using 532 nm laser excitation and 6 mW laser power. Thermogravimetric analysis (TGA) were carried out under nitrogen (flow rate of 50 mL/min) with Metler Toledo TGA-850 TG analyzer in the temperature range between 25 - 800°C at a heating rate 3°C / min.

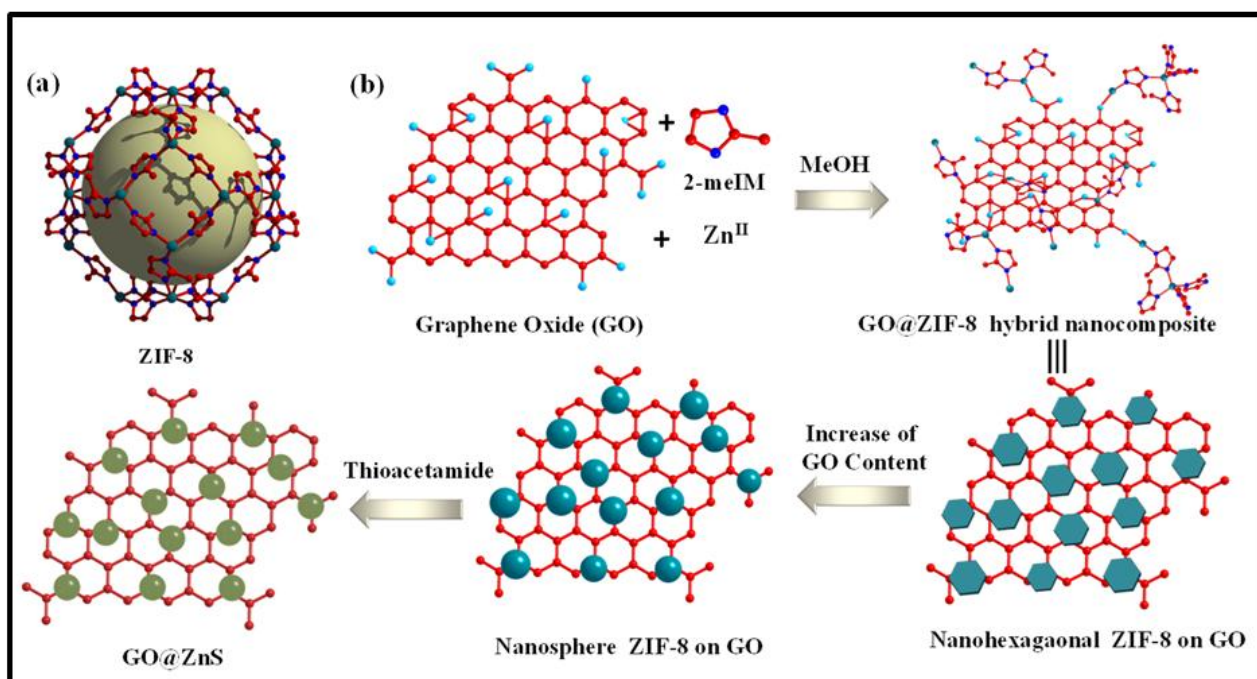
### **Adsorption Measurements:**

Adsorption studies of N<sub>2</sub> (77 K) and CO<sub>2</sub> (195 K) on ZIF-8 and ZG composites were carried out using *QUANTACHROME AUTOSORB-1C* analyzer. Prior to the measurements, the samples were activated at 433 K under high vacuum. In the sample chamber (~12 mL) maintained at  $T \pm 0.03$  K was placed the adsorbent sample (100-150 mg), which had been prepared at 423 K in 10<sup>-1</sup> Pa for 18 hours prior to measurement of the isotherms. The adsorbate was charged into the sample tube, and then the change of the pressure was monitored and the degree of adsorption was determined by the decrease

of the pressure on the equilibrium state. All operations were computer-controlled and automatic.

### 3.3 Results and Discussion:

In Scheme 1 we show the method of synthesis of GO@ZIF-8 hybrid nanocomposites with different GO content (ZG-0, ZG-1, ZG-2, ZG-4, ZG-10 and ZG-20 corresponding 0, 1, 2, 4, 10 and 20 wt% GO, respectively).



**Scheme 1.** (a) View of ZIF-8 framework showing large cavities with narrow windows; (b) Stepwise synthesis of GO@ZIF-8 hybrid nanocomposites with tunable morphology, nanospheres from hexagonal ZIF-8 nanocrystals and *in-situ* stabilization of ZnS nanoparticles on the GO sheet

The phase purity of the nanocomposite was established through elemental analysis and EDAX (Figure 3.2, 3.3). Powder X-ray diffraction patterns of the composites with different GO contents show the reflections of ZIF-8 (cubic space group) (Figure 3.1). With increase of GO content, a new reflection appears at  $2\theta = 8.6^\circ$  close to the 110 peak of ZIF-8, which would be attributed to GO. Such low angle shift compared to pristine GO indicating intercalation of ZIF-8 nanocrystals between the GO sheets.

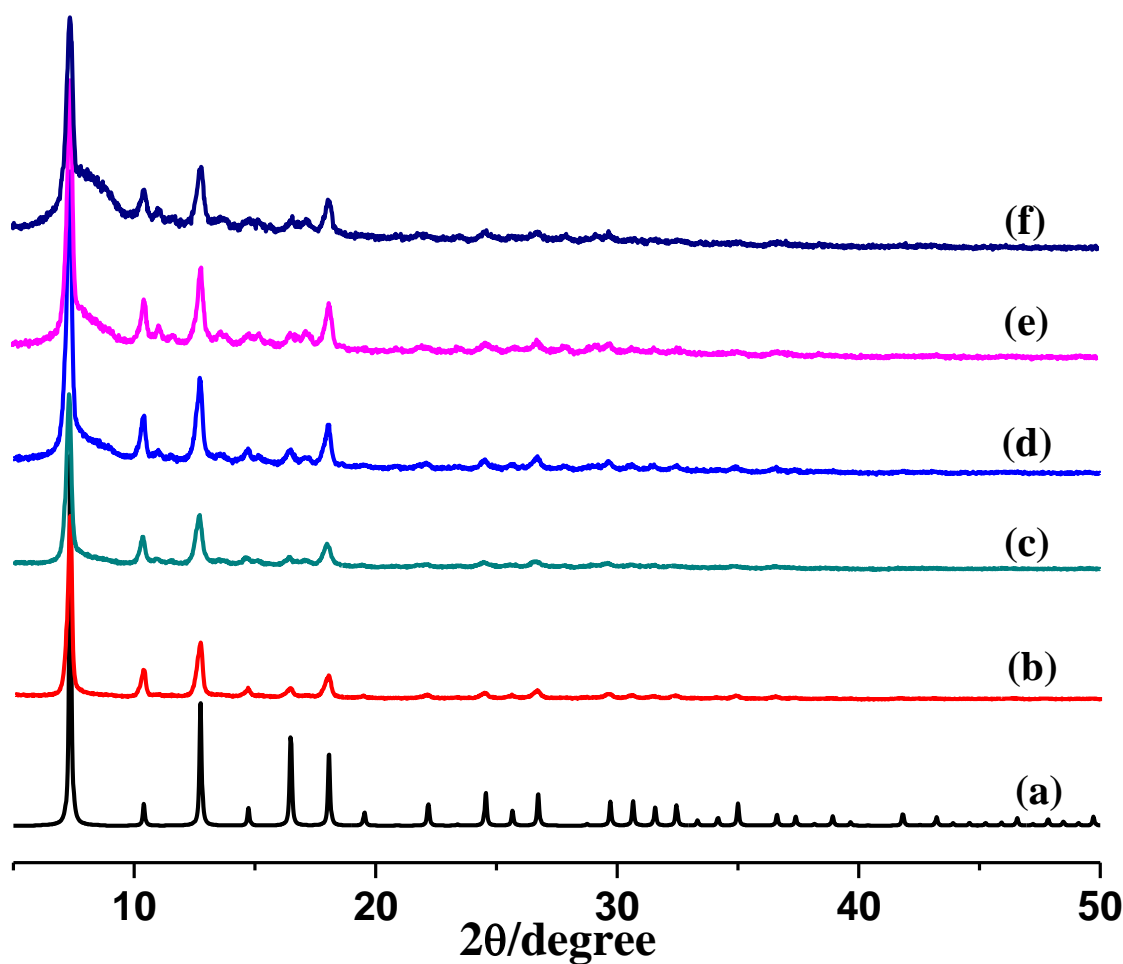


**Figure 3.1:** PXRD patterns of ZIF-8 and GO@ZIF-8 hybrid nanocomposites; (a) ZG-0 (ZIF-8), (b) ZG-1, (c) ZG-2, (d) ZG-4, (e) ZG-10, and (f) ZG-20



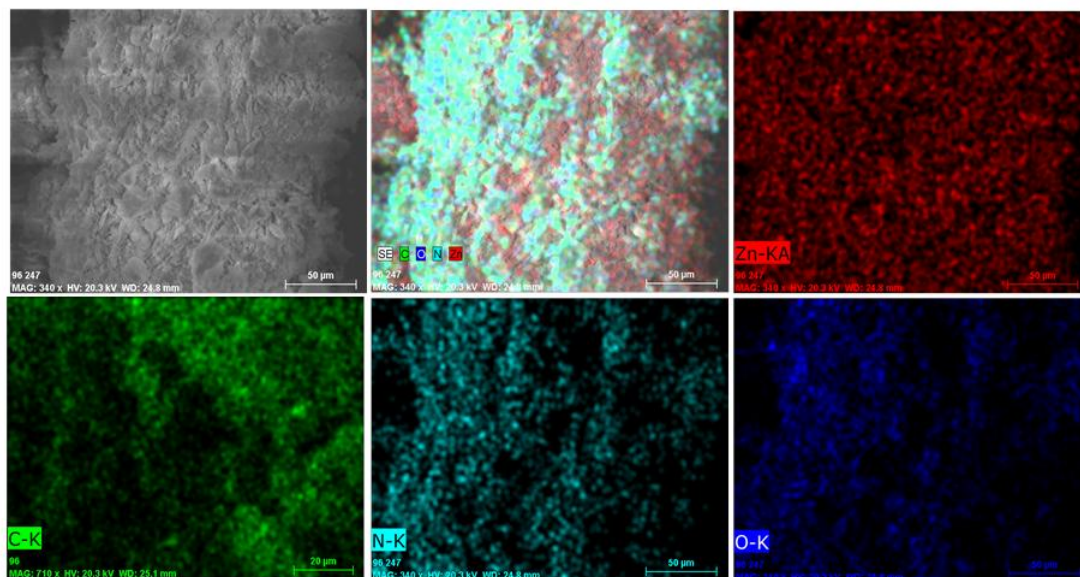


**Figure 3.2** Colour mapping of **ZG-10** sample showing phase purity with homogeneously distributed throughout the sample.

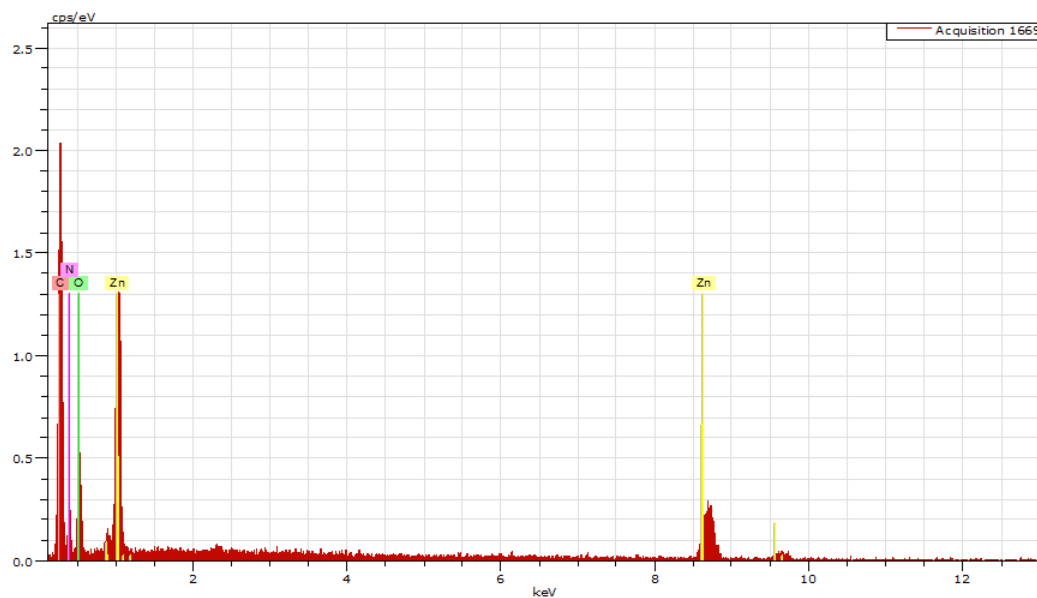


**Figure 3.3** Energy dispersive X-ray spectroscopy (EDS) analysis of **ZG-10** sample showing presence of C, N, O and Zn elements.

The infrared spectra of the ZG hybrid nanocomposites show bands due to ZIF-8 as

well as GO, the frequencies being shifted to slightly lower frequencies (Figure 3.4).

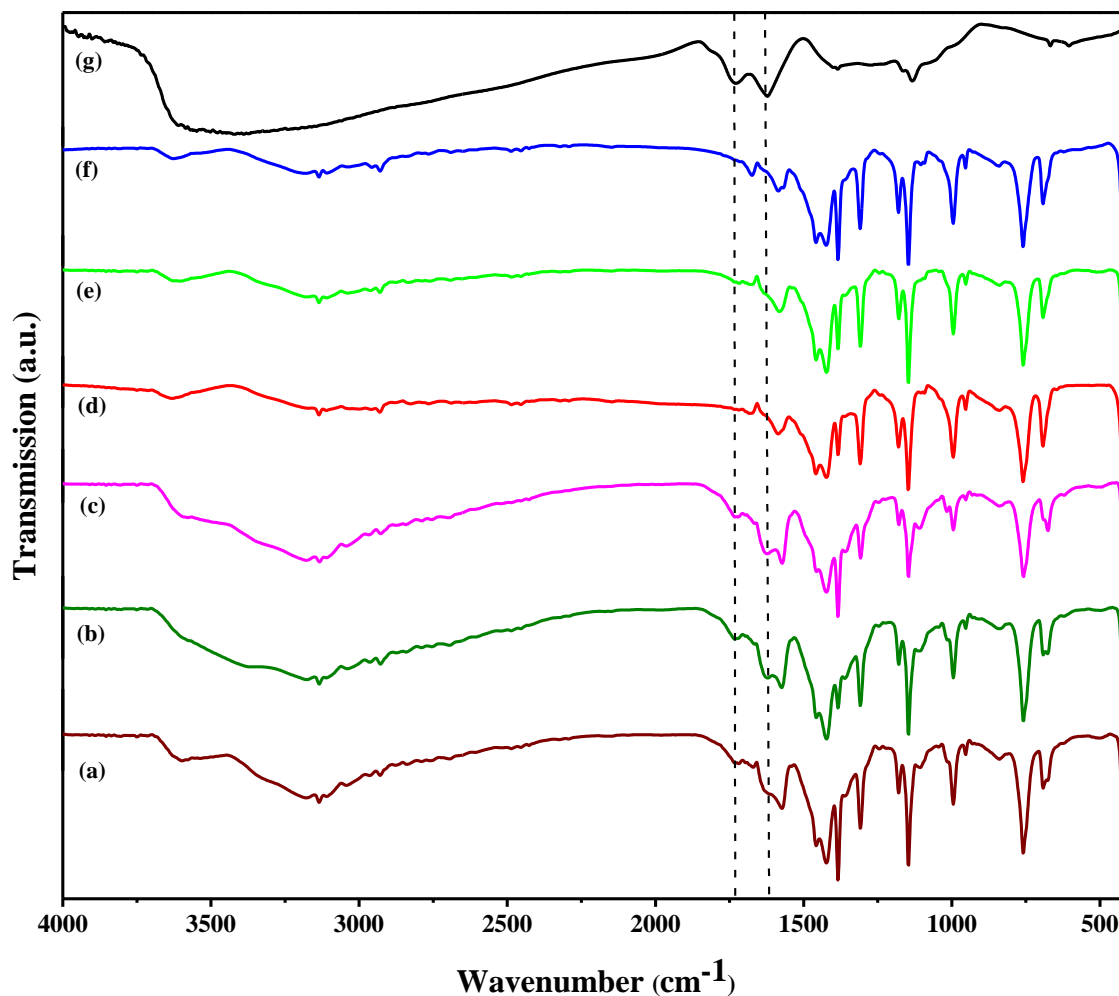


**Figure 3.4** FT-IR spectra of (a) ZG-0 (ZIF-8), (b) ZG-1, (c) ZG-2, (d) ZG-4, (e) ZG-10, (f) ZG- 20 and (g) GO.

Infrared spectrum of graphite oxide (GO) shows peak at  $1728\text{ cm}^{-1}$  due to C=O stretching vibration, peak at  $1621\text{ cm}^{-1}$  can be attributed to C=C vibration of unoxidized  $\text{sp}^2$  domains along with contribution from adsorbed water molecules. Fingerprint region is very broad with many overlapping peaks which cannot be clearly resolved. Peak around  $1230\text{ cm}^{-1}$  can be due to C-O stretching vibration of hydroxyl and epoxide functional

group. In ZG composites additional bands around  $1728\text{ cm}^{-1}$  and  $1621\text{ cm}^{-1}$  are observed due to contribution from GO. The  $1586\text{ cm}^{-1}$  band of ZIF-8 has shifted in ZG composites to lower wavenumber with increasing wt.% of GO. The value for ZG-4, 10, 20 is around  $1574\text{ cm}^{-1}$  which indicates a strong interaction between graphene oxide and ZIF-8 nanoparticles. The  $1586\text{ cm}^{-1}$  band of ZIF-8 can be attributed stretching vibration of imidazole ring.

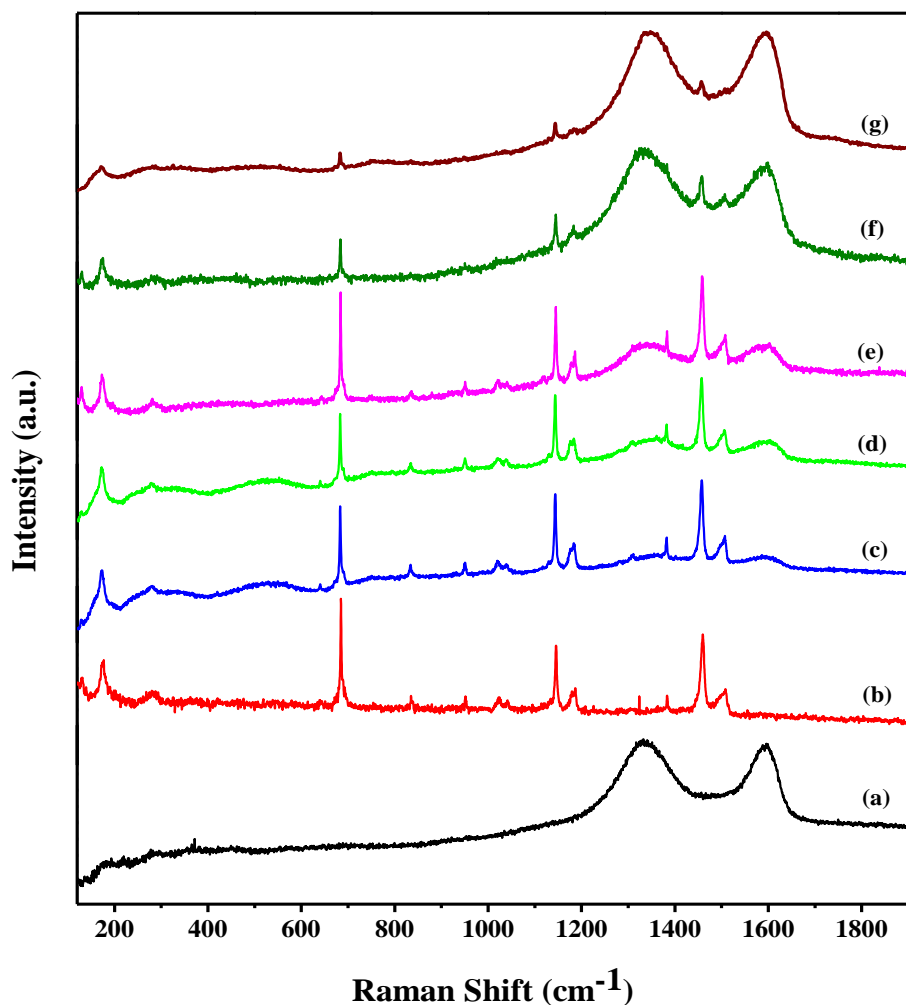


**Figure 3.5** Raman spectra of (a) ZG-0 (ZIF-8), (b) ZG-1, (c) ZG-2, (d) ZG-4, (e) ZG-10, (f) ZG-20 and (g) GO.

The ZIF-8 shows bands in the Raman spectrum corresponding to the 2-methylimidazole linker while GO shows bands at  $1333\text{ cm}^{-1}$  and  $1594\text{ cm}^{-1}$  due to the D and G bands respectively. The Raman spectra of composites show bands corresponding to ZIF-8 as well as the D and G bands (Figure 3.5). Peak assignment of Raman spectra is given in table 3.1 below.

| Raman Shift ( $\text{cm}^{-1}$ ) | Assignment   |
|----------------------------------|--|
| 685 (s)                          | $\nu$ ( $\text{CCH}_3$ ) due to C-C stretching of methyl group attached to imidazole ring.                         |
| 1145 (s)                         | Methyl rocking vibration $\rho$ ( $\text{CH}_3$ ). Bending mode of $\text{CH}_3$ group attached to imidazole ring. |
| 1460 (s)                         | Antisymmetric deformation vibrations of C-H in methyl group  |
| 1380 (w)                         | Symmetric deformation vibrations of C-H in methyl group  |
| 834 (w)                          | $\gamma$ (CH) modes. Out of plane C-H bending mode of H attached to 2-methylimidazole ring.                        |
| 1508 (m)                         | $\nu$ (R) In-plane imidazole ring stretching mode.   |
| 2930 (m)                         | C-H stretching vibration of methyl group ( $\text{sp}^3$ C-H stretching vibration).                                |
| 3114,3135 (m)                    | C-H stretching vibration of H attached to 2-methylimidazole ring ( $\text{sp}^2$ C-H stretching vibration)         |
| 1333 (broad)                     | D band of graphite oxide.  |
| 1594 (broad)                     | G band of graphite oxide.  |

[w = weak, s = strong, m = medium intensity]

**Table 3.1.** Raman peak assignment of ZIF-8 (ZG-O) and ZIF-8 graphene oxide composites (ZG).

Thermogravimetric (TG) analysis of ZIF-8 and the composites show high thermal stability as shown in figure 3.6.

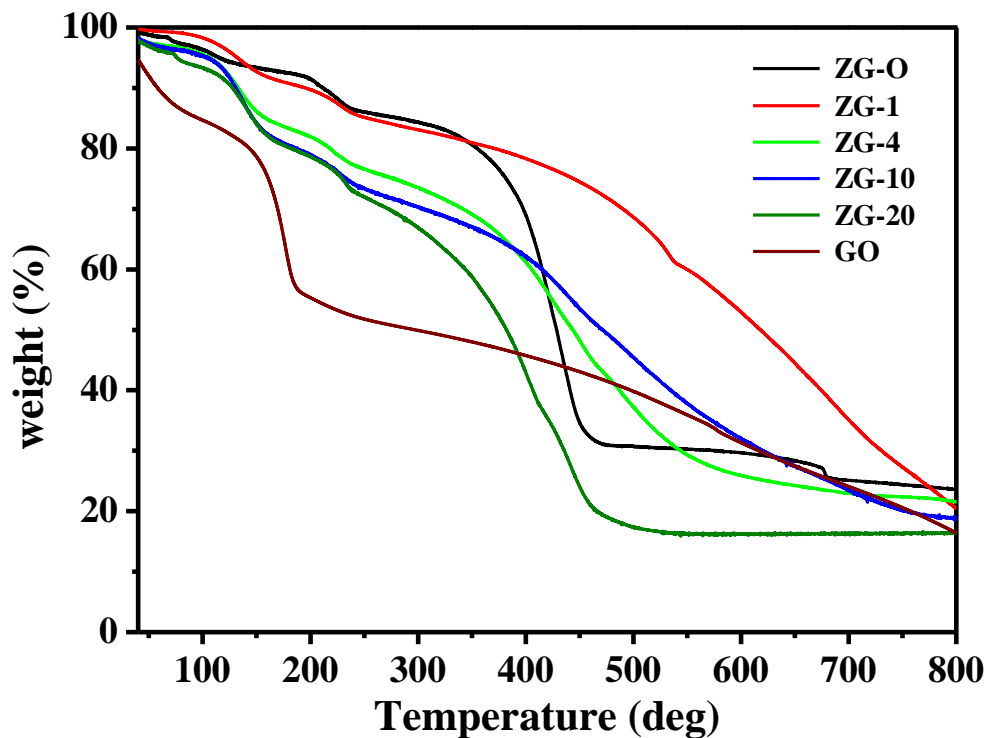
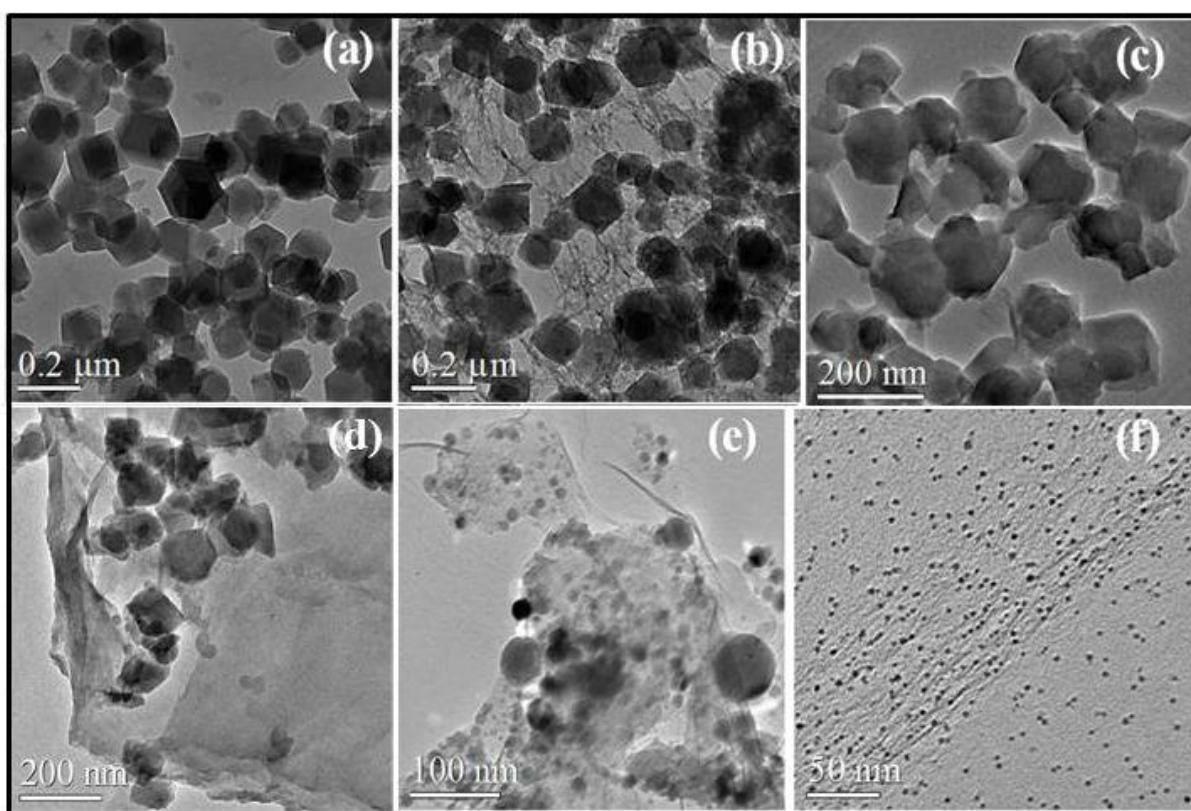


Figure 3.6 TGA of as-synthesized ZIF-8, GO and ZG composites.

The morphologies of ZIF-8 and the ZG composites were characterized by transmission electron microscopy (TEM). Typical TEM images are shown in Figure 3.7. The as-synthesized ZIF-8 (without any GO) shows hexagonal morphology with a particle size in the range ~100 - 150 nm as shown in Fig. 2a. Similar hexagonal morphology and particle size are also found in ZG-1 (1 wt.% of GO), with the ZIF-8 particles being stabilized within the dense GO sheets. With increasing GO content, the particle size of ZIF-8 decreases. In the case of ZG-2, irregular hexagons with a few squares or rectangles of 50 -100 nm size are seen and covered between the GO sheets (Figure 3.7c). On

increasing the GO content to 4 wt.% in (ZG-4), irregular particles transform to spherical shape, the size being 40 - 50 nm (Figure 3.7d). In ZG-10 (10 wt.% GO) spheres of 20 nm diameter (with a few of the bigger size of 40-50 nm) are formed (Figure 3.7e). In the case of ZG-20 (20 wt.% GO), the size of the nanocrystals gets significantly reduced and we see a homogenous distribution of uniform nanospheres of ~4 nm diameter in figure 3.7f.



**Figure 3.7** TEM images of ZG samples (a) ZG-0, (b) ZG-1, (c) ZG-2, (d) ZG-4, (e) ZG-10 and (f) ZG-20.

Clearly, the size and morphology of ZIF-8 are controlled by the percentage of GO in the composite. The GO sheets appear to provide a platform for the nucleation and growth of

nanocrystals. The shapes and sizes (hexagonal to sphere) are probably controlled by -OH and -COOH groups through coordination modulation which inhibits the growth of large crystals. The functionalized GO sheets act as both structure-directing and size-controlling agents for ZIF-8 nanocrystals.

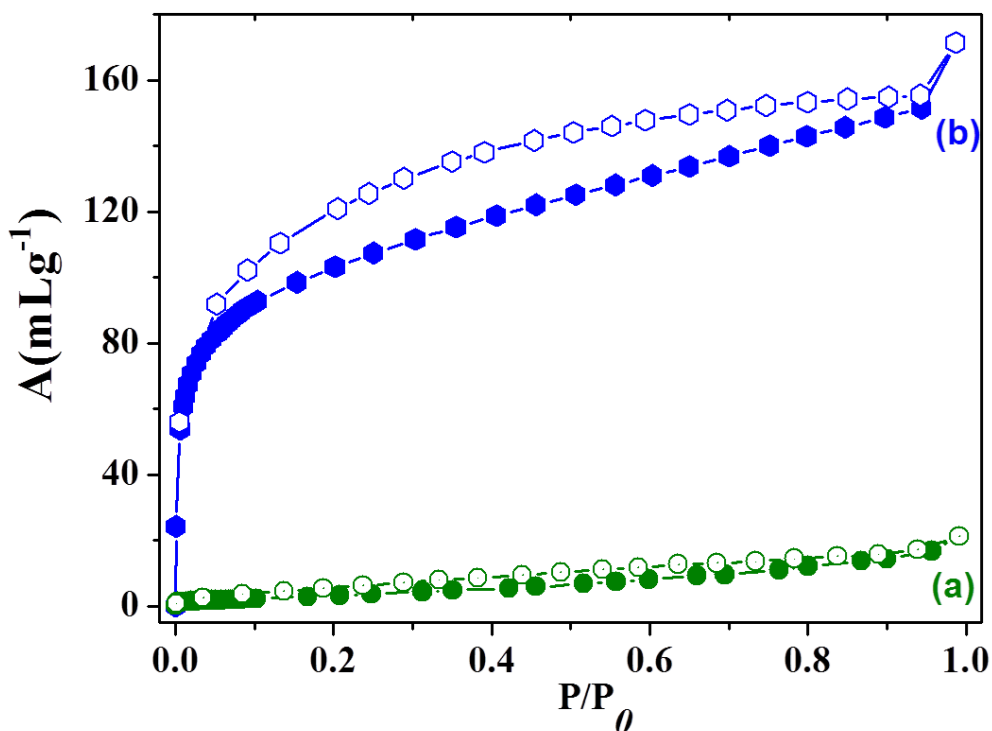


**Figure 3.8** (a) Nitrogen (b) Carbon dioxide adsorption isotherm of GO at 77 and 195 K respectively.

Textural parameters such as surface area, pore volume and pore size of the ZG hybrid nanocomposites were obtained from  $\text{N}_2$  adsorption-desorption measurements at 77 K (Figure 3.9, left). The BET surface area of the GO sample is around  $\sim 15 \text{ m}^2/\text{g}$  (Figure 3.8). On the other hand,  $\text{N}_2$  adsorption of the nanoscale ZIF-8 (ZG-0) shows typical type -I profile with a surface area of about  $1120 \text{ m}^2/\text{g}$  comparable with the literature value. The textural parameters of the ZG composites are given in table 3.2. The BET surface

area of the composites decreases relative to ZG-0 (ZIF-8) with increasing GO content. Thus, the surface areas of ZG-1, ZG-2, ZG-4, ZG-10 and ZG-20 are 819, 675, 450, 320, 280  $\text{m}^2/\text{g}$  respectively. The decrease in surface area can arise due to an increasing proportion of nonporous GO in the composites. To our surprise, the ZG composites exhibit good  $\text{CO}_2$  storage capacity with the  $\text{CO}_2$  uptake at 195 K increasing with the increasing GO content (Figure 3.9 (right) and Table S2). Note that pristine ZIF-8 (ZG-0) and GO show 27.2 wt.% and 33 wt.% of  $\text{CO}_2$  uptake, respectively (Figure 3.8). ZG-4 exhibits  $\text{CO}_2$  uptake of about 49 wt.% at 195 K (1 atm) which increases further to 72 wt.% in ZG-20. This unusual  $\text{CO}_2$  uptake can be attributed cumulative effect of ZIF8 and GO as later provide specific interaction with  $\text{CO}_2$  based functionalities on the sheets. This is supported by the high heat of  $\text{CO}_2$  sorption ( $q_{\text{st},\phi}$ ) 31.9 kJ/mol in case of ZG-20 obtained from Dubinin-Radushkevich (DR) equation.<sup>[28]</sup> To the best of our knowledge, this is the first report of GO@ZIF-8 hybrid nanocomposites with tunable porosity and significant  $\text{CO}_2$  storage capacity.

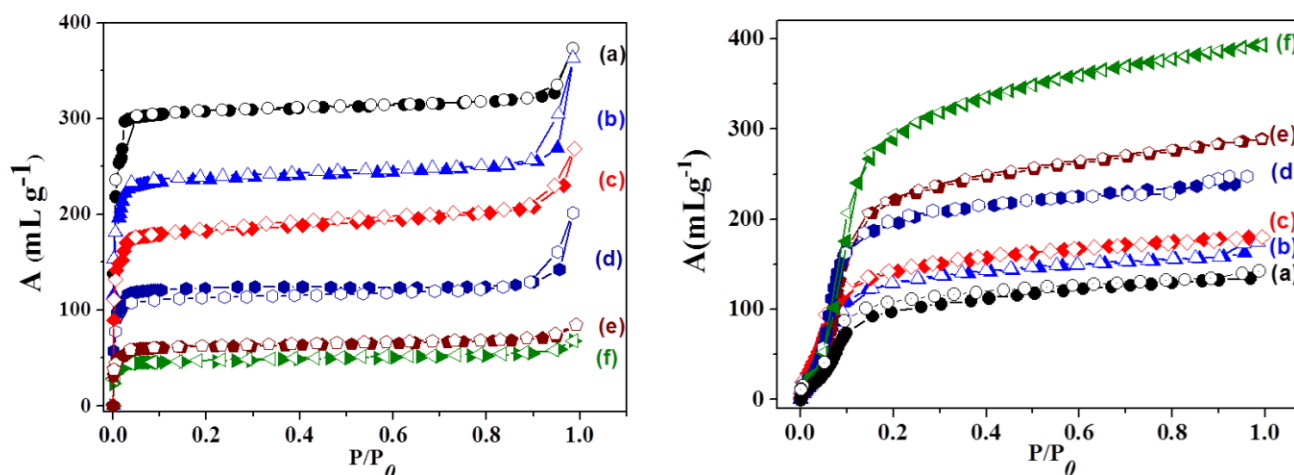


**Figure 3.9** (Left) Nitrogen (at 77 K), (right) Carbon dioxide (at 195 K) adsorption-desorption isotherms of ZG samples (a) ZG-0; (b) ZG-1; (c) ZG-2; (d) ZG-4 (e) ZG-10 (f) ZG-20.



| Sample | $S_{\text{BET}}$<br>( $\text{m}^2/\text{g}$ ) | $V_p$<br>( $\text{cm}^3/\text{g}$ ) | $\text{CO}_2$<br>(wt%) | Q<br>(KJ/mol) |
|--------|---|-------------------------------------|------------------------|---------------|
| ZIF-8  | 1120  | 0.56                                | 27.2                   | -             |
| ZG-1   | 819   | 0.45                                | 32.4                   | 28.9          |
| ZG-2   | 675   | 0.23                                | 35.1                   | 29.4          |
| ZG-4   | 450   | 0.19                                | 48.4                   | 30.3          |
| ZG-10  | 320   | 0.11                                | 55.3                   | 31.4          |
| ZG-20  | 289   | 0.09                                | 72.4                   | 31.9          |

**Table 3.2.** Textural parameters and  $\text{CO}_2$  storage capacities of as-synthesized nanocrystals of ZIF-8 and ZG composites.

Zinc sulphide (ZnS) shows fascinating electrical and optical properties, which would be further modified into nanoscale or in hybridization with other materials like graphene oxide (GO).<sup>[29]</sup> We have made use of the GO@ZIF-8 composite, ZG-20 for the synthesis of the GO@ZnS composite. On reaction with ZG-20 with thioacetamide, the ZIF-8 in the composite acts as the sacrificial Zn source and reacts with the sulphur produced by thioacetamide. Figure 3.10 (a) shows the powder X-ray diffraction pattern of the GO@ZnS nanocomposite with broad reflections corresponding to the Wurtzite structure of ZnS (*JCPDS No 39-1363*). The reflection at  $12.21^\circ$  corresponds to GO and the slight shift to a higher angle corroborates a decrease in the interlayer separation between two successive graphene sheets. Figure 3.10 (b-c) shows TEM images of the GO@ZnS, revealing that the ZnS nanoparticles of  $\sim 3$  nm are stabilized on the GO sheet. This particle size is consistent with the XRD data and this hybrid also shows uptake of  $\text{CO}_2$  about 9 wt% as shown in Figure 3.11.

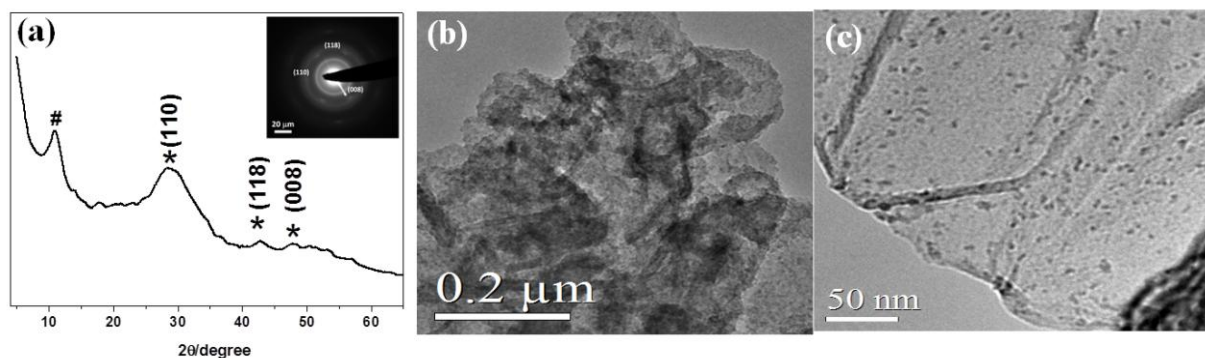


**Figure 3.10** Characterization of GO@ZnS composites: (a) powder XRD pattern (ED pattern inset shows three planes of the ZnS corresponding Wurtzite structure); (b-c) TEM images of show ZnS nanoparticles on the GO sheet.

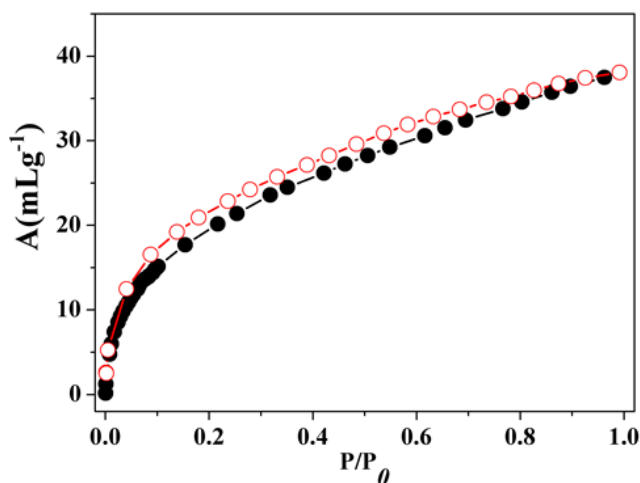


**Figure 3.11** CO<sub>2</sub> adsorption profile of GO@ZnS nano composite at 195 K.

### **3.4 Conclusions:**

In conclusion, we have demonstrated a simple procedure to prepare hybrid GO@ZIF-8 hybrid nanocomposites. ZIF-8 is stabilized on the GO surfaces through functional groups and the nanoscale morphology of the composite (from hexagonal to spherical) can be tuned by the concentration of GO. GO acts as a structure-directing

agent for the growth of nanocrystals of ZIF-8 through coordination modulation. The composites show remarkable CO<sub>2</sub> storage capacity compared to the parent ZIF-8. To the best of our knowledge, this is the first account of the growth and stabilization of nanoscale MOF on a graphene surface, with tunable morphology and gas storage characteristics. The GO-ZIF composite can be used as a precursor to obtain the GO@ZnS composite by reaction with thioacetamide, where ZIF-8 acts as the sacrificial source of Zn(II).

### **References:**

- [1] L. J. Murray, M. Dinca, J. R. Long, *Chemical Society Reviews* 2009, 38, 1294- 1314.
- [2] A. K. Cheetham, C. N. R. Rao, *Science* 2007, 318, 58-59.
- [3] S. Kitagawa, R. Kitaura, S.-i. Noro, *Angewandte Chemie International Edition* 2004, 43, 2334-2375.
- [4] J. Lee, O. K. Farha, J. Roberts, K. A. Scheidt, S. T. Nguyen, J. T. Hupp, *Chemical Society Reviews* 2009, 38, 1450-1459.
- [5] A. Dhakshinamoorthy, M. Alvaro, A. Corma, H. Garcia, *Dalton Transactions* 2011, 40, 6344-6360.
- [6] J.-R. Li, R. J. Kuppler, H.-C. Zhou, *Chemical Society Reviews* 2009, 38, 1477-1504.
- [7] P. Horcajada, T. Chalati, C. Serre, B. Gillet, C. Sebrie, T. Baati, J. F. Eubank, D. Heurtaux, P. Clayette, C. Kreuz, J.-S. Chang, Y. K. Hwang, V. Marsaud, P.-N. Bories, L. Cynober, S. Gil, G. Ferey, P. Couvreur, R. Gref, *Nat Mater* 2010, 9, 172-178.
- [8] W. Lin, W. J. Rieter, K. M. L. Taylor, *Angewandte Chemie International Edition* 2009, 48, 650-658.
- [9] A. M. Spokoyny, D. Kim, A. Sumrein, C. A. Mirkin, *Chemical Society Reviews* 2009, 38, 1218-1227.
- [10] A. Carne, C. Carbonell, I. Imaz, D. Maspoch, *Chemical Society Reviews* 2011, 40, 291-305.
- [11] H. J. Lee, W. Cho, S. Jung, M. Oh, *Advanced Materials* 2009, 21, 674-677.
- [12] T. Tsuruoka, S. Furukawa, Y. Takashima, K. Yoshida, S. Isoda, S. Kitagawa, *Angewandte Chemie International Edition* 2009, 48, 4739-4743.
- [13] C. N. R. Rao, A. K. Sood, K. S. Subrahmanyam, A. Govindaraj, *Angewandte Chemie International Edition* 2009, 48, 7752-7777.
- [14] D. Chen, H. Feng, J. Li, *Chemical Reviews* 2012, 112, 6027-6053.

- 
- [15] X. Li, W. Qi, D. Mei, M. L. Sushko, I. Aksay, J. Liu, *Advanced Materials* 2012, 24, 5136-5141.
- [16] J. Kim, L. J. Cote, J. Huang, *Accounts of Chemical Research* 2012, 45, 1356-1364.
- [17] Z.-H. Huang, G. Liu, F. Kang, *ACS Applied Materials & Interfaces* 2012, 4, 4942-4947.
- [18] C. Petit, T. J. Bandosz, *Advanced Materials* 2009, 21, 4753-4757.
- [19] Y. Guo, Y. Han, S. Shuang, C. Dong, *Journal of Materials Chemistry* 2012, 22, 13166-13173.
- [20] C. Petit, B. Mendoza, T. J. Bandosz, *Langmuir* 2010, 26, 15302-15309.
- [21] M. Jahan, Q. Bao, J.-X. Yang, K. P. Loh, *Journal of the American Chemical Society* 2010, 132, 14487-14495.
- [22] K. S. Park, Z. Ni, A. P. Côté, J. Y. Choi, R. Huang, F. J. Uribe-Romo, H. K. Chae, M. O’Keeffe, O. M. Yaghi, *Proceedings of the National Academy of Sciences* 2006, 103, 10186-10191.
- [23] Y. Pan, Y. Liu, G. Zeng, L. Zhao, Z. Lai, *Chemical Communications* 2011, 47, 2071-2073.
- [24] Z. Jiang, H. Sun, Z. Qin, X. Jiao, D. Chen, *Chemical Communications* 2012, 48, 3620-3622.
- [25] J. Cravillon, S. Münzer, S.-J. Lohmeier, A. Feldhoff, K. Huber, M. Wiebcke, *Chemistry of Materials* 2009, 21, 1410-1412.
- [26] G. Lu, O. K. Farha, W. Zhang, F. Huo, J. T. Hupp, *Advanced Materials* 2012, 24, 3970-3974.
- [27] Q. Song, S. K. Nataraj, M. V. Roussenova, J. C. Tan, D. J. Hughes, W. Li, P. Bourgoïn, M. A. Alam, A. K. Cheetham, S. A. Al-Muhtaseb, E. Sivaniah, *Energy & Environmental Science* 2012, 5, 8359-8369.
- [28] M. M. Dubinin, *Chemical Reviews* 1960, 60, 235-241.
- [29] S. Pan, X. Liu, *Journal of Solid State Chemistry* 2012, 191, 51-56.

---

***Flexible Porous crystal composites of  
a Cd-based MOF and graphene***

---

***Summary***

Homogeneous graphene MOF composites of 2D MOF  $[\text{Cd}_4(\text{azpy})_2(\text{pyrdc})_4(\text{H}_2\text{O})_2] \cdot 9\text{H}_2\text{O}_n$  (CAP) (azpy = 4,4'-azopyridine, pyrdc = pyridine-2,3-dicarboxylate) were synthesized and their adsorptive characteristics studied in detail. For the synthesis of hybrid composites two different functionalized graphene precursors, benzoic acid functionalized graphene and graphene oxide were used. Selective intercalation of functionalized graphene in 2D interlayer space was observed. Pure MOF shows selective  $\text{CO}_2$  uptake with single step type I adsorption profile. Composites show two step  $\text{CO}_2$  adsorption profile with large hysteresis, which indicates strong adsorbate-adsorbent interaction.

## **4.1 Introduction:**

Metal organic frameworks (MOFs) have wide range of applications in various fields like gas storage/separation, catalysis, biomedical and optoelectronic devices due to their unique ordered tunable functional porous environment with high surface area and large pore volume.<sup>[1-5]</sup> Some of the MOFs are flexible and respond reversibly to external stimuli.<sup>[6, 7]</sup> Owing to their flexibility the MOFs show interesting selective gas adsorption and hysteresis in the adsorption profiles.<sup>[8, 9]</sup> Dynamic MOFs have promising applications in selective adsorption, molecular recognition, guest storage and transport.<sup>[10]</sup> Utilization of weak interactions in addition to the coordinate bonds is an important requisite in designing flexible coordination frameworks.<sup>[11]</sup> Coordination bonds in MOFs are often supported by hydrogen bonding, van der Waals forces,  $\pi$ - $\pi$  interaction and other weak interactions which impart flexibility to the framework.<sup>[6, 10]</sup> Crystalline phases are often rigid and MOFs show an exceptional behavior of flexibility in this regard. The dynamic behavior of MOFs is therefore interesting for a study of the adsorption behavior, physical properties and applications.<sup>[12]</sup>

Graphene and various chemically modified forms of have widespread applications in electronics, energy storage devices, polymer composites, sensors and gas storage.<sup>[13-15]</sup> Graphene oxide (GO) which can be synthesized on a large scale by Hummers method is an important precursor for various graphene based materials.<sup>[16, 17]</sup> Benzoic acid functionalized graphene (BFG) synthesized from graphene oxide is another chemically modified form and has been used in the synthesis of MOF composites.<sup>[18]</sup> Epoxide, hydroxyl, carbonyl and carboxylic acid are the main functional group present in GO basal

plane and edges.<sup>[19]</sup> Important functional group in BFG basal plane is benzoic acid. These oxygen containing functional groups acts as coordination center for metal ion. In addition to providing coordination to metal ion they provide interaction by hydrogen bonding,  $\pi$ - $\pi$  interaction and weak van der Waals interaction. Recently various graphene based MOF composites have been reported but the MOF structures are rigid with no flexibility and adsorption property is mainly controlled by rigid MOF framework.<sup>[18, 20-22]</sup> Applications of chemically modified graphene for designing flexible MOFs are largely unexplored. The chemically modified graphene basal plane (GO, BFG) provides weak interactions required for designing flexible framework structure with interesting adsorption property. In this context making use of weak interactions provided by chemically modified graphene we have synthesized flexible graphene MOF composites of  $[\text{Cd}_4(\text{azpy})_2(\text{pyrdc})_4(\text{H}_2\text{O})_2] \cdot 9\text{H}_2\text{O}_n$  (CAP) (azpy = 4,4'-azopyridine, pyrdc = pyridine-2,3-dicarboxylate) with remarkably different adsorption property of composites in comparison to the parent MOF.<sup>[23]</sup> The difference in adsorption properties can be attributed to the synergistic effect in the composites and new interactions provided by the chemically modified graphene basal plane (GO, BFG).<sup>[14]</sup>

## **4.2 Materials and experiments:**

Graphite powder, Cadmium perchlorate hydrate and 2,3-Pyridinedicarboxylic acid were obtained from Sigma Aldrich. 4,4'-Azopyridine was synthesized using the procedure reported in literature.<sup>[24, 25]</sup> Methanol,  $\text{KMnO}_4$ ,  $\text{NaNO}_3$  and other chemicals were obtained from Merck chemicals.

**Synthesis of GO and BFG:**

Detailed procedure for synthesis of GO, RGO and BFG and characterization are given in chapter 2.

**Synthesis of CAP-GO, CAP-BFG and CAP**

Weight of 30 mg GO was dispersed in 50 ml water by sonication for 2 hrs. In the uniform colloidal dispersion Cd (II) ion (~1mmol,  $\text{Cd}(\text{ClO}_4)_2 \cdot x\text{H}_2\text{O}$ ) was added and stirred. After 15 min  $\text{Na}_2\text{pyrdc}$  (1 mmol) and methanolic solution (25 ml) of azpy (1 mmol) was slowly added and allowed to stir overnight. The obtained product was centrifuged and washed with water. Obtained product was dried under vacuum at room temperature. CAP-BFG was obtained by same procedure except the initial dispersion of BFG was obtained by sonication in water maintained at pH 10. CAP was obtained by simple mixing and overnight stirring of ligand solution with metal ion solution.<sup>[23]</sup> Phase purity of obtained product was checked by matching powder X-ray diffraction pattern with simulated pattern.

**Characterization:** Powder X-ray diffraction (PXRD) pattern of obtained composites were recorded on a Bruker D8 Discover instrument using  $\text{Cu-K}\alpha$  radiation. Morphology of CAP-GO, CAP-BFG and CAP were characterized with Transmission electron microscopy (TEM) (JEOL JEM-3010 with an accelerating voltage at 300 KV). SEM images were obtained from Nova Nano SEM 600, FEI Company. Raman spectra of the samples were recorded in backscattering arrangement, using 514.53 nm  $\text{Ar}^+$  laser. Thermogravimetric analysis (TGA) was carried out under nitrogen (flow rate of 50



mL/min) with Metler Toledo TGA-850 TG analyzer in the temperature range between 30 - 900°C at a heating rate 5 °C / min. Infra-red spectra of the compounds were recorded on a Bruker IFS 66v/S spectrophotometer using the KBr pellets in the region 4000-400 cm<sup>-1</sup>.

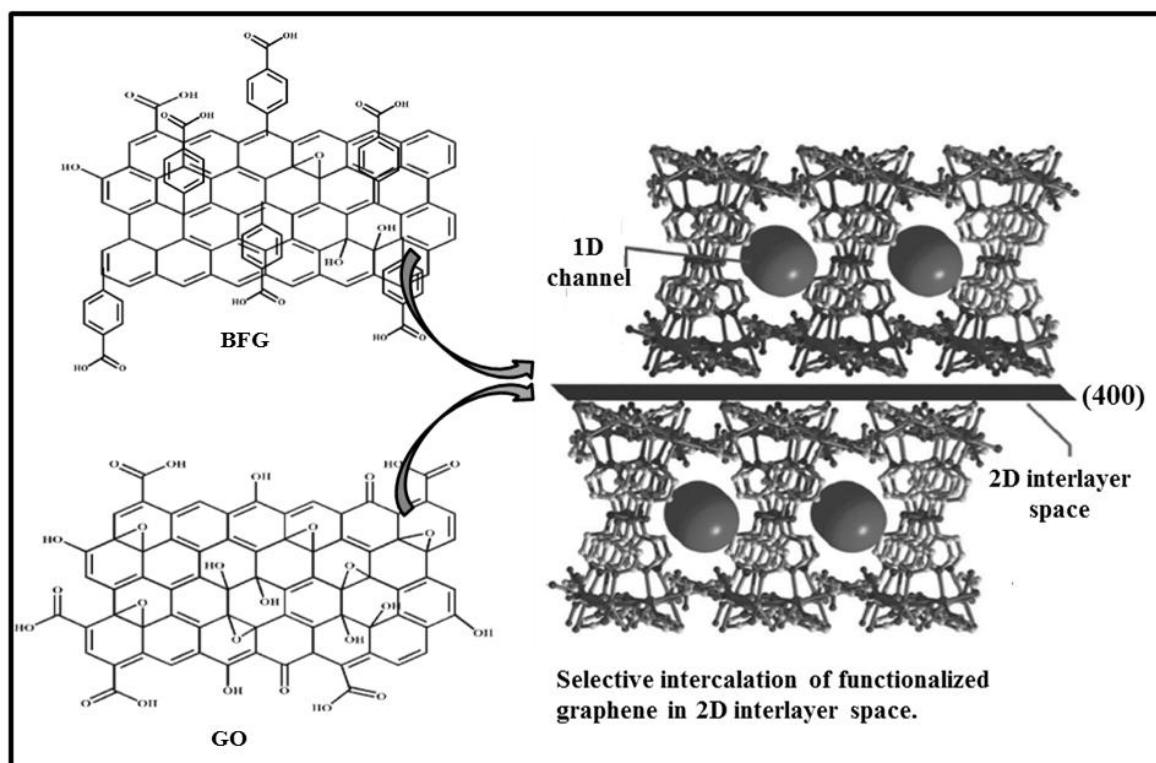
**Gas adsorption measurement:**

The adsorption isotherms for N<sub>2</sub>, (at 77K), and CO<sub>2</sub> (at 195 K) gases were carried out using *QUANTACHROME AUTOSORB-1C* analyzer. The solvent adsorption isotherms (MeOH (at 293 K) and H<sub>2</sub>O) were measured using BELSORP aqua-3 volumetric adsorption instrument from BEL, Japan. A known weight (100-125 mg) of the as-synthesized samples were placed in the sample cell, then, prior to measurements, the samples were dried under high vacuum at 423 K for 12h to remove the adsorbed water molecules. The adsorbate was charged into the sample tube, and change of the pressure was monitored. The degree of adsorption was determined by the decrease in pressure at the equilibrium state. All operations for measurement were computer-controlled and automatic.

### ***4.3 Results and Discussion:***

MOF composites CAP-GO and CAP-BFG were obtained by a simple procedure of room temperature stirring. Ligand solution and metal ion solution were mixed in 10 wt. % GO and BFG colloidal dispersion and stirred at room temperature. [Cd<sub>4</sub>(azpy)<sub>2</sub>(pyrdc)<sub>4</sub>(H<sub>2</sub>O)<sub>2</sub>].9H<sub>2</sub>O<sub>n</sub> (CAP) was synthesized using the same procedure of stirring ligand and metal ion solution. Obtained composites were characterized using PXRD, IR, Raman, TGA, FESEM, TEM and Elemental analysis. Gas and solvent adsorption

property were studied in detail. Scheme 1 shows the proposed bonding and formation of uniform composites CAP-GO and CAP-BFG, which is further supported by PXRD and adsorption measurements. Metal organic frameworks made up of a 2-D structure exhibits greater degree of flexibility due to the possible movement of 2-D networks in response to external stimuli or change in chemical environment in the 2-D networks.<sup>[26]</sup>



**Scheme 1:** Schematic representation of intercalation of functionalized graphene in (400) plane. 2D interlayer space is blocked due to selective intercalation.

This flexibility of structure can be monitored using peak shifts in powder X-ray diffraction of particular plane involved in structural breathing.<sup>[9, 23]</sup> Kanno *et al.* determined the crystal structure of CAP in the monoclinic  $C2/c$  space group, with 2D

pillared bilayer structure.<sup>[23]</sup> Framework Structure consisted of two different adsorbate accessible space 1D channel and 2D space in the interlayer region. 2D corrugated sheets of  $[\text{Cd}_4(\text{pyrdc})_4]_n$  were formed by linking of pyrdc ligands with Cd (II) centre in crystallographic  $bc$  plane. These 2D corrugated sheets were connected by azpy pillars along the crystallographic  $a$  direction to form a 2D pillared bilayer network. Convex type 1-D channels with a window dimension  $\sim 3.5 \times 8.8 \text{ \AA}^2$  were formed along the crystallographic  $c$  axis due to azpy pillars arranged in a criss-cross and canted fashion by  $\pi$ - $\pi$  interaction. The 2D pillared bilayer networks are held in plane by hydrogen bonding interaction between guest water molecules present in 2D interlayer space between two pillared bilayers. Carboxylic acid functional group of pyridine 2,3-dicarboxylate (pyrdc) forms hydrogen bond with water molecules present in the 2D gallery. Figure 4.1 shows the powder X-ray diffraction pattern of composites CAP-GO, CAP-BFG and CAP.

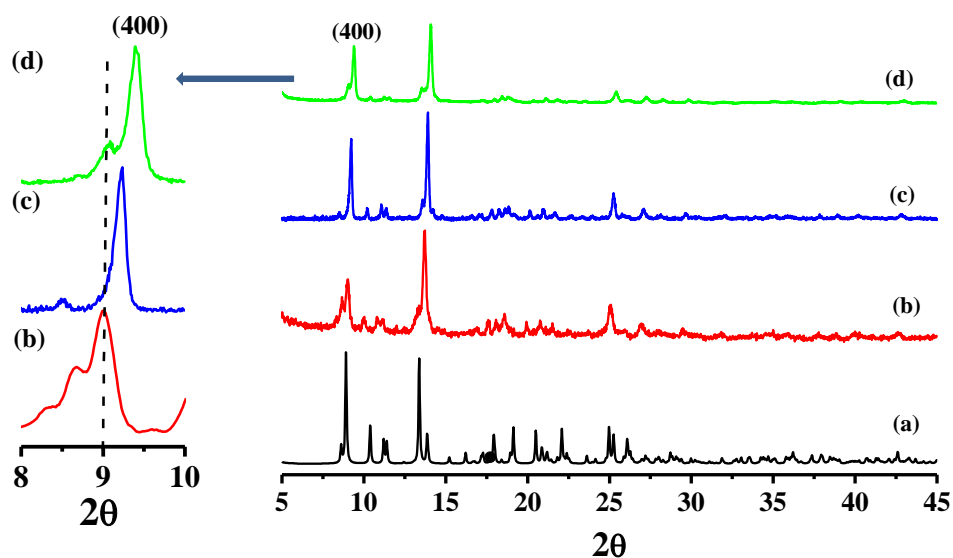


**Figure 4.1** Simulated PXRD pattern of (a)  $[\text{Cd}_4(\text{azpy})_2(\text{prdc})_4(\text{H}_2\text{O})_2] \cdot 9\text{H}_2\text{O}_n$  (CAP) (Black). Observed PXRD pattern of (b) CAP (red), (c) CAP-BFG (blue) and (d) CAP-GO (green). Raman spectroscopy

PXRD pattern matched with simulated pattern with a shift in peak position corresponding to (400) plane in CAP-BFG and CAP-GO. The (400) plane corresponds to 2D interlayer space and gives an important insight in the dynamic behavior of framework. Structural breathing due to flexible motion of pillared bilayers can be easily monitored by observing the peak shift corresponding to (400) plane. A shift to higher  $2\theta$  in (400) plane corresponding to 2D interlayer space was observed in composites CAP-BFG  $\sim 9.12^\circ$  and CAP-GO  $\sim 9.15^\circ$  in comparison to pure MOF CAP  $\sim 9^\circ$ . This shift in PXRD pattern to higher  $2\theta$  in CAP-GO and CAP-BFG can be attributed to intercalation of GO and BFG in 2D bilayer space and competitive hydrogen bonding and other weak interaction with functionalized graphene basal plane instead of water molecules. CAP due to flexibility and hydrogen bonding interaction accommodates water molecules in 2D space and depending on amount of water molecule present in 2D bilayer gallery shift in (400) plane is observed. Benzoic acid functional group present on the basal plane of BFG provides hydrogen bonding interaction with carboxylic acid of pyridine 2, 3-dicarboxylate. Similarly, in GO with epoxide, hydroxyl, carbonyl and carboxylic acid functional group strong hydrogen bonding interaction occurs between neighbouring bilayers. Other important interaction in composites CAP-GO and CAP-BFG is the  $\pi$ - $\pi$  interaction between pyridine moiety of 2D corrugated sheet  $[\text{Cd}_4(\text{pyrdc})_4]_n$  and  $\pi$  electron of GO and BFG. Due to the smaller size of water molecules (kinetic diameter, 2.65 Å) large number of water molecules are intercalated and stabilized by hydrogen bonding interaction in 2D space and a peak at  $2\theta \sim 9^\circ$  is observed in as synthesized CAP under ambient condition. With increase in temperature loss of water molecules from these 2D space occurs, bilayer

comes closer to each other and (400) plane shifts to higher  $2\theta$ . In composites large number of functional group present on graphene basal plane participates in hydrogen bonding,  $\pi$ - $\pi$  interaction and water molecules are excluded. In contrast to the smaller dynamic water molecules functional group on graphene basal plane are rigid and localized, leading to stronger interaction which brings bilayers more close to each other. GO due to more oxygen containing functionality will have more hydrogen bond forming sites in basal plane in comparison to BFG.CAP-GO with more hydrogen bond forming sites will have more stronger interaction between neighboring bilayers in comparison to CAP-BFG. This may be the reason for further shift in (400) peak  $\sim 9.15^\circ$  in CAP-GO in comparison to CAP-BFG  $\sim 9.12^\circ$ . Dynamic behavior of composites and interaction with functionalized graphene were further studied using adsorption measurements.

Raman spectroscopy gives an important insight into the homogeneity and quality of nanocarbon composites.<sup>[27]</sup> From the Raman spectra of all the compounds shown in Figure 4.2 in addition to all the peaks corresponding to MOF, two additional bands at  $1335\text{ cm}^{-1}$  and  $1595\text{ cm}^{-1}$  corresponding to D and G band of BFG can be observed in CAP-BFG.CAP-GO spectrum shows very strong D and G bands at  $1345\text{ cm}^{-1}$  and  $1595\text{ cm}^{-1}$  corresponding to graphene oxide in addition to the peaks corresponding to metal organic framework. As shown in figure 4.3, it is clear that infrared spectra of composites matched with pure MOF.

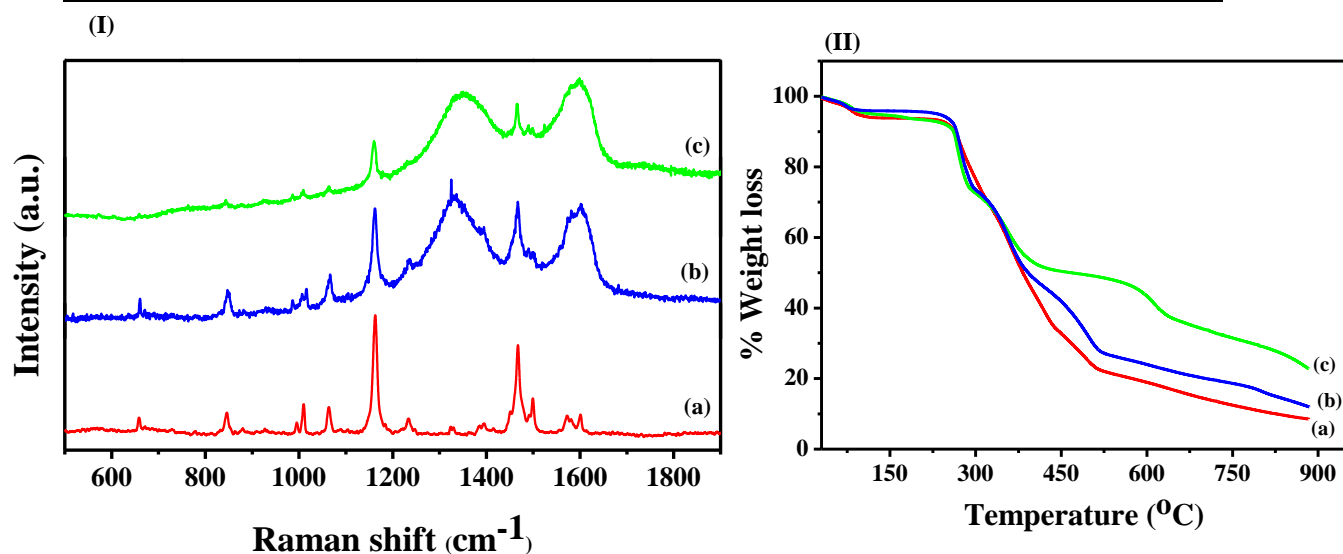


**Figure 4.2** (I) Raman spectra of (a) CAP (red), b) CAP-BFG (blue) and c) CAP-GO (green). (II) TG analysis of (a) CAP (red), (b) CAP-BFG (blue) and (c) CAP-GO (green) at heating rate 5 °C min<sup>-1</sup> under N<sub>2</sub> atmosphere.

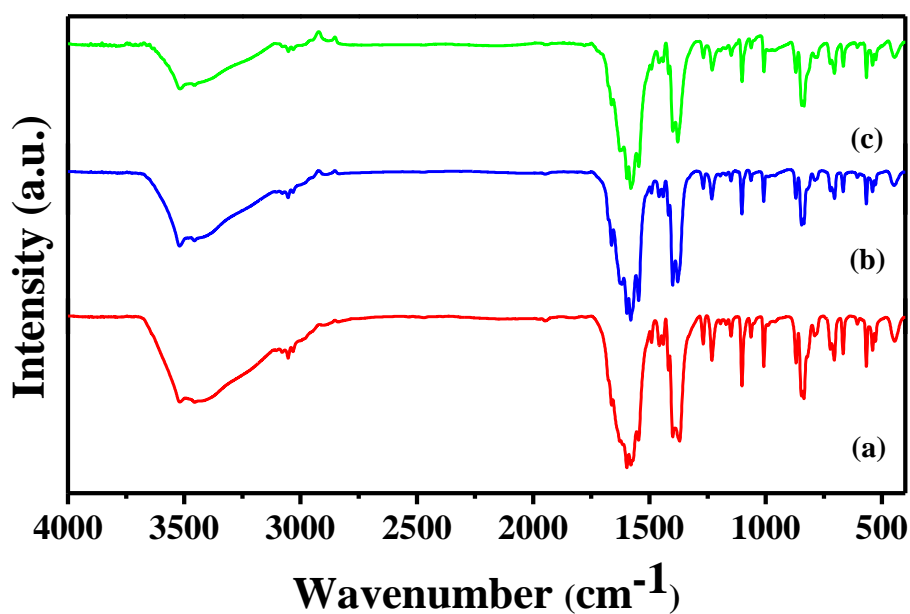


**Figure 4.3** Infrared spectra of (a) CAP (red), (b) CAP-BFG (blue) and (c) CAP-GO (green)

Thermo gravimetric analysis of CAP, CAP-BFG, CAP-GO (Figure 4.2 (II)) shows first weight loss up to 115 °C due to the loss of coordinated water molecules inside the

pores. Second weight loss due to the decomposition of framework was observed at 240 °C. From the TG analysis it can be concluded that the thermal stability of CAP-BFG and CAP-GO are similar to CAP indicating the composites are very uniform and stable.

Morphology of CAP, CAP-BFG and CAP-GO were analyzed using FESEM and TEM. As shown in figure 4.4 shows TEM images of CAP-BFG and CAP-GO composites consisted of thin plate like sheets arranged in layers similar to pure MOF. FESEM (Figure 4.5) images shows that sheet sizes of composites are bigger in comparison to pure MOF which may be due to the nucleation and growth of MOF on large area chemically modified graphene sheets.

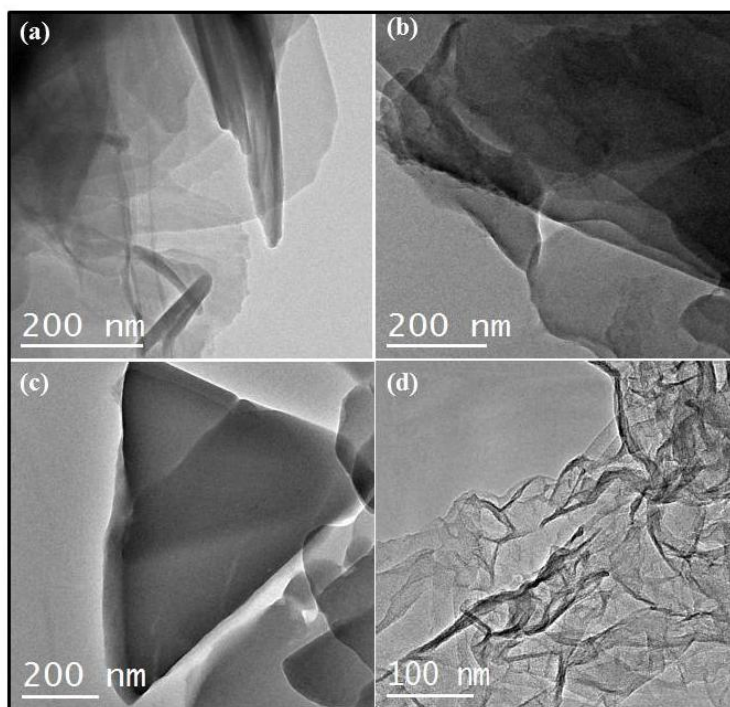


**Figure 4.4** TEM images of (a) CAP-BFG and (b) CAP-GO (c) CAP and (d) RGO used in the synthesis of BFG

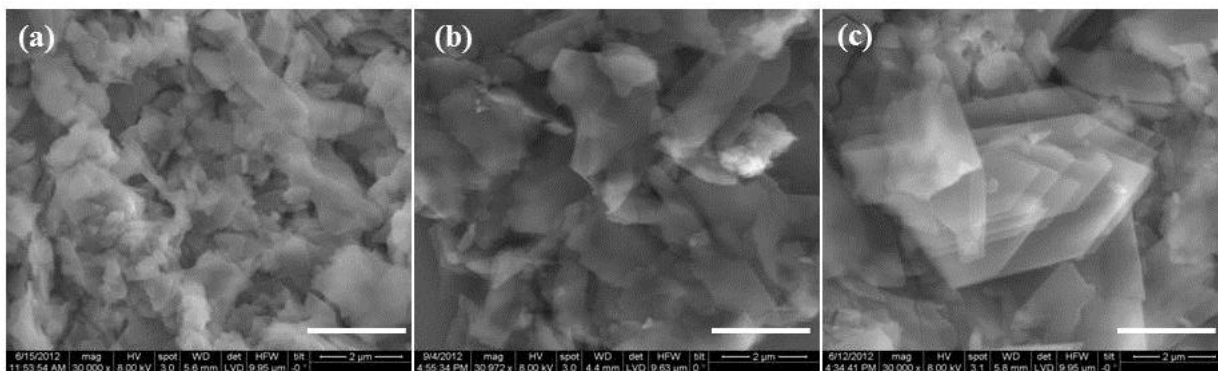


**Figure 4.5** . FESEM images of (a) CAP, (b) CAP-BFG, and (c) CAP-GO showing layered morphology. Scale bar is 2  $\mu\text{m}$ .

Adsorption isotherm gives important information on flexibility of framework, different types of pore and interaction between adsorbate and adsorbent.<sup>[2]</sup> The dynamic behavior of framework and interaction between adsorbate and adsorbent were studied with the help of solvent and gas adsorption. Adsorption behavior of composites CAP-GO and CAP-BFG were different from pure CAP which is also supported by the observed changes in PXRD pattern. Both composites showed selectivity for  $\text{CO}_2$  with negligible  $\text{N}_2$  uptake. This selectivity for adsorption of a particular gas is an important property of flexible frameworks which gives it capability in molecular recognition and separation.<sup>[7,</sup>  
<sup>28]</sup> Figure 4.6 shows  $\text{CO}_2$  adsorption isotherm of CAP and composites at 195 K. CAP with two different adsorbate accessible spaces 1D channel and 2D interlayer space showed type I  $\text{CO}_2$  adsorption isotherm due to adsorption in micropores. Isotherm showed sharp  $\text{CO}_2$  uptake up to  $P/P_0 \sim 0.1$  with a final uptake of 32 ml/g at  $P/P_0 \sim 1$ . Carbon dioxide with suitable kinetic diameter (3.3 Å) and quadrupole moment ( $-1.4 \times 10^{-39} \text{ Cm}^2$ ) interacts with  $-\text{COO}$  and  $-\text{N}=\text{N}-$  functional group present on the surface



of 1D channel.<sup>[29]</sup> Such fruitful interaction helps in overcoming the diffusion barrier in 1D channel. CO<sub>2</sub> adsorption occurs selectively in 1D channel and a single step adsorption profile is observed. The CO<sub>2</sub> adsorption isotherm of CAP-BFG and CAP-GO showed two step uptakes which is remarkably different from CAP. In the first step up to  $P/P_0 \sim 0.1$  CAP-GO and CAP-BFG shows adsorption of  $\sim 5$  ml and  $\sim 9$  ml CO<sub>2</sub> respectively followed by onset of second step.  $P/P_0 \sim 0.1$  corresponds to threshold pressure for gate opening in bilayers and the bilayers starts moving with respect to each other. First step before  $P_{th} \sim 0.1$  is due to adsorption of CO<sub>2</sub> in 1D channel. Low uptake of CO<sub>2</sub> in the first step may be due to the blocking of 1D channel with nonporous GO and BFG.

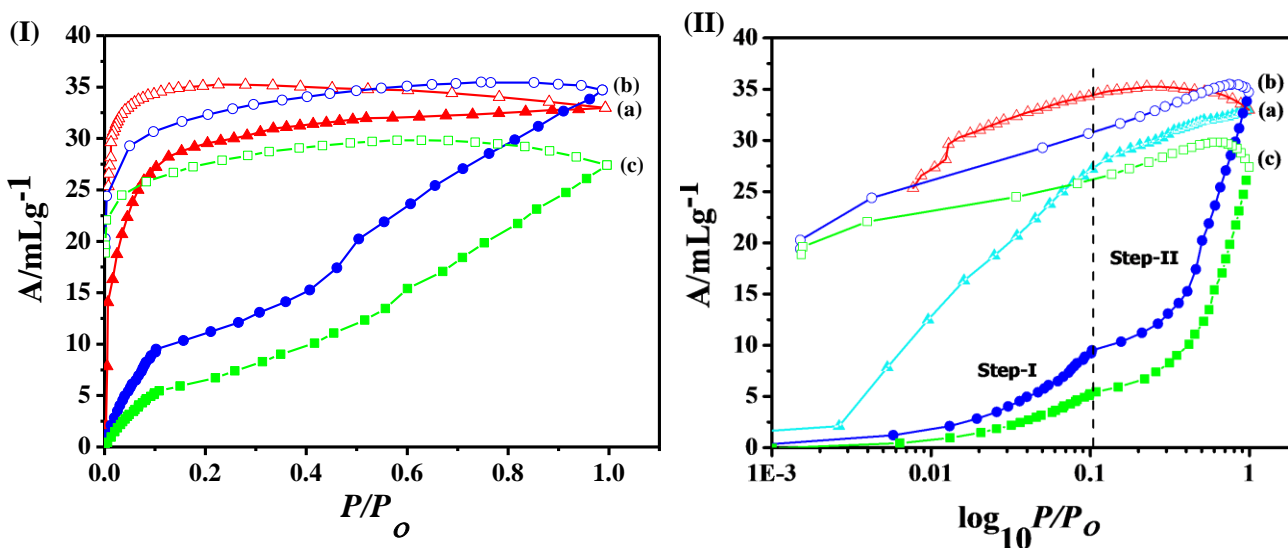


**Figure 4.6** (I) CO<sub>2</sub> sorption isotherm at 195 K (a) CAP adsorption (red filled triangles) and desorption (red open triangles), (b) CAP-BFG adsorption (blue filled circles) and desorption (blue open circles), (c) CAP-GO adsorption (green filled squares) and desorption (green open square). (II) Plots in log scale showing two step CO<sub>2</sub> uptake.

After  $P_{th}$  diffusion of  $CO_2$  molecules occurs in the 2D interlayer space and slow increase in adsorbed amount with final uptake of 27 ml and 34 ml at  $P/P_0 \sim 1$  is observed for CAP-GO and CAP-BFG respectively. This slow increase in adsorption after  $P_{th}$  in second step is different from reported stepwise adsorption profile in literatures, where a sharp increase in adsorption near  $P_{th}$  is generally observed. The cooperative interaction of large ensemble of adsorbate with adsorbent brings the required structural change and stepwise adsorption is observed at  $P_{th}$ . This cooperative interaction depends on the property adsorbent and hence interaction between adsorbate and adsorbent. GO and BFG owing to the functional group on its basal plane provides strong interaction to quadrupolar  $CO_2$  molecule. Due to this strong interaction between  $CO_2$  and oxygen functionality of GO and BFG, adsorption of  $CO_2$  occurs in 2D interlayer space in the second step. The dimension of 2D interlayer space is smaller than that of the 1D channel and slow diffusion of  $CO_2$  in the 2D interlayer space dominated by strong interaction with functional groups of graphene basal plane may be the reason for slow increase in  $CO_2$  uptake in the second step. Large hysteresis was observed in adsorption profile of CAP-GO and CAP-BFG which supports the strong interaction of  $CO_2$  with composites. Although an increase in  $CO_2$  uptake is expected when adsorption in both 1D channel and 2D interlayer space occurs, uptake amount of CAP-BFG and CAP-GO are comparable to CAP. This comparable value is due to the low uptake in the first step in CAP-BFG and CAP-GO in comparison to CAP. Figure 4.7 (I) and (II) shows the MeOH (at 293 K) and  $H_2O$  (at 298 K) adsorption profile. Both CAP-GO and CAP-BFG showed single step adsorption with the final uptake of 99 ml and 109 ml respectively due to adsorption in 1D channel. This single step adsorption of CAP-GO and CAP-BFG is different from CAP

which shows double step adsorption due to adsorption in both 1D channel and 2D interlayer space. GO and BFG present in 2D interlayer space interacts with the neighbouring bilayer by hydrogen bonding and competes with MeOH and H<sub>2</sub>O.

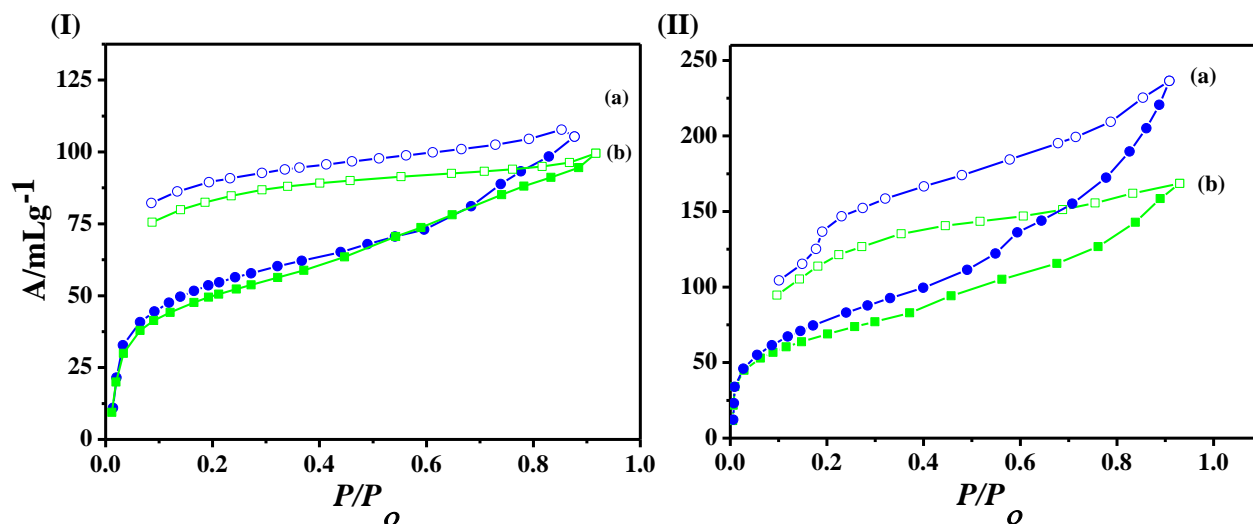


**Figure 4.7** (I) Methanol sorption isotherm of (a) CAP-BFG adsorption (blue filled circles) and desorption (blue open circles) and (b) CAP-GO adsorption (green filled squares) and desorption (green open squares) at 293 K. (II) Water sorption isotherm of (a) CAP-BFG adsorption (blue filled circles) and desorption (blue open circles) and (b) CAP-GO adsorption (green filled squares) and desorption (green open squares) at 298 K

The diffusion barrier for MeOH and H<sub>2</sub>O in 2D layer is compensated by the energy released from the hydrogen bond formation. Now with oxygen functionality present on GO and BFG participating in hydrogen bond formation diffusion of MeOH and H<sub>2</sub>O in 2D interlayer space is not favourable. Similar single step adsorption profile due to adsorption in 1D channel was also obtained for H<sub>2</sub>O. Water uptake was higher in CAP-BFG and CAP-GO in comparison to CAP which may be due to the cluster formation at higher pressure. Figure 4.8 shows N<sub>2</sub> adsorption profile of CAP-GO and CAP-BFG

Composites CAP-GO and CAP-BFG showed negligible N<sub>2</sub> uptake with type II adsorption profile.

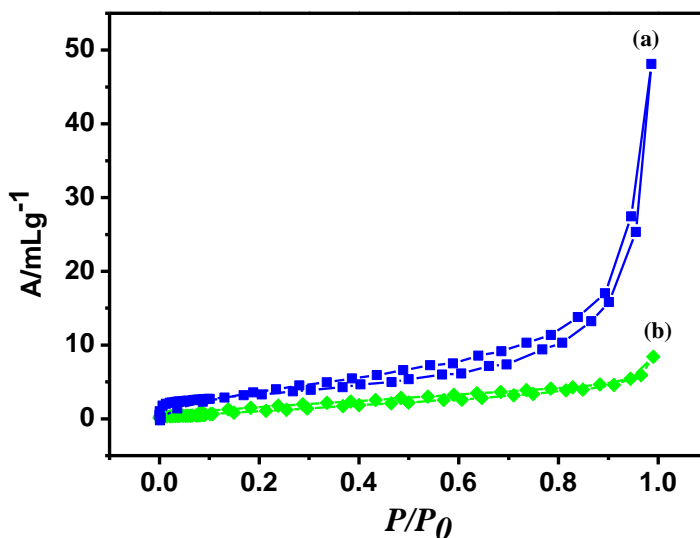


**Figure 4.8** N<sub>2</sub> adsorption isotherm of (a) CAP-BFG (blue squares) and (b) CAP-GO (green diamond) at 77 K

## **4.4 Conclusions:**

Hydrogen bonding,  $\pi$ - $\pi$  interaction and other weak interactions provided by benzoic acid functionalized graphene and graphene oxide were utilized in designing flexible MOF graphene composites. The composites, CAP-GO and CAP-BFG, based on a Cd containing MOF show a double-step CO<sub>2</sub> adsorption profile and hysteresis, with the second step having higher contribution in CO<sub>2</sub> uptake. This is different from pure CAP where only the 1D channel participates in adsorption and a single step is observed in CO<sub>2</sub> uptake. Weak interactions enabled by the graphene oxide basal plane and functionalized graphene in designing flexible MOFs are largely unexplored. Such composites making

use of functionalities present in the graphene basal plane may find applications in separation processes, storage, sensing and catalysis.

### References:

- [1] A. K. Cheetham, C. N. R. Rao, *Science* 2007, *318*, 58-59.
- [2] S. Kitagawa, R. Kitaura, S.-i. Noro, *Angewandte Chemie International Edition* 2004, *43*, 2334-2375.
- [3] G. Ferey, *Chemical Society Reviews* 2008, *37*, 191-214.
- [4] A. U. Czaja, N. Trukhan, U. Muller, *Chemical Society Reviews* 2009, *38*, 1284-1293.
- [5] M. D. Allendorf, C. A. Bauer, R. K. Bhakta, R. J. T. Houk, *Chemical Society Reviews* 2009, *38*, 1330-1352.
- [6] K. Uemura, R. Matsuda, S. Kitagawa, *Journal of Solid State Chemistry* 2005, *178*, 2420-2429.
- [7] P. Kanoo, R. Sambhu, T. K. Maji, *Inorganic Chemistry* 2010, *50*, 400-402.
- [8] A. J. Fletcher, K. M. Thomas, M. J. Rosseinsky, *Journal of Solid State Chemistry* 2005, *178*, 2491-2510.
- [9] R. Kitaura, K. Fujimoto, S.-i. Noro, M. Kondo, S. Kitagawa, *Angewandte Chemie International Edition* 2002, *41*, 133-135.
- [10] S. Horike, S. Shimomura, S. Kitagawa, *Nat Chem* 2009, *1*, 695-704.
- [11] S. Kitagawa, K. Uemura, *Chemical Society Reviews* 2005, *34*, 109-119.
- [12] S. Bureekaew, S. Shimomura, S. Kitagawa, *Science and Technology of Advanced Materials* 2008, *9*, 014108.
- [13] C. N. R. Rao, A. K. Sood, K. S. Subrahmanyam, A. Govindaraj, *Angewandte Chemie International Edition* 2009, *48*, 7752-7777.
- [14] K. E. Prasad, B. Das, U. Maitra, U. Ramamurty, C. N. R. Rao, *Proceedings of the National Academy of Sciences* 2009, *106*, 13186-13189.
- [15] K. S. Subrahmanyam, P. Kumar, U. Maitra, A. Govindaraj, K. P. S. S. Hembram, U. V. Waghmare, C. N. R. Rao, *Proceedings of the National Academy of Sciences* 2011.
- [16] W. S. Hummers, R. E. Offeman, *Journal of the American Chemical Society* 1958, *80*, 1339-1339.
- [17] D. R. Dreyer, S. Park, C. W. Bielawski, R. S. Ruoff, *Chemical Society Reviews* 2010, *39*, 228-240.
- [18] M. Jahan, Q. Bao, J.-X. Yang, K. P. Loh, *Journal of the American Chemical Society* 2010, *132*, 14487-14495.
- [19] H. He, T. Riedl, A. Lerf, J. Klinowski, *The Journal of Physical Chemistry* 1996, *100*, 19954-19958.
- [20] C. Petit, T. J. Bandosz, *Advanced Materials* 2009, *21*, 4753-4757.
- [21] C. Petit, B. Mendoza, T. J. Bandosz, *Langmuir* 2010, *26*, 15302-15309.
- [22] C. Petit, B. Mendoza, T. J. Bandosz, *ChemPhysChem* 2010, *11*, 3678-3684.

- 
- [23] P. Kanoo, G. Mostafa, R. Matsuda, S. Kitagawa, T. Kumar Maji, *Chemical Communications* 2011, 47, 8106-8108.
- [24] E. V. Brown, G. R. Granneman, *Journal of the American Chemical Society* 1975, 97, 621-627.
- [25] O. Theilmann, W. Saak, D. Haase, R. d. Beckhaus, *Organometallics* 2009, 28, 2799-2807.
- [26] K. Biradha, Y. Hongo, M. Fujita, *Angewandte Chemie* 2002, 114, 3545-3548.
- [27] M. S. Dresselhaus, A. Jorio, R. Saito, in *Annual Review of Condensed Matter Physics, Vol 1, Vol. 1* (Ed.: J. S. Langer), Annual Reviews, Palo Alto, **2010**, pp. 89-108.
- [28] S. Horike, D. Tanaka, K. Nakagawa, S. Kitagawa, *Chemical Communications* 2007, 0, 3395-3397.
- [29] R. Vaidhyanathan, S. S. Iremonger, G. K. H. Shimizu, P. G. Boyd, S. Alavi, T. K. Woo, *Science* 2010, 330, 650-653.

***Robust porous graphene  
frameworks pillared by organic  
linkers, with tunable surface area  
and gas storage***

---

***Summary***

A procedure making use of the Pd(0) catalyzed coupling reaction has been developed for the synthesis of high surface area graphene based 3D porous graphene frameworks. These porous solids have high BET surface areas up to 825 m<sup>2</sup>/g which is higher than the reduced graphene oxide precursor (RGO, 40 m<sup>2</sup>/g). The pillared porous solids have remarkably high CO<sub>2</sub> uptake of 112 wt.% at 195 K and 1 atm. High pressure CO<sub>2</sub> measurements shows uptake of 43 wt.% (34 bar) and 31 wt.% (55 bar) at 273 K and 298 K respectively. Porous solids have hydrogen uptake of up to 2.1 wt.% at 77 K and 1 bar pressure. The 3D pillared porous solids have high thermal and chemical stability. Utilization of very light weight and mechanically strong graphene sheets in the synthesis of such high performance pillared porous solids is promising. The Pd(0) catalyzed synthesis procedure is highly efficient and can be utilized for covalent modifications of nanocarbons.

## **5.1 Introduction:**

Graphene has emerged to become an exciting two-dimensional material with many unique properties.<sup>[1-5]</sup> Besides its unusual electronic properties, it is associated with high-surface areas, the predicted value being close to 2600 m<sup>2</sup>/g. Very high surface area in combination with high mechanical and thermal stability makes graphene one of the best materials for storage, sensing and catalyst support.<sup>[6-8]</sup> However theoretically predicted high surface area is hardly achieved due to strong  $\pi$ - $\pi$  interaction between individual graphene sheets. Application of graphene for gas storage applications needs synthesis of graphene in large scale which can be achieved by reduction of graphene oxide.<sup>[9, 10]</sup> Graphene synthesized by reduction of graphene oxide contains residual oxygen functionality such as epoxy, hydroxyl and carboxyl groups. These functional groups in addition to strong  $\pi$ - $\pi$  interactions further increases interaction between individual graphene sheets and decreases adsorbate accessible space. Various noncovalent interactions between graphene and intercalating molecules have been utilized to decrease strong  $\pi$ - $\pi$  interactions.<sup>[4, 11]</sup> Utilization of very light weight graphene sheets with high mechanical, thermal and chemical stability by covalently linking individual graphene sheets using definite length linkers can be a promising approach for very high performance porous solids. The improvement in permanent porosity with high specific surface area and monolayer pore surface is a key for gas storage applications. Such pillared nanostructures connecting individual graphene sheets and carbon nanotubes have been theoretically studied for hydrogen storage applications.<sup>[12-16]</sup>



Recently Yildirim et.al reported construction of pillared graphene oxide (GO) framework based on 1,4-diboronic acid linkage.<sup>[17]</sup> However, the surface area has not significantly increased. High O/C ratios due to the direct use of GO resulted in reduced surface area.<sup>[18]</sup> Moreover, GO is hydrophilic and the presence of boronate ester linkage, a moisture sensitive group, would further diminish its chemical stability. Thermal stability of GO is limited due to the presence of large concentration of oxygen functionality on GO basal plane.<sup>[19]</sup> Therefore further development of tailorable graphene based materials with high thermal and chemical stability, tunable surface area with modular pore surface is essential for storage of the hydrogen and carbon dioxide.

With this objective in mind construction of 3D pillared graphene materials by covalently linking functionalized reduced graphene oxide sheets (RGO) by different organic linkers was envisioned. We have used Pd catalyzed Sonogashira coupling reaction for covalently linking individual Iodobenzene functionalized graphene (IBZ-RGO) sheets. Two different linkers were used to connect graphene sheets and obtained porous solids are denoted as PGF-1 and PGF-2. Obtained porous solids PGF-1 and PGF-2 showed large increase in surface area in comparison to RGO and very high CO<sub>2</sub> uptake. These porous solids will have potential application in gas storage/separation, CO<sub>2</sub> sequestration and catalysis.

To the best of our knowledge this is the first report of application of Pd catalyzed C-C coupling reaction in chemically modifying nanocarbon basal plane. Although we have used Pd catalyzed coupling reaction for the synthesis of porous solids, the synthesis procedure can be applied in other systems for covalent modification of nanocarbon. Different synthesis procedure for aryl halide functionalization of carbon nanotube and

graphene are reported in literature.<sup>[20-24]</sup> Aryl halide functionalized nanocarbons can be further connected with different functionalities using very efficient palladium catalyzed C-C or C-N coupling reactions.<sup>[25]</sup> The traditional approach of carboxylic acid functionalization using HNO<sub>3</sub> and H<sub>2</sub>SO<sub>4</sub> followed by reaction with SOCl<sub>2</sub> and amide bond formation using amino group containing molecules creates defects on the basal plane due to the cleavage of C=C bonds and formation of -COOH functional groups.<sup>[26]</sup> Owing to the well-known chemistry of Pd catalyzed coupling reactions, this new approach of chemically modifying aryl halide functionalized nanocarbons will start a new synthetic protocol in nanocarbon chemistry.<sup>[4, 26-29]</sup>

## **5.2 Materials and experiments:**

Graphite powder was obtained from Alfa aesar. 4-Iodoaniline (98%) and Pd(PPh<sub>3</sub>)<sub>4</sub> were obtained from Sigma Aldrich. Other chemicals were obtained from Merck chemicals unless otherwise mentioned. The chemicals were of high purity grade.

### **Synthesis of Graphite Oxide:**

Graphite oxide was synthesized using modified Hummers method.<sup>[9]</sup> In an ice bath 75 ml conc. H<sub>2</sub>SO<sub>4</sub> was mixed with 1.5 g graphite powder and 1.5 g NaNO<sub>3</sub> and allowed to stir for 10 min. In the uniform mixture 10 g of KMnO<sub>4</sub> was added slowly and allowed to mix properly. The reactants were transferred to oil bath maintained at 40°C and stirred for another 45min. To this mixture 75 ml distilled water was added followed by stirring

for 15min at 70 °C. Uniform brown colour suspension was formed. The temperature was then raised to 80 °C and 15ml H<sub>2</sub>O<sub>2</sub> in 150ml warm water (~70 °C) was added. The color of suspension changed from brown to yellow. Obtained product was centrifuged and washed repeatedly with deionized water. Graphite oxide was again dispersed in water and dialyzed till dialysate became neutral. Product was then centrifuged to remove excess water. Obtained solid product was transferred to petri dish and dried under vacuum at room temperature.

### **Reduction of Graphite Oxide:**

Obtained graphite oxide was dispersed in water and reduced using NaBH<sub>4</sub> according to the procedure reported in literature.<sup>[30]</sup> In a round bottom flask 400 mg of GO was dispersed in 320 ml water by sonication. The pH was adjusted to 10 by adding 5% Na<sub>2</sub>CO<sub>3</sub> solution. Then, the dispersion was stirred at 90 °C for 9 hours. The pH was again checked using a pH meter and adjusted to 10. Then, 3.2g NaBH<sub>4</sub> (0.085mol) in 80ml H<sub>2</sub>O was added to dispersion under constant stirring, with temperature maintained at 80 °C. The dispersion was stirred for next 3 hours. The color of dispersion changed from dark brown to black accompanied by outgassing. The final product was filtered and washed several times with water and ethanol and dried under vacuum.

### **Iodobenzene functionalization of graphene**

Diazonium salt used for iodobenzene functionalization of graphene was prepared in situ using 4-Iodoaniline. 4-Iodoaniline (4.3 mmol, 961 mg) was dissolved in 80 ml water

by adding minimum amount of HCl drop wise. 4-Iodoaniline solution was then transferred to a round bottom flask maintained at 0 °C in an ice bath. To this solution NaNO<sub>2</sub> (7 mmol, 483 mg ) and 4 ml 20% HCl (6.4 M, 12.8 mmol) was added and allowed to stir for 45 min. Colour of solution changed from transparent to yellow due to the formation of diazonium salt. Reduced graphene oxide obtained after sodium borohydride reduction was agglomerated with poor dispersion in water. RGO (125 mg) was dispersed in 125 ml 1 wt.% sodium dodecylbenzene sulfonate (SDBS) surfactant solution. RGO dispersion was then added to diazonium salt solution. Reactant mixture was maintained at 0°C for next 2 hours followed by stirring at room temperature for next 4 hours. Obtained product was filtered and washed with copious amount of water, (1:1) water-ethanol solution, ethanol and THF to remove the surfactant properly. Final product was dried in vacuum desiccator at room temperature.

### **Synthesis of RGOF-1:**

In a typical procedure, mixture of IBZ-RGO (40mg), 1,4-diethynylbenzene (177mg), Pd(PPh<sub>3</sub>)<sub>4</sub> (3mol%), CuI (6mol%) were degassed by four freeze-thaw pump cycles and purged with N<sub>2</sub>. To this 2 mL dry DMF and 1mL anhydrous triethylamine were added under continuous N<sub>2</sub> flow. Reaction mixture was stirred at 140 °C for 48 hrs and cooled to room temperature. Precipitates were collected by filtration and washed several times with water, ethanol and tetrahydrofuran. Further purification was carried out using Soxhlet extraction technique with methanol and THF for 24hrs each. Compounds were dried under vacuum at room temperature for 24 hrs. Yield: 83%. FTIR in KBr (cm<sup>-1</sup>): 3428(br), 3293(br), 3027(w), 2919(w), 2184(w), 1907 (w), 1664(br),

1600(s), 1502(m), 1384(m), 1261(w), 1178(w), 1099(s), 1016(m), 898(sh), 833(s), 543(w).r

### **Synthesis of RGOF-2:**

Similar procedure is followed as in RGOF-1, except 4, 4'-diethynylbiphenyl in the presence of linker. Yield: 78%. FTIR in KBr ( $\text{cm}^{-1}$ ): 3438(br), 3299(br), 3029(w), 2919(w), 2184(w), 1909 (w), 1664(br), 1604(s), 1492(m), 138(m), 1261(w), 1178(w), 1099(s), 1004(m), 898(sh), 833(s), 543(w).

### **Physical Measurements**

Infrared spectra of samples were recorded on a Bruker IFS 66v/S using KBr pellets. Raman spectra were recorded in backscattering geometry using Jobin Yvon LabRam HR spectrometer with 514.53 nm  $\text{Ar}^+$  laser. Thermogravimetric analyses (TGA) were carried out on Mettler Toledo TGA850 instrument with a heating rate of 3  $^{\circ}\text{C}/\text{min}$  in  $\text{N}_2$  atmosphere. FESEM images of PGF-1 and PGF-2 were obtained from Nova Nano SEM 600, FEI Company. TEM images were obtained with a FEI TITAN microscope operating at an accelerating voltage of 80 kV. XPS spectra were recorded using omicron spectrometer. XPS samples were prepared by drop casting samples on Si substrate with native  $\text{SiO}_2$  coating. Solid state NMR measurements were performed using Bruker solid state NMR spectrometer.

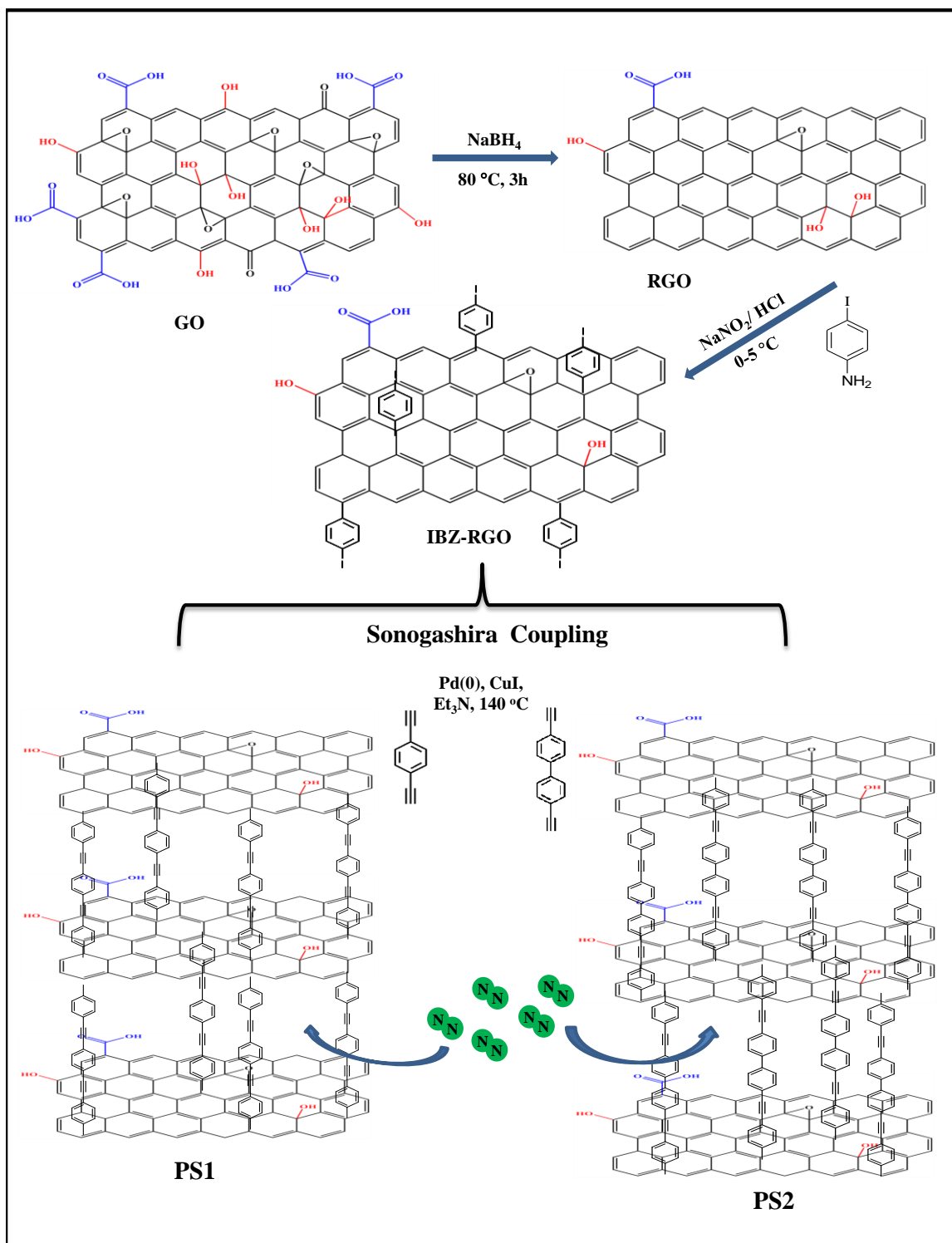
### **Gas adsorption measurement:**

All the samples were activated at 160  $^{\circ}\text{C}$  prior to gas adsorption measurements. The adsorption isotherm for  $\text{N}_2$ , (at 77K), and  $\text{CO}_2$  (at 195 K) were obtained using *QUANTACHROME AUTOSORB-1C* analyzer. The adsorbates were charged into the

sample tube, and change in pressure was monitored. The degree of adsorption was determined by monitoring the decrease in pressure at the equilibrium state. High-pressure H<sub>2</sub> adsorption measurements were carried out at 77 K. High pressure CO<sub>2</sub> adsorption measurements were carried out at 273 K and 298 K. The measurements were performed in a fully computer controlled volumetric BELSORP-HP, BEL JAPAN high pressure instrument. Non-ideal corrections for H<sub>2</sub> and CO<sub>2</sub> gases were done by applying virial coefficients at respective measurement temperatures. All the gases used in adsorption study were high purity scientific/ research grade.

### **5.3 Results and Discussion:**

Scheme 1 shows the synthesis steps involved in PGF-1 and PGF-2. Initial reduction step of graphene oxide using sodium borohydride reduces oxygen functionality.<sup>[30]</sup> Small concentration of oxygen functionality remains after reduction. Obtained RGO was functionalized with Iodobenzene using in-situ prepared diazonium salt.



**Scheme 5.1:** Synthesis steps involved in PGF-1 and PGF-2 using Pd(0) Sonogashira coupling reaction.

Iodobenzene functionalized RGO (IBZ-RGO) sheets were coupled using Pd(0) catalyzed Sonogashira coupling reactions with two different linkers 1,4-diethynylbenzene (**PGF-1**) and 4, 4'-diethynylbiphenyl (**PGF-2**). Infrared spectrum of RGO (Figure 5.1 (I)) have peaks at  $1580\text{ cm}^{-1}$  due to C=C stretching vibration, low intensity shoulder peak near  $1720\text{ cm}^{-1}$  indicates efficient reduction of graphene oxide. UV spectra of GO and RGO (Figure 5.1 (II)) have peaks at 227 nm and 250 nm respectively due to  $\pi\rightarrow\pi^*$  transition. Red shift in  $\pi\rightarrow\pi^*$  transition of RGO is due to partial recovery of conjugation after reduction. Iodobenzene functionalization of graphene (IBZ-RGO) was characterized using IR and XPS spectroscopy. IR spectrum of IBZ-RGO has strong C-I stretching band at  $467\text{ cm}^{-1}$  (Figure 5.2 (II)). XPS Survey scan of IBZ-RGO (Figure 5.2 (I)) shows peaks at 621 eV and 632.5 eV due to I  $3d_{5/2}$  and I  $3d_{3/2}$  from Iodobenzene functional groups on graphene basal plane.<sup>[31]</sup>

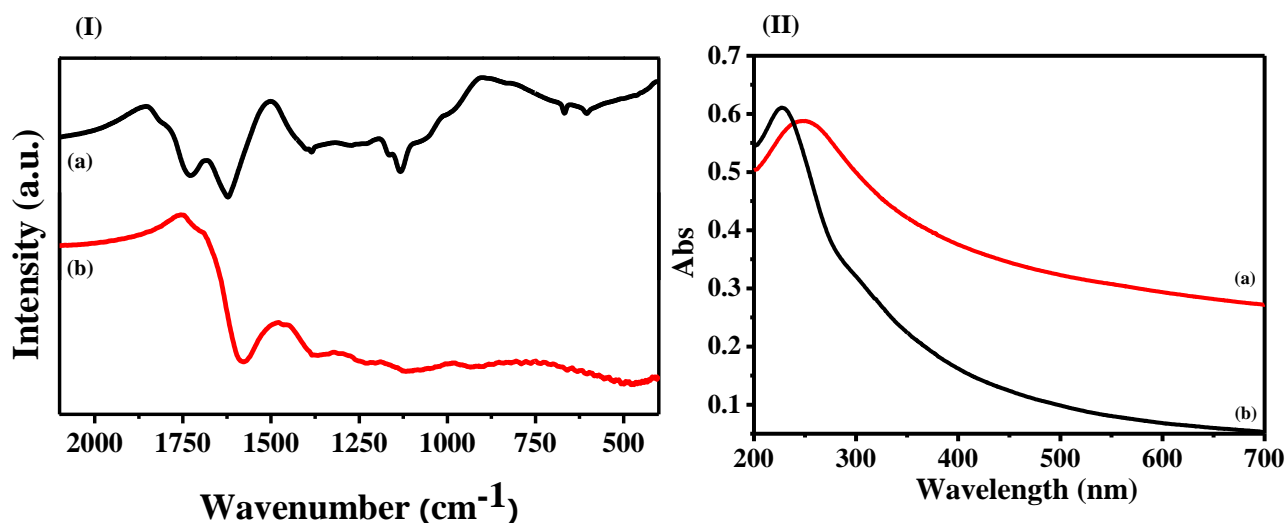


**Figure 5.1** (I) IR spectra of (a) GO (black) and (b) RGO. (II) UV-visible absorption spectra of (a) RGO (red) and (b) GO (black)



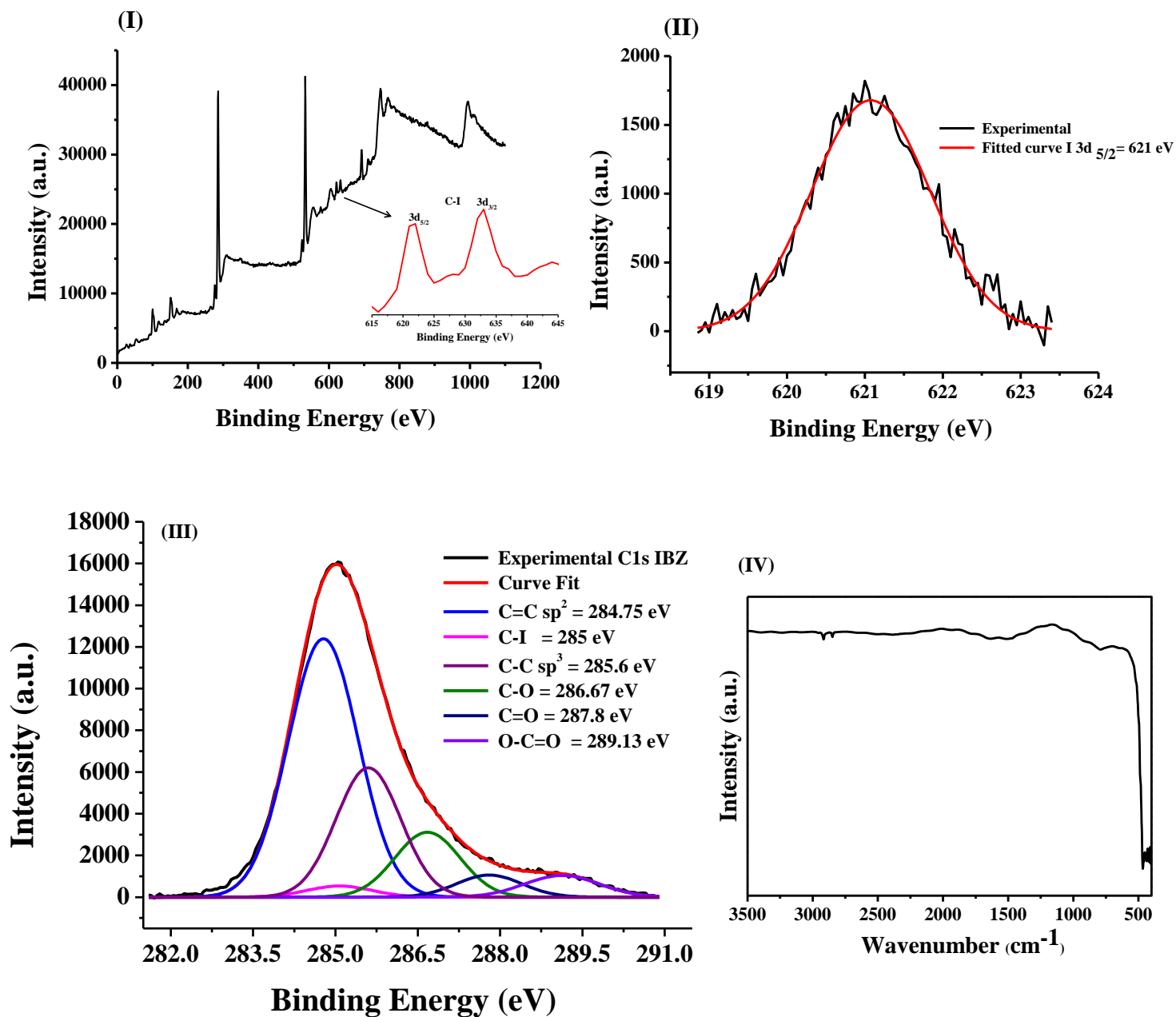


**Figure 5.2** (I) Survey scan of IBZ-RGO. (II) High resolution XPS spectra I  $3d_{5/2}$ . (III) High resolution C1s XPS spectra of IBZ-RGO. (IV) IR spectrum of IBZ-RGO.

Obtained porous solids PGF-1 and PGF-2 were characterized using direct pulse  $^{13}\text{C}$  solid state NMR spectroscopy. Figure 5.3 shows the  $^{13}\text{C}$  NMR spectrum of PGF-1 at 10 kHz MAS. SSNMR spectra of RGO, RGO-IBZ and PGF-2 were collected at 5 kHz MAS (Figure 5.4). SSNMR spectrum of PGF-1 shows broad unresolved peak from 120 ppm to 145 ppm due to  $\text{sp}^2$  carbon present in different chemical environment. Presence of moderate signal about 91 ppm corresponding to  $-\text{C}\equiv\text{C}-$  bond confirms connection of bridging linkers 1,4-diethynyl benzene in-between layers of IBZ-RGO resulting in pillared 3D porous structure. Very weak intensity peak near 170 ppm can be attributed to remaining carboxylic acid group of graphene after reduction.<sup>[32]</sup> Weak broad signal at 60 ppm merging with spinning side band is probably due to remaining small concentration of epoxide functional group of RGO. No signal at 70 ppm corresponding to hydroxyl group was observed in PGF-1.

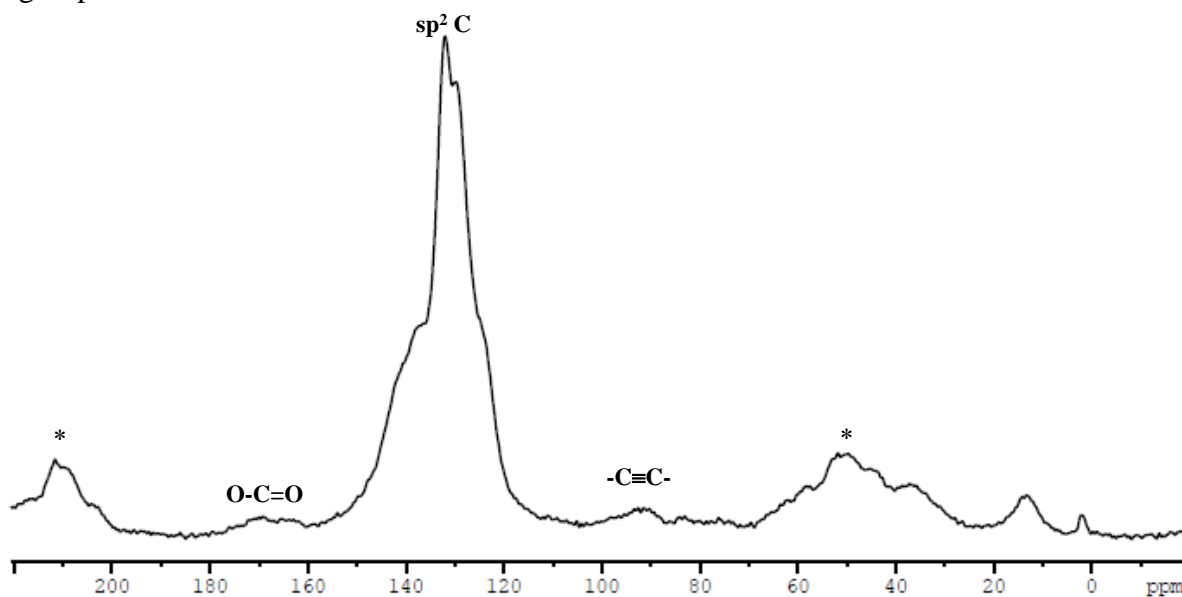


**Figure 5.3** Direct pulse  $^{13}\text{C}$  NMR spectrum of PGF-1 at 10 kHz MAS. Aestrik represents spinning sidebands.

Poor signal to noise ratio of NMR spectra collected at 5 kHz limited the identification of functional groups present in low concentration. NMR spectra of RGO and RGO-IBZ showed broad peak centered at 118 ppm and 121 ppm due to  $sp^2$  carbon with no significant observable intensity at 60 ppm and 70 ppm corresponding to epoxide and hydroxyl functional groups. Although no peak with observable intensity corresponding to epoxide, hydroxyl and carboxylic acid functional groups are observable in NMR spectrum, detection of peak in our NMR spectra is limited by the poor S/N ratio and small concentration of these functional groups. NMR spectrum of RGO is consistent with literature reports of sample prepared by reduction of GO using sodium borohydride.<sup>[10, 33]</sup> Even at poor S/N ratio peak near 91 ppm corresponding to  $-C\equiv C-$  can be observed in 5 kHz spectrum of PGF-1 and PGF-2. Similar to PGF-1, PGF-2 showed broad unresolved peak from 115 ppm to 145 ppm due to different  $sp^2$  carbon centers present in the sample.

Infrared spectra of PGF-1 and PGF-2 (Figure 5.5 (I)) have strong peaks at 1602  $cm^{-1}$  and 1502  $cm^{-1}$  corresponding to  $-C=C-$  vibrations. Weak band at 2184  $cm^{-1}$  in PGF-1 and PGF-2 is due to  $-C\equiv C-$  stretching frequency of connecting linkers. Raman spectra (Figure 5.6) of PGF-1 and PGF-2 showed characteristic D and G bands of graphene centered at 1345  $cm^{-1}$  and 1593  $cm^{-1}$  respectively.

Thermal stability of pillared porous solids PGF-1 and PGF-2 were analyzed using thermogravimetric analysis (Figure 5.5 (II)). PGF-1 and PGF-2 showed high thermal stability with no weight loss up to 300 °C followed by slow weight loss upto 900 °C due to the loss of functional groups on graphene basal plane. PGF-1 and PGF-2 have significantly higher thermal stability in comparison to RGO due to very effective

crosslinking of graphene sheets by linkers and formation of 3-D porous structure. Obtained porous solids were highly hydrophobic with very good chemical stability.

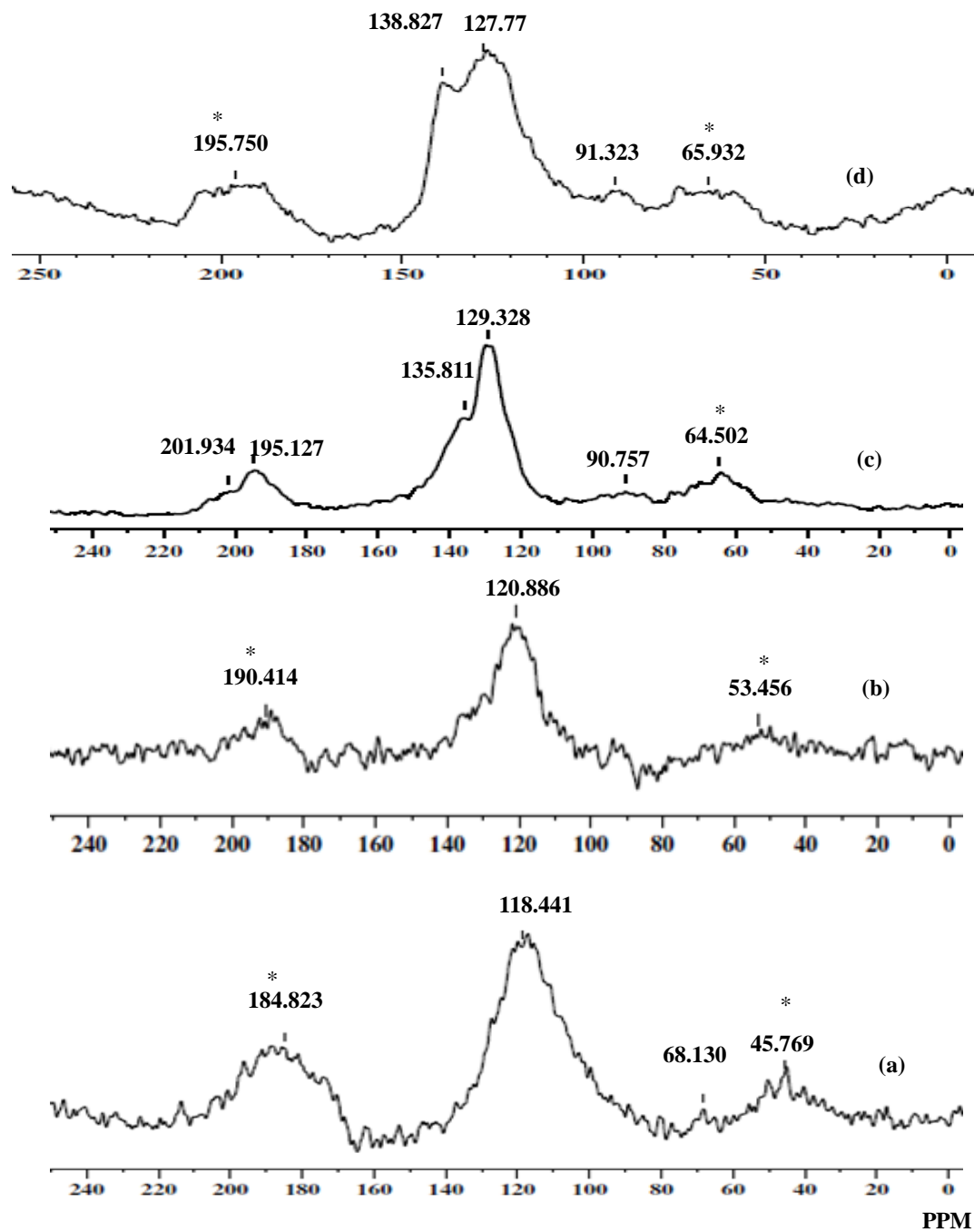


**Figure 5.4** Direct pulse  $^{13}\text{C}$  NMR spectra of (a) RGO (b) IBZ-RGO (c) PGF-1 and (d) PGF-2 at 5 kHz MAS.

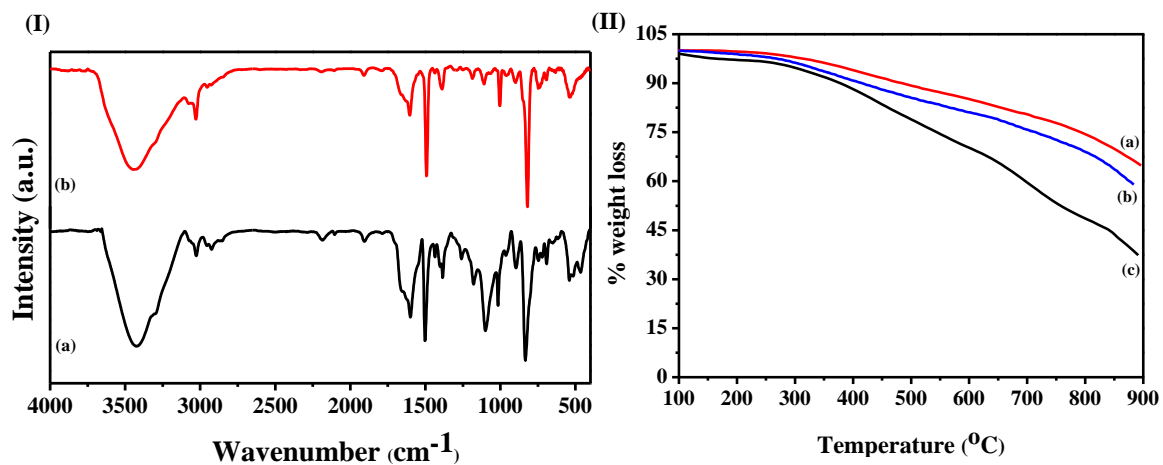


**Figure 5.5** (I) Infrared spectra of (a) PGF-1 (black) and (b) PGF-2 (red). (II) Thermogravimetric analysis of (a) PGF-1 (red), (b) PGF-2 (blue) and (c) RGO (black).

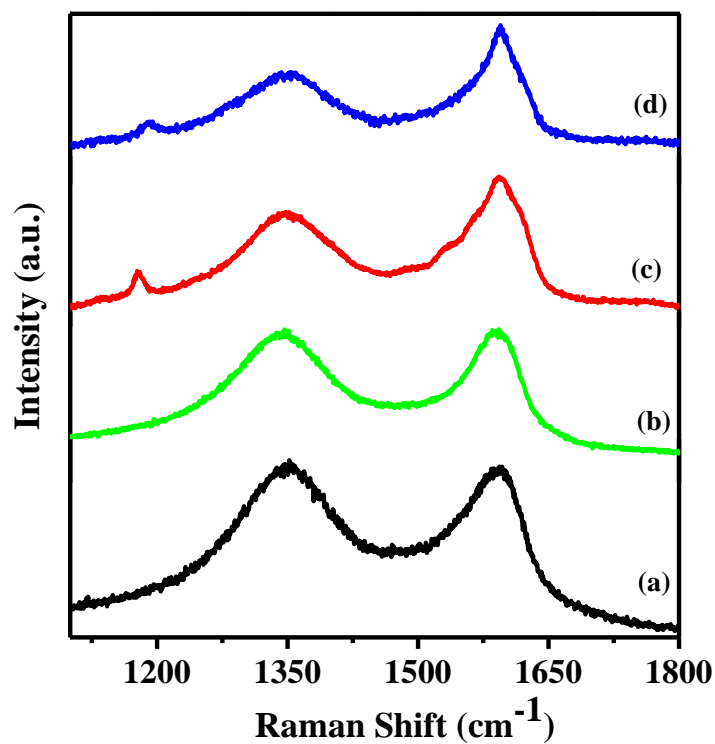


**Figure 5.6** Raman spectra of (a) RGO (black) (b) IBZ-RGO (green) (c) PGF-1 (red) and (d) PGF-2 (blue)

XPS spectrum of PGF-1 showed no peaks corresponding to Iodine. Figure 5.7 shows the survey scan and high resolution C1s core level spectra of PGF-1. Small concentration of oxygen functionality can be observed. Peak positions corresponding to different functional group are represented in figure. Peak at 284.95 can be attributed to  $\text{-C}\equiv\text{C-}$  of the pillar.

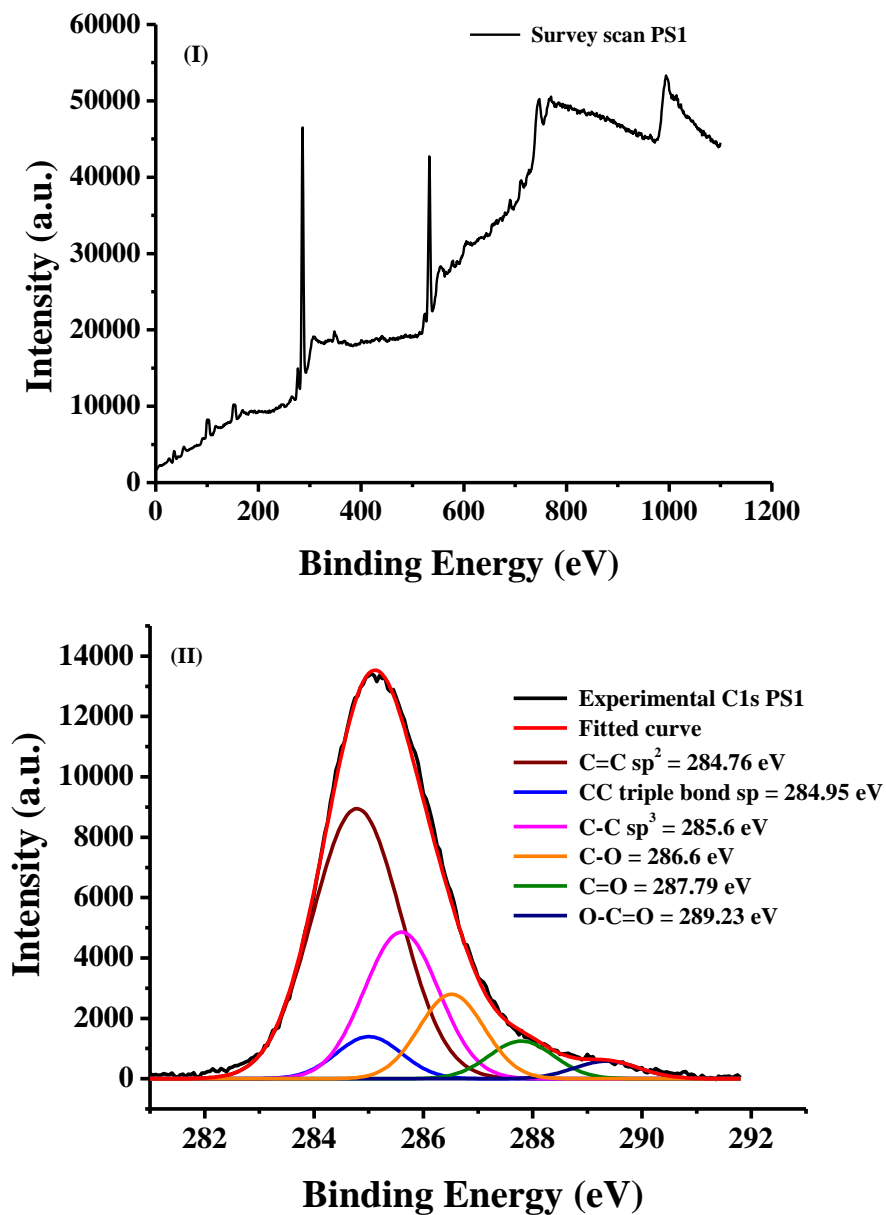
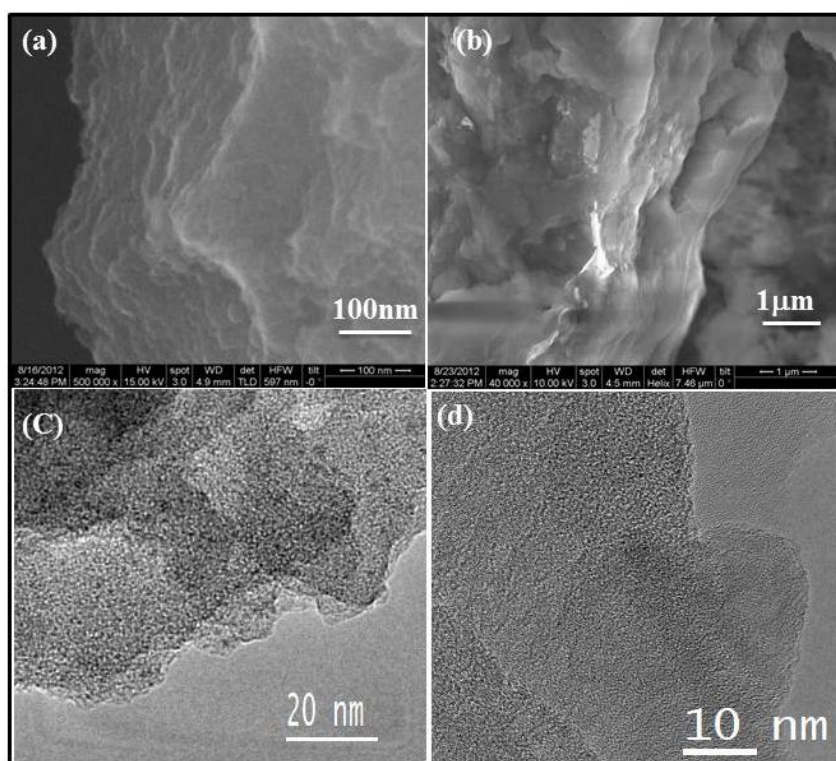
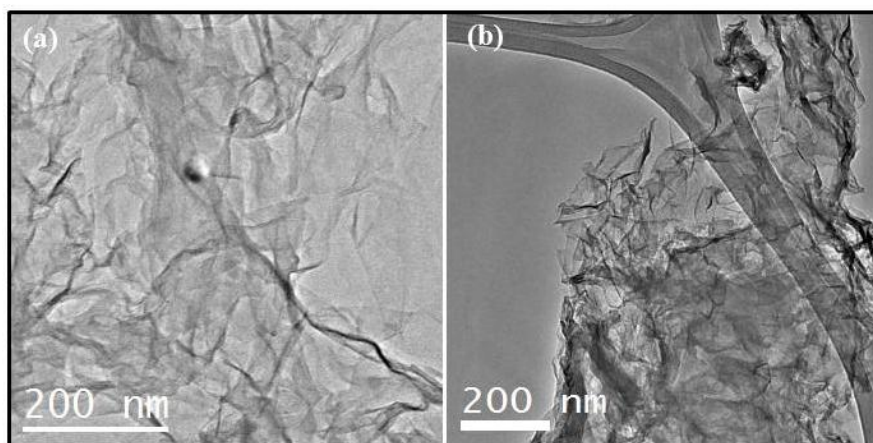


Figure 5.7 (I) Survey scan of PGF-1. (II) High resolution C1s XPS spectra of PGF-1.

3D porous structure of PGF-1 and PGF-2 were further studied by electron microscopy techniques. FESEM images of PGF-1 and PGF-2 showed the formation of micrometer sized particles with sizes ranging from 3 to 6  $\mu\text{m}$  corresponding to the dimension of the RGO sheet (Figure 5.8 a, b). The attachment of several RGO sheets through rigid pillar was clearly observed in SEM. Cross-sectional view of PGF-1 and PGF-2 showed the stacking of several RGO sheets. Greater insight into pillared networks is provided by transmission electron microscopy (TEM). Keen observation at the boundaries of the PGF-1 and PGF-2 reveals thick packing of several graphene sheets into several nanometers (Figure 5.8 c, d). TEM of RGO shows agglomerated few layer graphene sheets with single layer sheets present on edges (Figure 5.9).



**Figure 5.8** FESEM images of (a) PGF-1 and (b) PGF-2. TEM images of (c) PGF-1 and (d) PGF-2.



**Figure 5.9** TEM images of RGO.

Permanent porosity and gas adsorption property of the 3D porous solids PGF-1 and PGF-2 were studied using  $N_2$ ,  $H_2$  and  $CO_2$  gas adsorption. All the samples were activated at  $160\text{ }^\circ\text{C}$  under vacuum before adsorption measurements to remove any moisture or solvent molecules. Figure 5.10 shows the  $N_2$  uptake at 77K of PGF-1 and control sample RGO used for the synthesis of PGF-1 and PGF-2. PGF-1 showed type-IV adsorption profile with steep uptake in the low pressure region upto  $P/P_0$  0.1 followed by hysteresis in the high pressure region which reveals mesoporous nature of pillared solid PGF-1. PGF-1 have final  $N_2$  uptake of 477 ml and Brunauer–Emmet–Teller (BET) surface area of  $824.8\text{ m}^2/\text{g}$ . Also, a Non-local density functional theory (NL-DFT) model is fitted to the  $N_2$  adsorption isotherm to estimate the pore size distribution (inset figure 5.10). The average pore size is found to be  $30.8\text{ \AA}$  indicating the mesoporous nature of the framework. RGO showed type II adsorption profile with BET surface area of  $40\text{ m}^2/\text{g}$  and final  $N_2$  uptake of 60 ml. RGO due to strong  $\pi$ - $\pi$  interaction and remaining oxygen functionality is nonporous and shows the characteristic type II adsorption profile.



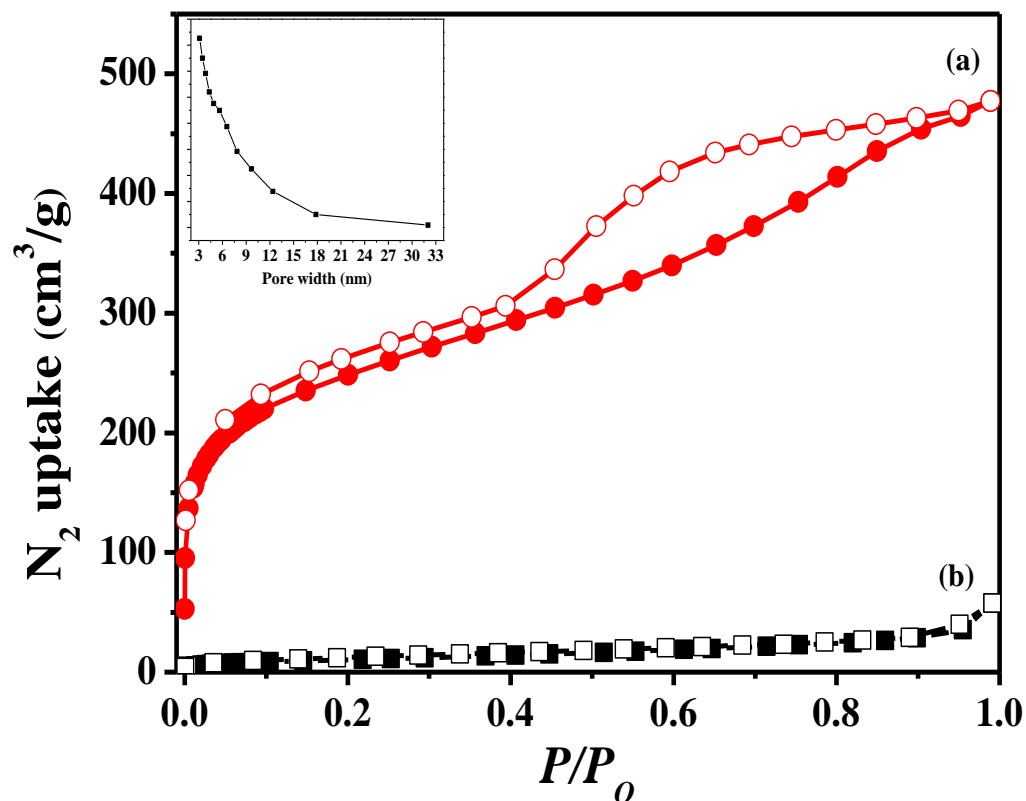


**Figure 5.10** N<sub>2</sub> sorption isotherm of (a) PGF-1 adsorption (red close circle) and desorption (red open circle) and (b) RGO adsorption (black close square) and desorption (black open square) at 77 K. Inset shows the pore size distribution of PGF-1

The N<sub>2</sub> adsorption of PGF-2 at (77 K) is shown in figure 5.11. PGF-2 showed type H4 hysteresis loop which indicates narrow slit like pores with pore width in both micropore and mesopore range. This adsorption behaviour is further supported by pore size distribution from micro to mesopores (1.5 nm - 4.0 nm) (inset figure 5.11). PGF-2 has BET surface area of 770.23 m<sup>2</sup>/g with the final N<sub>2</sub> uptake of 571 ml which is higher than PGF-1. The observed increase in uptake can be attributed to the increased pillar length between graphene sheets in PGF-2.

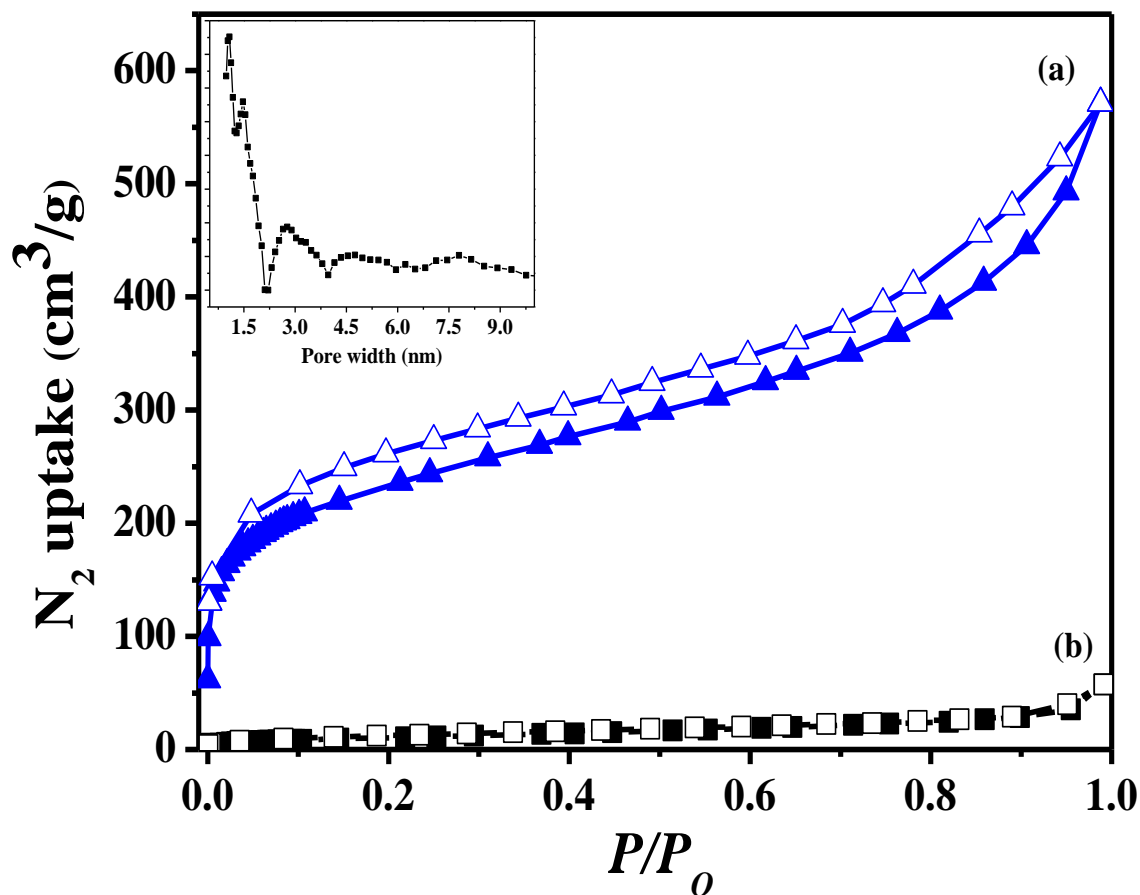


**Figure 5.11**  $N_2$  sorption isotherm of (a) PGF-2 adsorption (blue close triangle) and desorption (blue open triangle) and (b) RGO adsorption (black close square) and desorption (black open square) at 77 K. Inset shows the pore size distribution of PGF-2.

Good thermal and chemical stability along with the high  $N_2$  uptake capacity and surface area of porous solids prompted us to study their potential application in  $\text{CO}_2$  sequestration and  $\text{H}_2$  storage for clean energy applications. Application of high performance porous solids with good thermal and chemical stability provides significant advantage over amine based solvents presently being used for  $\text{CO}_2$  sequestration. Figure 5.12 (I) shows the  $\text{CO}_2$  uptake of PGF-1 and PGF-2 at 195 K and 1 atm pressure. PGF-1 and PGF-2 showed remarkably high  $\text{CO}_2$  uptake of 112 wt.% and 59 wt.% respectively at

195 K and 1 atm. High pressure measurements at 273 K showed the CO<sub>2</sub> uptake of 43 wt.% at 34 bar and 35.9 wt.% at 30 bar for PGF-1 and PGF-2 respectively (Figure 5.12 (II)).

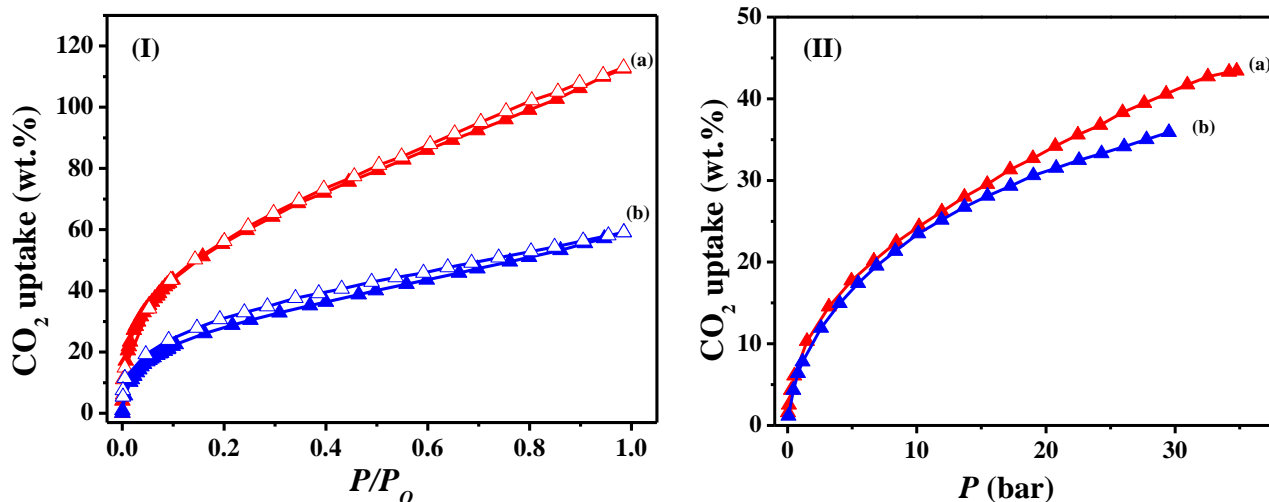


**Figure 5.12 (I)** CO<sub>2</sub> uptake of (a) PGF-1 (red triangle) and (b) PGF-2 (blue triangle) at 195 K and 1 atm. Closed and open triangle corresponds to adsorption and desorption respectively. **(II)** High pressure CO<sub>2</sub> uptake of (a) PGF-1 (red triangle) and (b) PGF-2 (blue triangle) at 273 K

PGF-1 showed 31 wt.% CO<sub>2</sub> uptake at 298 K and 55 bar pressure (Figure 5.13). This remarkably high CO<sub>2</sub> uptake of PGF-1 and PGF-2 can be due to fruitful interaction between remaining oxygen containing functional groups in PGF-1 and PGF-2 and quadrupolar CO<sub>2</sub> molecule ( $-1.4 \times 10^{-39}$  Cm<sup>2</sup>). High CO<sub>2</sub> uptake in PGF-1 and PGF-2 is further supported by the high heat of adsorption ( $q_{st,\phi}$ ) for CO<sub>2</sub> molecules calculated from Dubinin-Radushkevich (DR) equation. Obtained CO<sub>2</sub> uptake values are comparable with high surface area MOFs. We further investigated the application of PGF-1 and PGF-2 for hydrogen storage application. PGF-1 and PGF-2 showed H<sub>2</sub> uptake of 1.9 wt.% and 1.8 wt.% respectively at 77 K and 50 bar pressure (Figure 5.14). Obtained hydrogen uptake capacities are close to high surface area MOFs

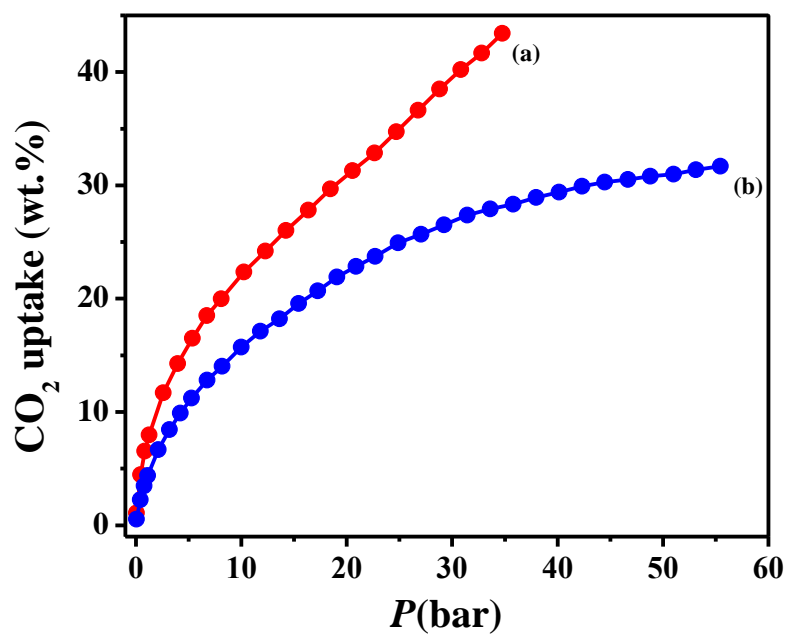


Figure 5.13 High pressure CO<sub>2</sub> uptake of PGF-1 at (a) 273 K (red circle) and (b) 298 K (blue circle).

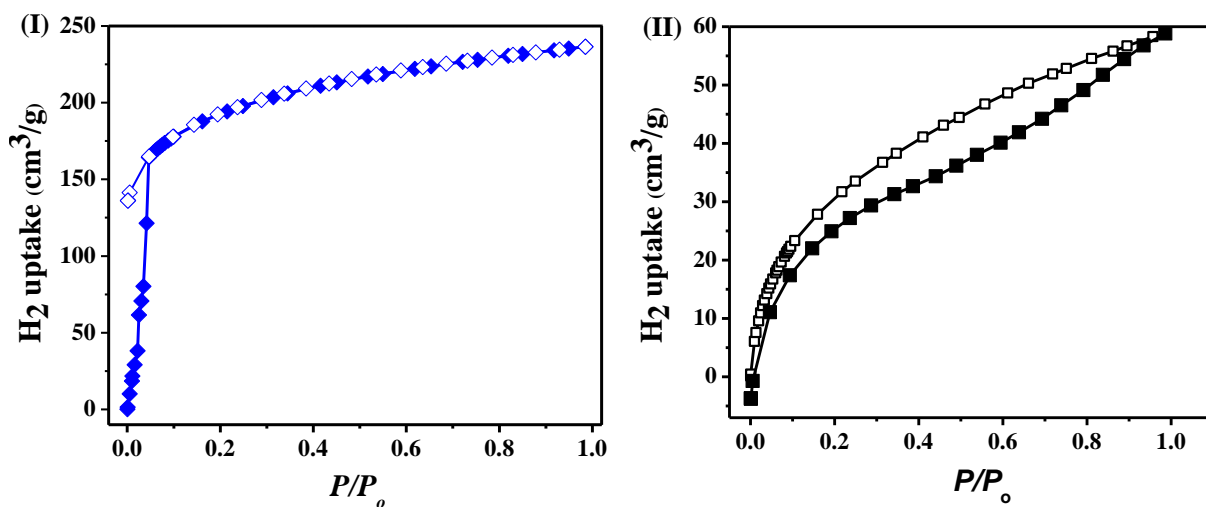


Figure 5.14 H<sub>2</sub> uptake of (I) PGF-1 (blue diamond) and (b) PGF-2 (black diamond) at 77 K and 1 atm.

## **5.4 Conclusions:**

In conclusion, a new method for the synthesis high performance 3D pillared porous structures of graphene is developed. The porous solids PGF-1 and PGF-2 have good thermal and chemical stability with high specific surface areas. They have remarkably high CO<sub>2</sub> uptake and good hydrogen storage capacity. Although Pd catalyzed coupling reaction is utilized for cross linking graphene sheets with tunable pillar length, the synthesis procedure can be utilized for covalent modification of carbon nanotube and graphene. The chemistry of Pd catalyzed reactions is well explored and nanocarbons can be easily functionalized with aryl halide using diazonium salts. Different molecules can be attached to these aryl halide functionalized nanocarbons using C-C or C-N coupling reactions. Our present investigations provide a new synthesis strategy in nanocarbon chemistry. Presently we are investigating the application of these 3D porous solids as electrode materials in electric-double layer capacitors (EDLC). We plan to incorporate polar functional groups such as -OH, -NH<sub>2</sub> or amide etc. to improve CO<sub>2</sub> uptake and H<sub>2</sub> uptake capacity.

## **References:**

- [1] C. Lee, X. Wei, J. W. Kysar, J. Hone, *Science* 2008, *321*, 385-388.
- [2] S. Stankovich, D. A. Dikin, G. H. B. Dommett, K. M. Kohlhaas, E. J. Zimney, E. A. Stach, R. D. Piner, S. T. Nguyen, R. S. Ruoff, *Nature* 2006, *442*, 282-286.
- [3] A. A. Balandin, *Nat Mater* 2011, *10*, 569-581.
- [4] K. P. Loh, Q. Bao, P. K. Ang, J. Yang, *Journal of Materials Chemistry* 2010, *20*, 2277-2289.
- [5] H. Chang, H. Wu, *Advanced Functional Materials* 2012, n/a-n/a.
- [6] C. N. R. Rao, A. K. Sood, K. S. Subrahmanyam, A. Govindaraj, *Angewandte Chemie International Edition* 2009, *48*, 7752-7777.
- [7] S. Moussa, A. R. Siamaki, B. F. Gupton, M. S. El-Shall, *ACS Catalysis* 2011, *2*, 145-154.

- [8] A. Schaetz, M. Zeltner, W. J. Stark, *ACS Catalysis* 2012, 2, 1267-1284.
- [9] W. S. Hummers, R. E. Offeman, *Journal of the American Chemical Society* 1958, 80, 1339-1339.
- [10] W. Gao, L. B. Alemany, L. Ci, P. M. Ajayan, *Nat Chem* 2009, 1, 403-408.
- [11] A. Ghosh, K. V. Rao, S. J. George, C. N. R. Rao, *Chemistry – A European Journal* 2010, 16, 2700-2704.
- [12] G. K. Dimitrakakis, E. Tylianakis, G. E. Froudakis, *Nano Letters* 2008, 8, 3166-3170.
- [13] E. Tylianakis, G. M. Psfogiannakis, G. E. Froudakis, *The Journal of Physical Chemistry Letters* 2010, 1, 2459-2464.
- [14] S. Patchkovskii, J. S. Tse, S. N. Yurchenko, L. Zhechkov, T. Heine, G. Seifert, *Proceedings of the National Academy of Sciences of the United States of America* 2005, 102, 10439-10444.
- [15] P. F. Weck, E. Kim, N. Balakrishnan, H. Cheng, B. I. Yakobson, *Chemical Physics Letters* 2007, 439, 354-359.
- [16] M. M. Biswas, T. Cagin, *The Journal of Physical Chemistry B* 2010, 114, 13752-13763.
- [17] J. W. Burress, S. Gadipelli, J. Ford, J. M. Simmons, W. Zhou, T. Yildirim, *Angewandte Chemie International Edition* 2010, 49, 8902-8904.
- [18] D. R. Dreyer, S. Park, C. W. Bielawski, R. S. Ruoff, *Chemical Society Reviews* 2010, 39, 228-240.
- [19] D. Krishnan, F. Kim, J. Luo, R. Cruz-Silva, L. J. Cote, H. D. Jang, J. Huang, *Nano Today* 2012, 7, 137-152.
- [20] J. L. Bahr, J. Yang, D. V. Kosynkin, M. J. Bronikowski, R. E. Smalley, J. M. Tour, *Journal of the American Chemical Society* 2001, 123, 6536-6542.
- [21] J. L. Bahr, J. M. Tour, *Chemistry of Materials* 2001, 13, 3823-3824.
- [22] C. A. Dyke, J. M. Tour, *Journal of the American Chemical Society* 2003, 125, 1156-1157.
- [23] C. A. Dyke, J. M. Tour, *Nano Letters* 2003, 3, 1215-1218.
- [24] J. R. Lomeda, C. D. Doyle, D. V. Kosynkin, W.-F. Hwang, J. M. Tour, *Journal of the American Chemical Society* 2008, 130, 16201-16206.
- [25] B. H. Yang, S. L. Buchwald, *Journal of Organometallic Chemistry* 1999, 576, 125-146.
- [26] S. Banerjee, T. Hemraj-Benny, S. S. Wong, *Advanced Materials* 2005, 17, 17-29.
- [27] D. Tasis, N. Tagmatarchis, A. Bianco, M. Prato, *Chemical Reviews* 2006, 106, 1105-1136.
- [28] S. Niyogi, M. A. Hamon, H. Hu, B. Zhao, P. Bhowmik, R. Sen, M. E. Itkis, R. C. Haddon, *Accounts of Chemical Research* 2002, 35, 1105-1113.
- [29] M. Prato, K. Kostarelos, A. Bianco, *Accounts of Chemical Research* 2007, 41, 60-68.
- [30] M. Jahan, Q. Bao, J.-X. Yang, K. P. Loh, *Journal of the American Chemical Society* 2010, 132, 14487-14495.
- [31] H. Cabibil, H. Ihm, J. M. White, *Surface Science* 2000, 447, 91-104.
- [32] S. Park, Y. Hu, J. O. Hwang, E.-S. Lee, L. B. Casabianca, W. Cai, J. R. Potts, H.-W. Ha, S. Chen, J. Oh, S. O. Kim, Y.-H. Kim, Y. Ishii, R. S. Ruoff, *Nat Commun* 2012, 3, 638.
- [33] Y. Si, E. T. Samulski, *Nano Letters* 2008, 8, 1679-1682.